Bose-Einstein Correlations in ep Collisions at HERA using the H1 Detector

Syed Eram Abbas Rizvi

Department of Physics,
Queen Mary and Westfield College,
University of London

A thesis submitted in accordance with the regulations
for the Degree of Doctor of Philosophy
in the University of London

April 1997

Abstract

The two-particle correlation function is measured for neutral current DIS events with $5 \leq Q^2 \leq 100$ GeV^2 with data taken by the H1 detector at HERA with $\sqrt{s}$ = 300 GeV during the 1994 run period corresponding to an integrated luminosity of 1.3 pb^{-1}. The diffractive and non-diffractive selections of the data are analysed separately, and both exhibit an enhanced correlation for small 4-momentum difference for like-sign pairs as expected from Bose-Einstein interference in the production amplitudes for identical boson pairs. Fits using a Gaussian parametrisation of the enhancement yield no statistically significant difference between the diffractive and non-diffractive samples. The non-diffractive data sample is further separately analysed in three bins of each of the kinematic variables x, Q^2, and W as well as mean particle density, $\langle dn/d\eta^* \rangle$, in the hadronic centre of mass frame. Of these a strong evolution of the Gaussian fit parameters is observed with increasing particle density only. The non-diffractive data are also compared to three fit parameterisations: Gaussian, exponential, and power-law. The most favourable χ^2 is obtained for the exponential fit, though the power-law attains a similarly successful description of the data in the region of low 4-momentum difference.

This thesis is dedicated to the memory of my aunt Yasmeen Nawaz Khan, my uncle Sehba Akhter, Poet Laureate of Pakistan, and my grandfather Dr. Nuruddin Noorani.

Contents

List of Figures

List of Tables

Introduction

Since the beginning of the 20^{th} century scattering experiments have proved to be highly successful means of probing the structure and composition of matter at ever decreasing distance scales. Together with data from matter-antimatter annihilation experiments, two "gauge" theories of particle interactions have emerged, namely Electro-Weak theory (EW) and Quantum Chromo-Dynamics (QCD). They describe the interactions of fermions as being mediated by the exchange of gauge bosons, which transfer 4-momentum; gluons in the case of QCD, and photons, the Z^0, and $W^{\pm}$ particles for EW. Electro-weak theory combines the highly successful quantum theory of electromagnetism - Quantum Electro-Dynamics (QED), with the gauge theory of weak interactions. When taken together QCD and EW form the Standard Model which represents the most successful theory of matter we have, incorporating three of the four fundamental forces of nature: the strong, weak and electromagnetic forces. The fourth, gravity, is not included since even at the highest attainable energies it is negligible in comparison with the other interactions.

Early lepton-nucleon scattering experiments utilised the easily accelerated leptons as a source of electro-weak bosons to inelastically probe the nucleon with a 4-momentum transfer, **q**. At large momentum transfer squared of ~ 4 GeV^2 the experiments reached the regime of deep inelastic scattering (DIS) which revealed many features of nucleon structure, showing its composite nature of charged fermionic constituents which were point like and free within the nucleon.

HERA is the most recent *ep* scattering experiment able to study both neutral current (NC) DIS in which photons, or Z^0s are exchanged, and charged current (CC) DIS occurring via $W^{\pm}$ exchange. It has allowed the mechanisms of QCD and EW to be tested in previously unexplored regions of phase space. The emerging data have already made significant contributions in the understanding of proton structure and

have shown surprising results such as the existence of a diffractive component in DIS. Diffractive processes are associated with soft hadronic interactions and were postulated to occur via the exchange, at large centre of mass energies, of the "pomeron", ($I\!P$), an object with the quantum numbers of the vacuum. HERA has provided the opportunity to determine the structure of diffractive exchange to an unprecedented level of accuracy.

Further insight and tests of QCD have been achieved by the analysis of the hadronic final state. Studies have included measurements of the multiplicity distribution in the hadronic centre of mass frame, and the fragmentation functions of quarks to name but two. These analyses centre on measurements of single variable distributions in the statistical system of the hadronic final state. In other words how often a variable takes on a particular value reveals much useful information. However, information can also be extracted by examining how two variables behave simultaneously, or how they are correlated. Correlation functions are designed for this purpose. They measure how frequently two (or more) variables take on particular values with respect to a statistical background. In the context of multi-particle production in high energy physics, such correlation functions provide information on the dynamics of the hadronisation process in which quarks and gluons combine to form colourless hadrons. Hadronisation is a soft process and therefore well beyond the scope of perturbative calculation. For this reason research in this area is often neglected, though in recent years there has been a revival due to the technical improvements in measuring correlations, as well as new theoretical input.

This work is an analysis of Bose-Einstein Correlations (BEC) in which quantum mechanical interference in the production amplitudes of identical bosons leads to an enhancement in the probability of finding two bosons with similar 4-momentum. It was first proposed as an interference measurement to determine the angular diameter of stellar bodies by Hanbury-Brown and Twiss in 1954. The effect was rediscovered by G. and S. Goldhaber, Lee, and Pais in $p\bar{p}$ anihillation in 1959 and has since been studied in all available types of high energy collisions in an attempt to understand the space-time structure of the boson source. Although such analyses have been done in previous DIS experiments, HERA represents the highest centre of mass energy to date. It offers the unique opportunity to examine whether the

boson source behaves in the same manner for virtual photon-proton collisions as for virtual photon-pomeron collisions within the same experiment. The nature of deeply inelastic scattering also offers the chance to test for any evolution of the source size (or indeed its lifetime) over the accessible kinematic range.

BEC are relevant to studies of particle distributions as these are affected by the quantum mechanical constraints imposed at production. Furthermore BEC are known to distort the line shape of short lived resonances, thereby influencing the production cross-section measurements. This is most notable for the ρ^0 and also has consequences for real $W^{\pm}$ production at LEP2. In high energy collisions, soft hadronic production constitutes a large part of the total cross-section, and yet it remains the area of QCD about which we are most ignorant. It is hoped that further study may lead to a better understanding of non-perturbative QCD and the process of colour confinement.

Chapter 1 contains a description of the setup of HERA and the H1 detector during the 1994 run period. Emphasis is placed on the main components used in this analysis. In chapter 2 a short introduction to DIS is presented and a brief discussion of diffraction at HERA. The Monte Carlo models used are described in chapter 3, followed by a discussion in chapter 4 of the selections used to identify the events and tracks on which this work is based. The measurements of BEC are presented in chapter 5 which includes a discussion of resolution and bias within the data. Finally the major results and conclusions are collected together in chapter 6. The analysis presented here has been submitted for publication to Zeitschrift für Physik.

Throughout this thesis a system of units is used in which $\hbar = c = 1$.

Chapter 1

The HERA Collider and the H1 Detector

1.1 The HERA Collider

The HERA accelerator (shown in figure 1.1) is the first colliding beam machine to study *ep* collisions. It is designed to collide 820 GeV protons with 30 GeV electrons[1] which are stored in independent rings situated in a 6.3 km tunnel, 20 m below ground. The beams are brought to collision at two intersection points with zero crossing angle in the experimental Halls where the HERA detectors H1 and ZEUS are located. The particles are stored in a maximum of 210 bunches which collide at intervals of 96 ns. In 1994 HERA ran with 153 colliding bunches, and an additional 15 electron, and 17 proton non-colliding bunches (known as *pilot* bunches), used to determine background rates from interactions of beam particles with the beam pipe and residual gas. During the 1994 data taking period an integrated luminosity of 3.5 pb^{-1} was delivered by HERA to H1, with an average instantaneous luminosity of $1.4 \times 10^{30} cm^{-2} s^{-1}$. Operational efficiencies and deadtime reduce this to 1.3 pb^{-1} which could be used for analysis.

The electron beam is constrained by conventional magnets and can attain a maximum energy of 30 GeV limited by synchrotron radiation losses. For the proton beam synchrotron losses are small, and super-conducting magnets are used for bending, since iron magnets cannot provide the 4.7 T fields required.

[1]Throughout this thesis the term electron will be taken to mean both electrons and positrons.

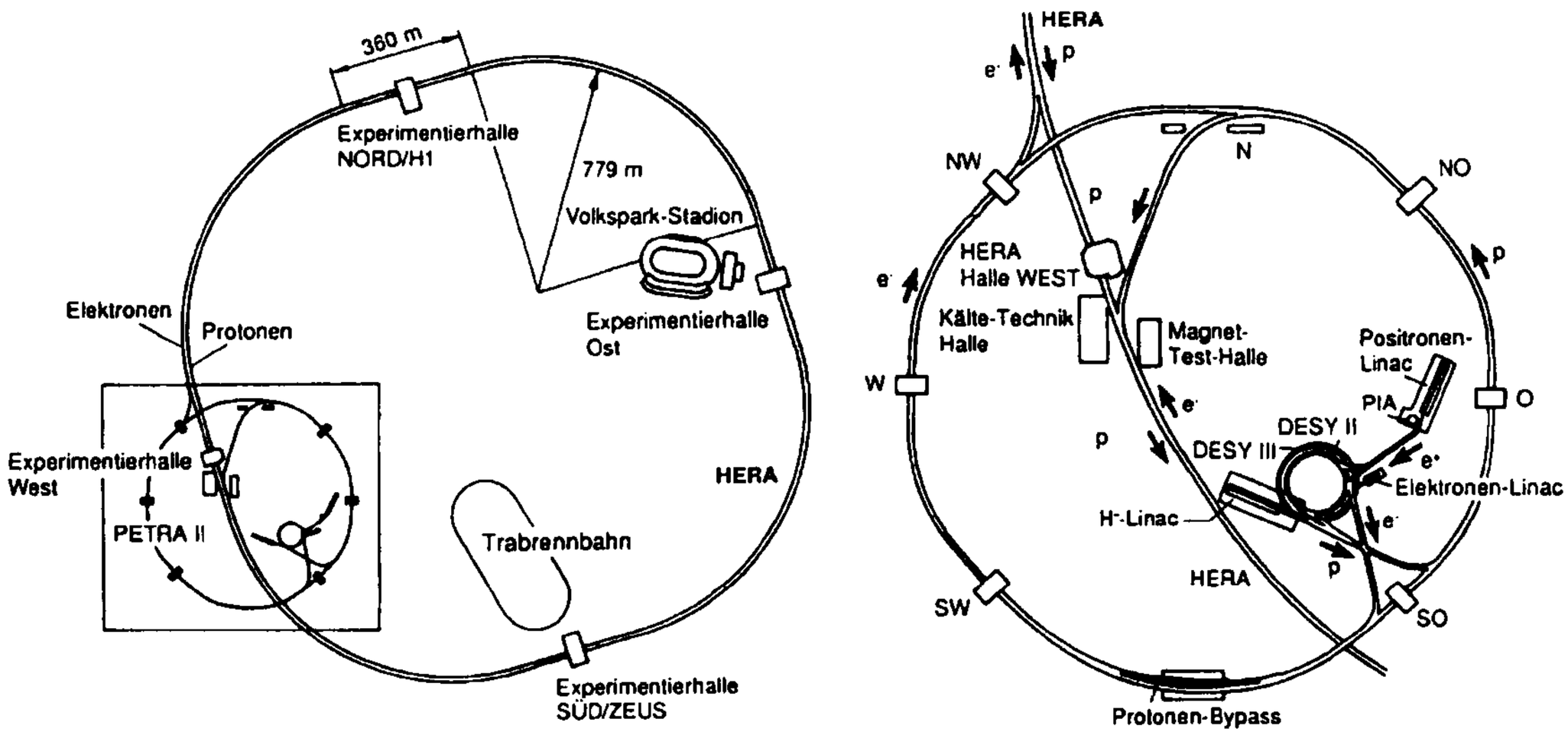

Figure 1.1: Layout of the HERA machine with pre-accelerators

1.2 The H1 Detector

A schematic diagram of the H1 detector[2] is shown in figure 1.2. It is a 4π detector offering excellent hermetic coverage of the interaction region and is designed for the study of many different physics processes whilst being able to reject beam induced background events with a high efficiency. The centre of mass for *ep* collisions is boosted forward in the proton direction and so H1 is highly segmented and more heavily instrumented in this region. In the backward (electron) direction good electron identification is important so as to be able to isolate the scattered lepton from DIS events. In order to differentiate *ep* collisions from background a multi-level pipelined trigger is used, complemented by a fast digitisation and readout chain capable of writing 250,000 channels to tape at rates of $\sim$10 Hz.

The tracking chambers surrounding the interaction point detect charged particles by gas ionisation. Surrounding the tracking system is the liquid argon calorimeter (LAr), complemented by the plug calorimeter in the extreme forward direction around the beam pipe. The Backward Electromagnetic Calorimeter (BEMC), is used to detect the scattered lepton from low Q^2 NC DIS events. Mounted on the face of the BEMC is the Backward Proportional Chamber (BPC), designed to provide accurate spatial resolution for scattered electron identification. On the far side of the BEMC is the scintillator Time-of-Flight system (ToF), whose pur-

[2]The H1 right handed cartesian coordinate system is defined with respect to the nominal interaction point such that the positive z axis points in the direction of the proton beam along the beam line, and the x axis points towards the centre of the HERA ring.

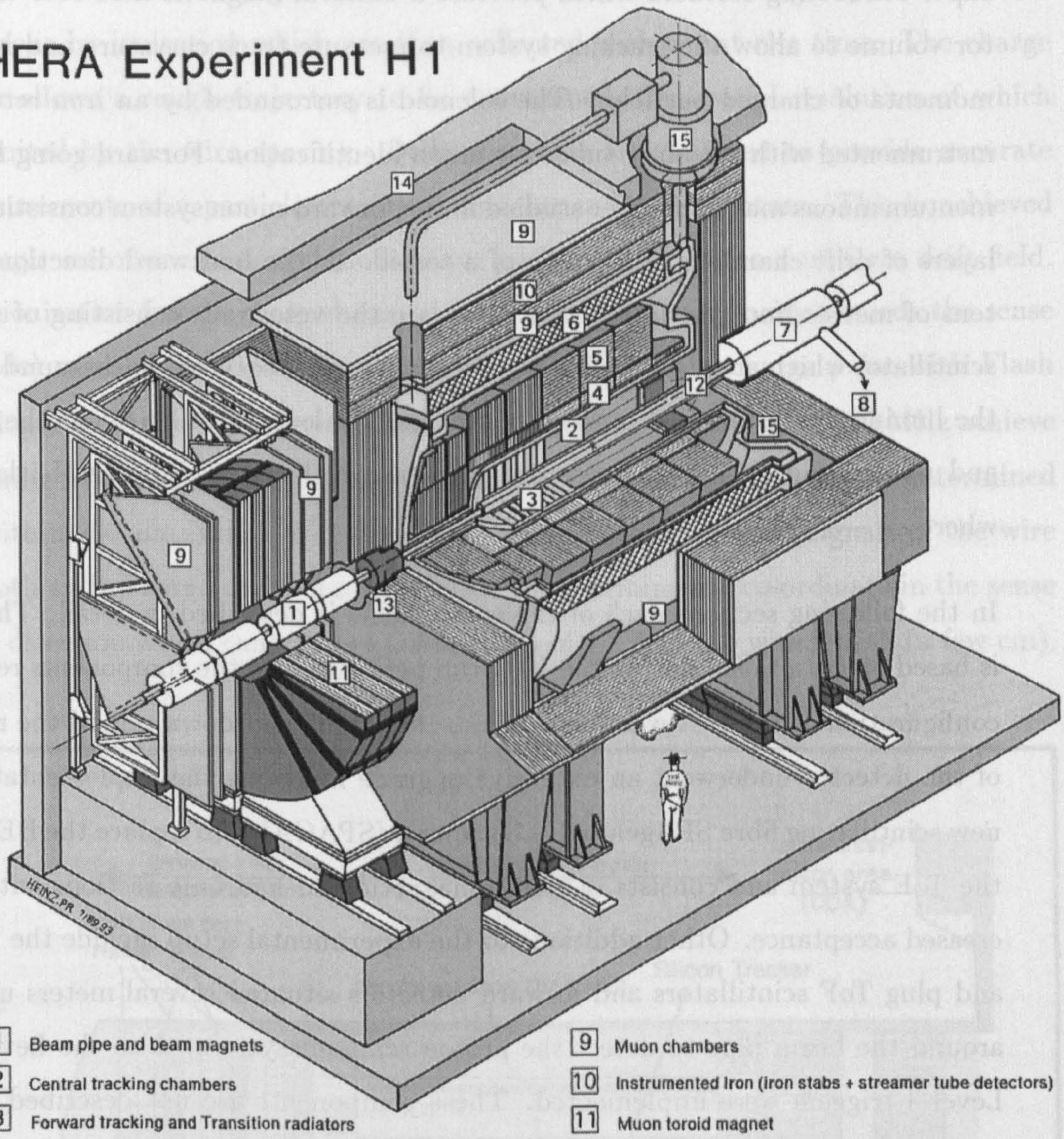

Figure 1.2: Diagram of the H1 detector showing individaul sub-components.

pose is to provide accurate timing information in order to veto events originating from proton beam induced background. These components are situated inside a super-conducting solenoid which provides a uniform magnetic field over the detector volume to allow the tracking system to measure track curvature and hence the momenta of charged particles. The solenoid is surrounded by an iron return yoke instrumented with streamer tubes for muon identification. Forward going high momentum muons may be further studied in the forward muon system consisting of two layers of drift chambers either side of a toroid. In the backward direction, several tens of metres from the interaction point are the veto walls consisting of sheets of scintillator which are also used to veto proton beam associated background. Finally the luminosity system is composed of two small calorimeters known as the e-tagger and photon tagger and are designed to measure the rate of Bethe-Heitler events where $ep \longrightarrow ep\gamma$.

In the following sections each of the components is described in detail. This thesis is based on data taken during the 1994 run period and so the components reflect the configuration of H1 as it was then. In the 1994/1995 shutdown period the rear part of the detector underwent an extensive upgrade involving the implementation of a new scintillating fibre SPAgehtti CALorimeter (SPACAL), to replace the BEMC and the ToF system and consists of electromagnetic and hadronic sections with an increased acceptance. Other additions to the experimental setup include the Forward and plug ToF scintillators and forward detectors situated several meters upstream around the beam pipe to detect the proton remnant system. Also the Level 2 and Level 3 triggers were implemented. These components are not described and the reader is referred to [2] for further details.

1.3 Tracking Chambers

The tracking system is divided into two components, the central and forward trackers, covering the range $15° \leq \theta \leq 165°$, and $7° \leq \theta \leq 25°$ respectively where θ is defined with respect to the proton beam direction ($+ z$ axis). Additionally a backward proportional chamber covering the range $156° \leq \theta \leq 175°$ is used to identify the scattered lepton track. The components are shown in longitudinal section in figure 1.3. Both central and forward tracking systems are composed of multi-wire

proportional chambers (MWPCs), and drift chambers. The MWPCs have good timing response and are used for triggering purposes. They are composed of finely spaced anode wires in a gas volume, such that an incident charged particle creates electrons by ionisation which are then collected with a fast rise time. The charge pulse allows a rough trajectory to be determined, the spatial resolution of which is limited by the wire spacing. Drift chambers are designed to provide accurate measurements of a particle trajectory and hence its momentum. This is achieved through use of anode and cathode wires positioned to create a uniform drift field. The ionisation from a charged particle drifts at constant velocity towards the sense (anode) wires, typically at 50 μm/ns. Digitisation of the charge pulse with Flash Analogue to Digital Converters (FADCs) at sampling frequencies of 100 MHz achieve a timing resolution of a few nano-seconds. Thus spatial positions can be determined to within 200 μm in the drift direction. By comparing readout signals of the wire at both ends, charge division may be used to determine the co-ordinate in the sense wire direction which can achieve a resolution of 1-2% of the wire length (a few cm).

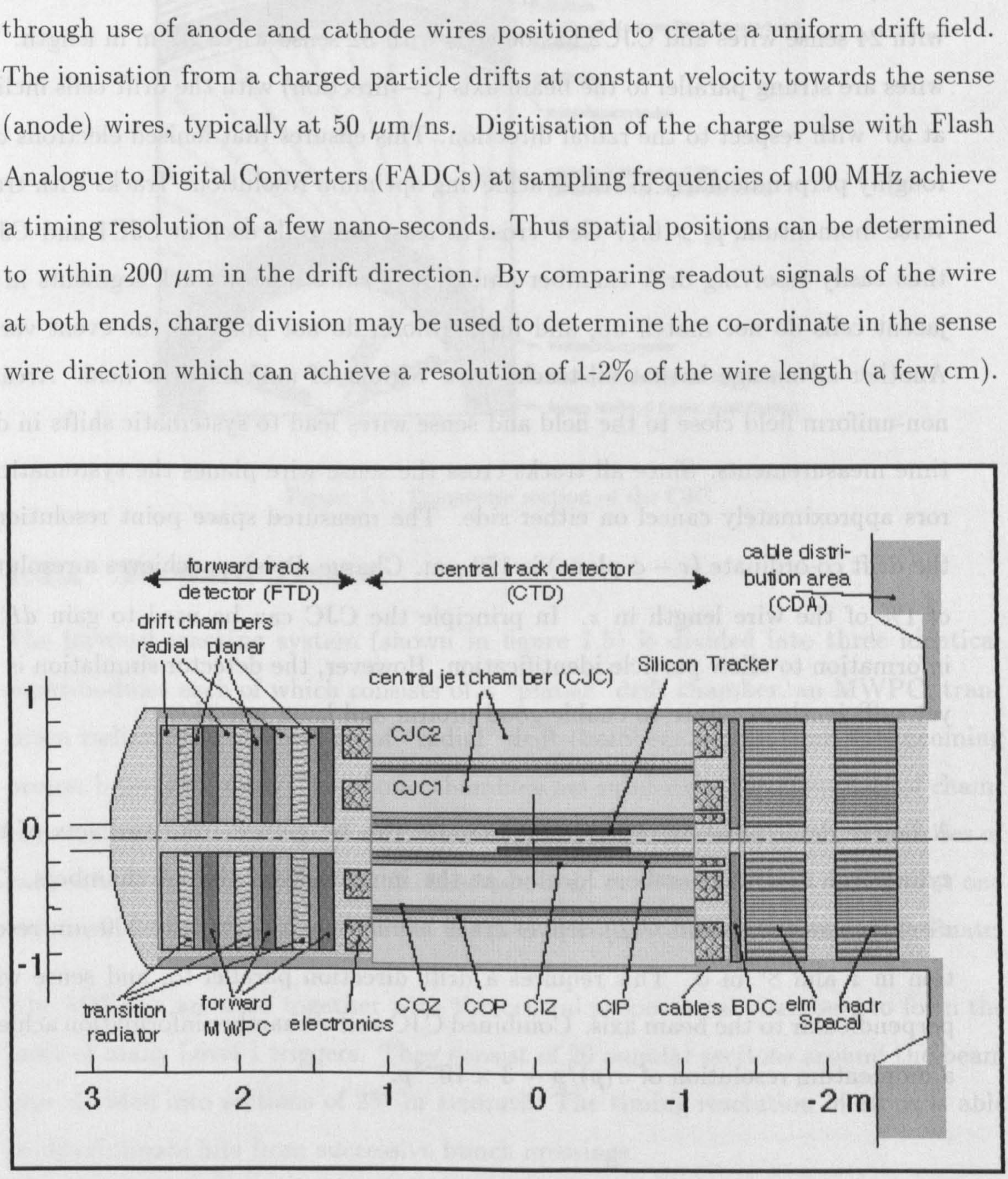

Figure 1.3: Longitudinal view of the H1 tracking systems.

1.3.1 Central Tracker

The present analysis is mainly based on the central tracking system, closest to the interaction point. Measurements of charge and momentum of charged particles are provided by two large cylindrical drift chambers (central jet chambers, CJC1 and CJC2) shown in cross-section in figure 1.4. The inner chamber, CJC1, has 30 cells with 24 sense wires and CJC2 has 60 cells with 32 sense wires 2.2 m in length. The wires are strung parallel to the beam axis ($z-$direction) with the drift cells inclined at 30° with respect to the radial direction. This ensures that ionised electrons drift roughly perpendicularly to tracks achieving optimum resolution. Tracks with transverse momentum, $p_t > 0.17$ GeV cross at least two cells each in CJC1 and CJC2, thus easily resolving drift chamber ambiguities since mirror track segments in adjacent cells do not match up, and furthermore, do not point to the event vertex. Another advantage is that all tracks cross regions of uniform drift field. Areas of non-uniform field close to the field and sense wires lead to systematic shifts in drift time measurements. Since all tracks cross the sense wire planes the systematic errors approximately cancel on either side. The measured space point resolution in the drift co-ordinate ($r-\phi$ plane) is 170 μm. Charge division, achieves a resolution of 1% of the wire length in z. In principle the CJC can be used to gain dE/dx information to allow particle identification. However, the detector simulation is not yet sufficiently accurate to enable good proton and kaon rejection.

A better determination of the z co-ordinate can be gained from two sets of thin cylindrical $z-$drift chambers located at the inner radii of the jet chambers. The $z-$chambers (COZ and CIZ) deliver track elements with typically 300 μm resolution in z and 8° in ϕ. This requires a drift direction parallel to, and sense wires perpendicular to the beam axis. Combined CJC and z-chamber information achieves a momentum resolution of $\sigma(p)/p \sim 3 \times 10^{-3} p$.

The central proportional chambers (CIP and COP) are used in the Level 1 trigger to give a fast estimate of the z position of the event vertex.

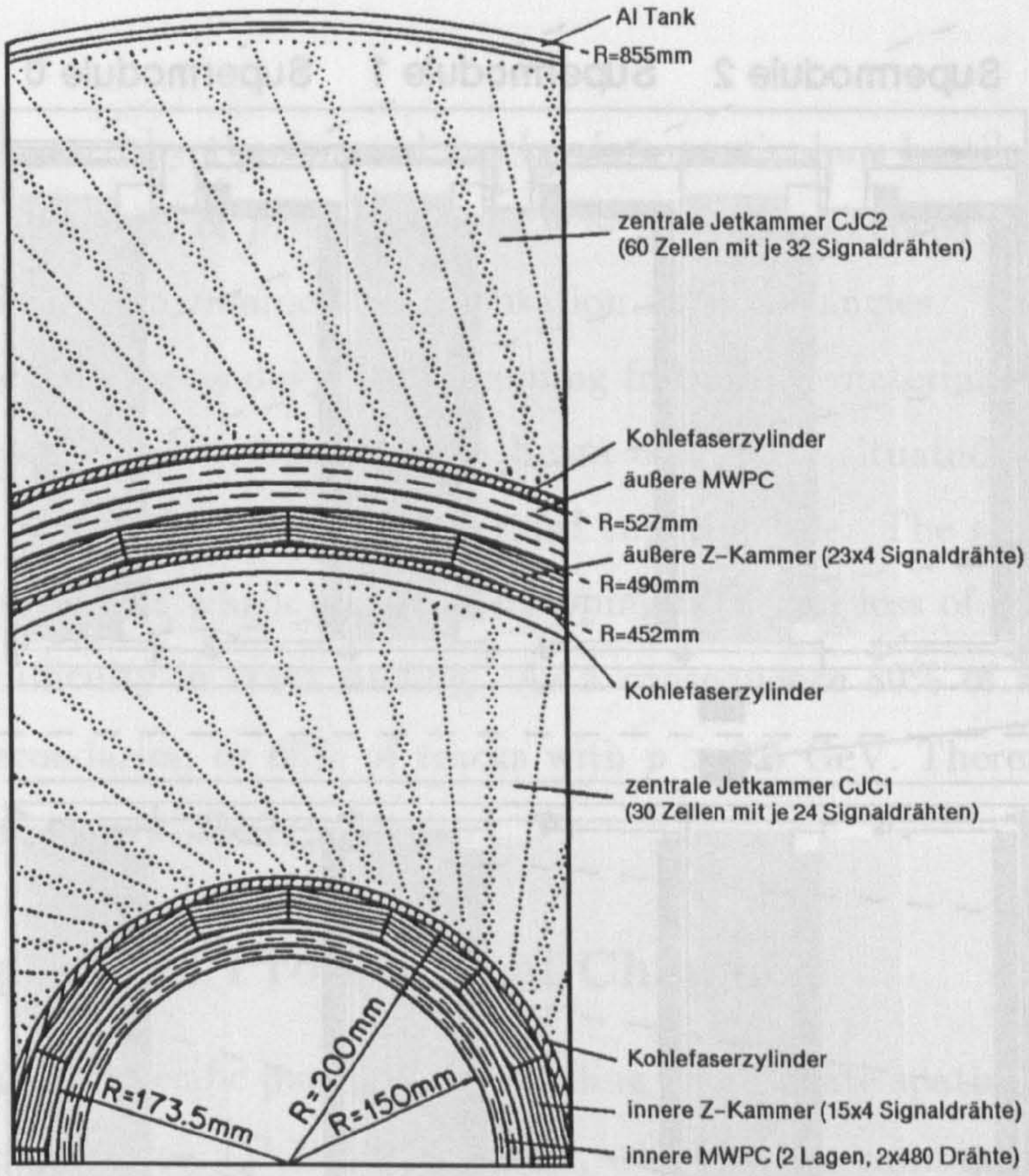

Figure 1.4: Transverse section of the CJC.

1.3.2 Forward Tracker

The forward tracking system (shown in figure 1.5) is divided into three identical supermodules each of which consists of a "planar" drift chamber, an MWPC, transition radiators, and a section of "radial" drift chambers as seen from the incoming proton beam direction. The planar chambers are subdivided into four sets of chambers each with three layers of cells whose wires extend in the xy plane. The wires of each subset are rotated from each other by 60° in ϕ. Wires are only read out at one end so no information about the hit position is available along the wire co-ordinate.

The MWPCs are used together with the central proportional chambers to form the basis of many Level 1 triggers. They consist of 20 annular sections around the beam pipe divided into sections of 25° in azimuth. The timing resolution of 20 ns is able to discriminate hits from successive bunch crossings.

The transition radiators are composed of a passive array of 400 polypropylene layers. An incident particle on crossing each dielectric interface emits a "soft" X-ray

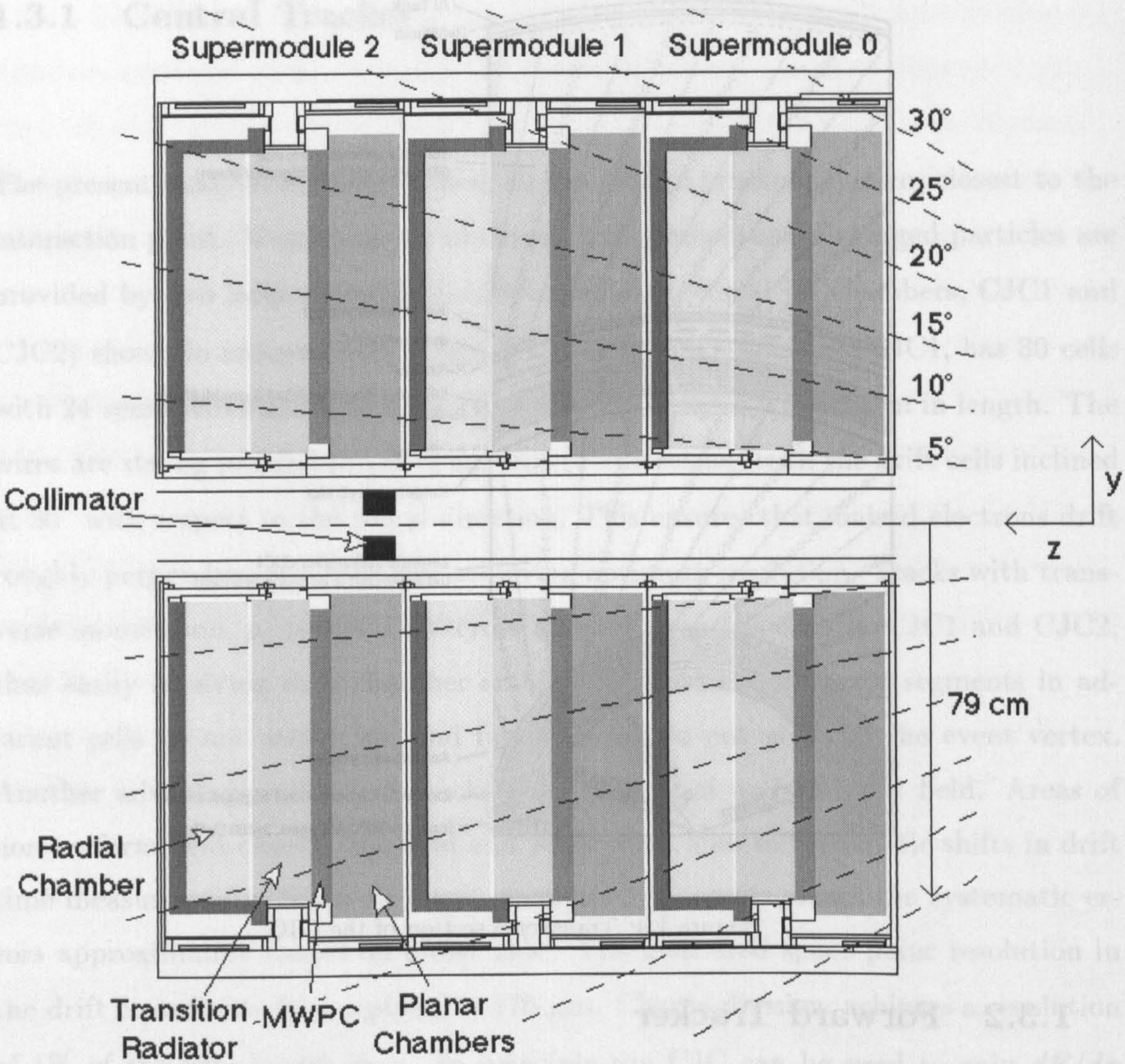

Figure 1.5: Longitudinal section of the forward tracking system.

photon of a few keV with a typical probability of emission of 1% for a 20 GeV electron. This can be used for e/π separation since the X-ray emission probability is proportional to the Lorentz γ factor which is larger for electrons than for pions of equal momentum.

The X-ray, emitted at angles $\sim 1/\gamma$, is detected in the radial chambers through photo-ionisation of the gas volume. This is coupled with the usual ionisation by the particle itself and leads to an enhanced charge pulse on the wires from which the electrons and pions can be discriminated. The radial chambers are composed of 12 layers of 40 radially strung wires providing a good ϕ measurement and information on the radial co-ordinate from charge division. Inefficiencies in the first few layers of the radial chambers mean that the particle identification has never worked suc-

cessfully.

The region covered by the forward tracker is a particulary hostile environment in which the multiplicity of *primary* tracks is $\sim 10 - 15$ composed of low momentum particles from proton remnant fragmentation at small angles. This is further exacerbated by many secondary tracks coming from dead material between the CJC and the forward tracker, as well as a beam collimator situated within the beam pipe at $z = 2.04$ m, i.e. beneath the third supermodule. The secondaries lead to a high density of hits which causes overlapping hits, and loss of information and a subsequent difficulty in track finding. As a consequence 80% of all tracks in this region are secondaries, or 60% of tracks with $p > 0.5$ GeV. Therefore the forward tracker was not used in this analysis.

1.3.3 Backward Proportional Chamber

The BPC has the specific purpose of providing an accurate spatial resolution of the scattered lepton in low Q^2 NC DIS events, which, when combined with an energy measurement from the BEMC gives a high resolution of kinematic quantities (see chapter 4). The chamber is composed of four wire layers strung in the xy plane, each layer being rotated by 45° with respect to each other. An angular resolution in θ of 0.5 mrad is attained with a detection efficiency of 98%.

1.4 Calorimeters

Calorimeters complement the information obtained from the tracking system since they are able to detect neutral particles, provide energy measurements of jets with high particle densities, and have a resolution which improves at high energy in contrast to the trackers. Calorimeters are also used to distinguish between electrons and pions from geometric comparisons of shower profiles of the energy deposition. The H1 detector has its main calorimeters within the magnetic field coil so as to reduce the amount of dead material in front of the calorimeter and to reduce its overall size and weight. The largest component is the Liquid Argon Calorimeter (LAr), covering the range $4° \leq \theta \leq 154°$. The BEMC is purely an electromagnetic calorimeter covering $151° \leq \theta \leq 177°$. The plug provides additional coverage around the forward beam pipe in the range $0.7° \leq \theta \leq 4°$. The instrumented iron

return yoke around H1 is additionally used to measure energy leakage from the LAr and the BEMC, and is also known as the "tail catcher". All of these components are sampling calorimeters and have alternate layers of passive absorber material followed by active instrumented regions. Incident particles lose energy in the absorber by inelastic collisions producing a shower of secondary particles whose number is sampled in the active regions as the shower develops in depth. The number of particles detected is proportional to the energy of the initiating particle. Electromagnetic showers from electrons and photons consist of further photons and electron produced as Bremsstrahlung and pair-production respectively. Hadronic showers develop from inelastic nuclear collisions and have a larger longitudinal and transverse extent than electromagnetic showers.

1.4.1 Liquid Argon Calorimeter

The liquid argon calorimeter is designed to measure the hadronic final state as well as the scattered lepton from high Q^2 NC DIS events. For this reason the calorimeter is split radially into two parts, an innermost electromagnetic section and an outer hadronic section as shown in figure 1.6. The calorimeter is further subdivided into eight "wheels" in z, each with eight ϕ segments. The electromagnetic section consists of lead absorber plates in a liquid argon sampling medium and varies from 20-30 radiation lengths in depth. The hadronic section has steel absorber plates and varies from 4.5-8 interaction lengths. Energy dependent weighting factors are applied to hadronic measurements since the charge collection efficiency for hadrons is about 30% less than for electrons. The electromagnetic section has a resolution obtained from test beam measurements of $\sigma(E)/E \sim 0.12/\sqrt{E(\mathrm{GeV})} \oplus 0.01$. The overall energy scale is known to within 3% from comparisons of scattered lepton energy between the LAr and the CJC. The hadronic section has a resolution of $\sigma(E)/E \sim 0.5/\sqrt{E(\mathrm{GeV})} \oplus 0.01$ obtained from test beam data. The hadronic energy scale is known to within 6%, determined from measurements of transverse momentum balance in NC DIS events.

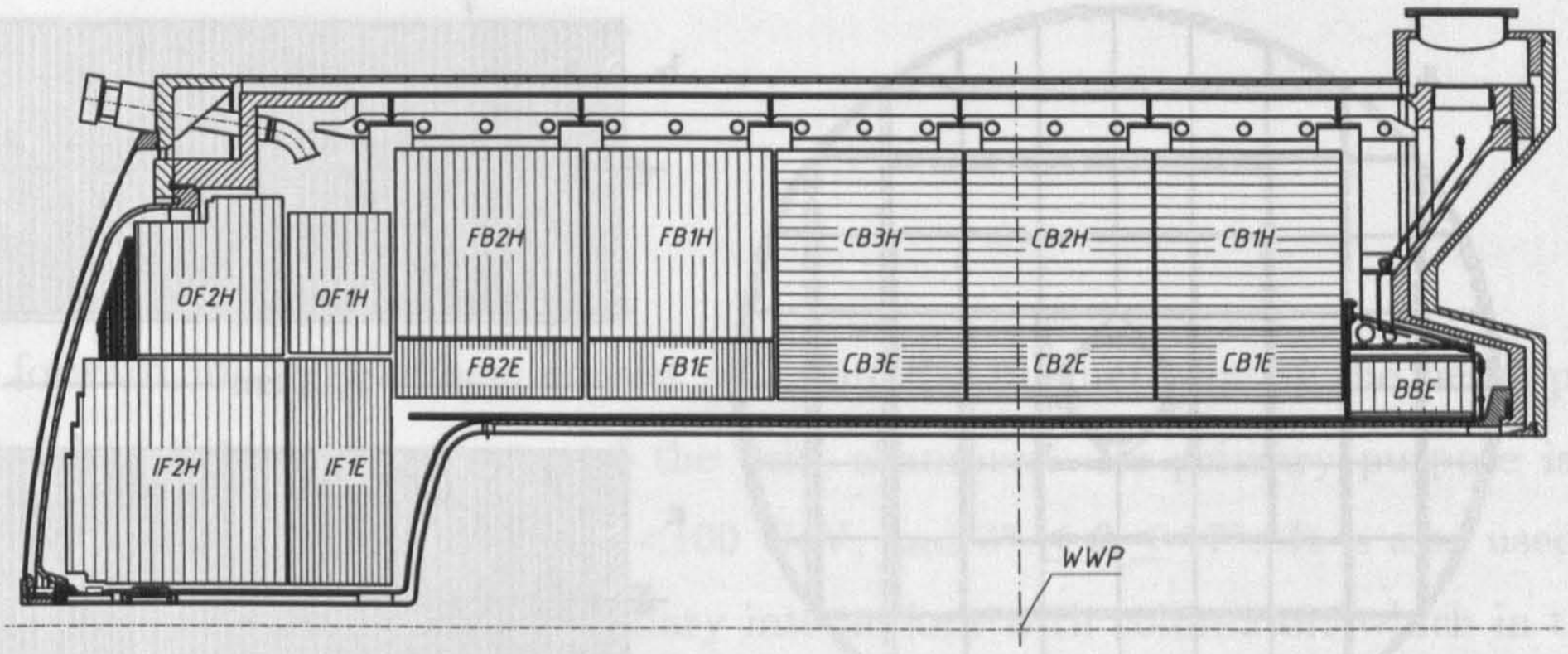

Figure 1.6: Diagram of the Liquid Argon calorimieter in the rz plane.

1.4.2 BEMC

The BEMC (shown in figure 1.7) is primarily required to trigger on, and measure the energy of, the scattered lepton in the Q^2 range $2 < Q^2 < 100$ GeV^2 and consists of 88 stacks, each composed of 50 lead-scintillator layers, 23 radiation lengths in depth. Photons from the scintillator are collected in two pairs of wavelength shifter bars on opposite sides of each stack, covering its entire length and read out by photo-diodes. The remaining sides have one short wave length shifter each covering only the last 15 layers so providing two-fold segmentation in z. This allows a discrimination between electromagnetic and hadronic showers. For electrons the resolution is determined to be $\sigma(E)/E \sim 0.39/E(\mathrm{GeV}) \oplus 0.10/\sqrt{\mathrm{E(GeV)}} \oplus 0.01$ where the first term is a noise contribution, the second is due to sampling fluctuations and the constant term arises from energy leakage from the stack. The BEMC energy scale is known to within 0.7%. The stacks have a depth of $\sim$1 interaction length leading to poor hadronic response. With 40% of hadrons failing to interact within the BEMC, and those that do typically losing 45% of their energy, the hadronic resolution, even when combined with information from the tail catcher behind the BEMC, is $\sigma(E)/E \sim 0.8/\sqrt{E(\mathrm{GeV})}$.

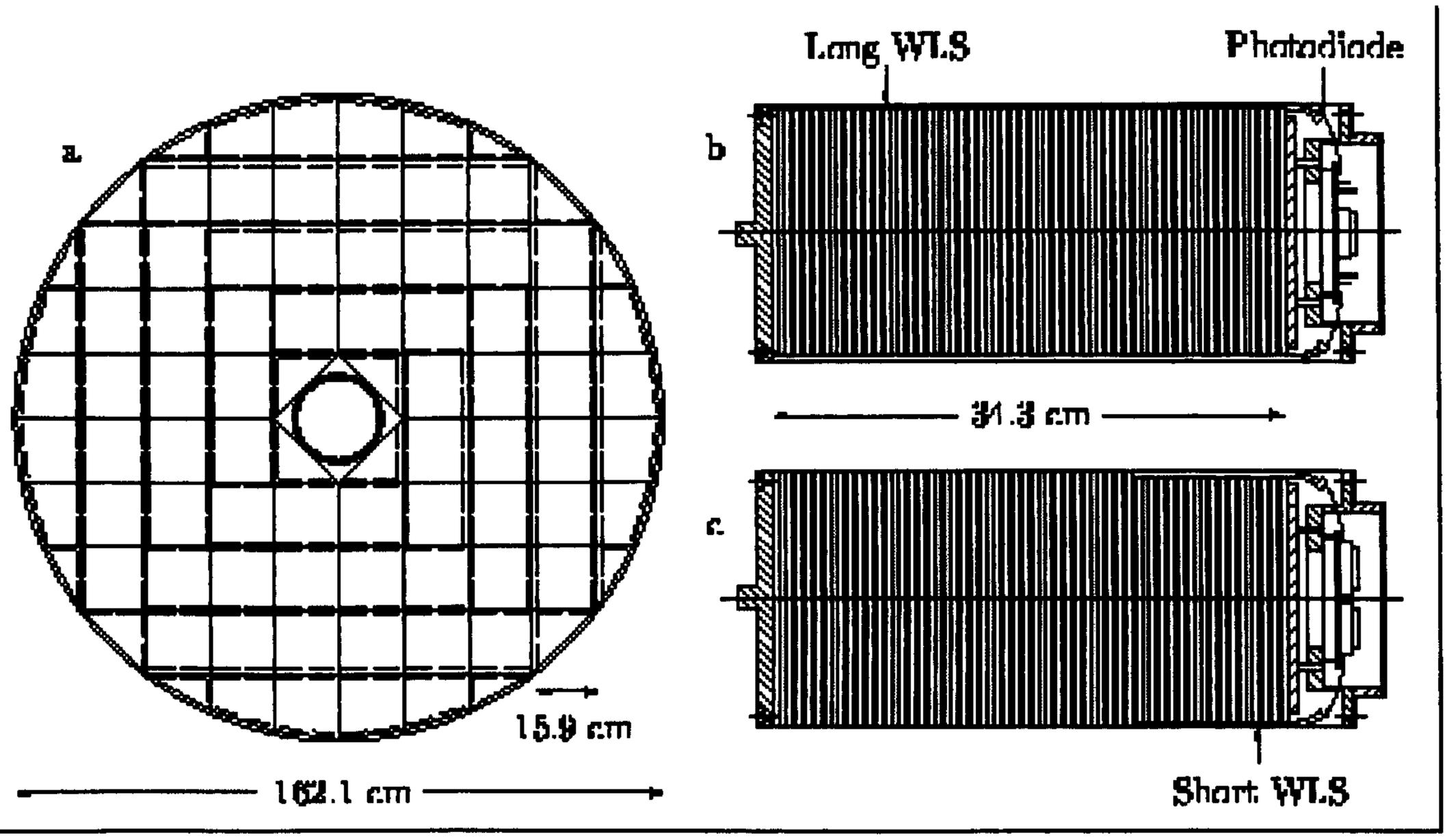

Figure 1.7: Transverse section of the BEMC. Also shown are two views of an individual calorimeter stack.

1.4.3 Plug Calorimeter

In the forward direction surrounding the beam-pipe the plug, a copper/silicon calorimeter, covers the angular range $0.7° \leq \theta \leq 3.5°$. It consists of 9 layers of copper absorber and silicon detector with depth of 4.3 interaction lengths. Its design aim was to minimise losses of transverse momentum to allow better kinematic reconstruction from charged current DIS events, however it has proved particularly successful in the selection of diffractive events which are required to have no energy in the forward direction (see section 4.2). The energy resolution (as determined from data and Monte Carlo simulation) is $1.5/\sqrt{E(GeV)}$.

The Plug is required to operate in a region of very high energy density. The harsh conditions have lead to radiation damage of the detector and an energy resolution which does not approach the design specification.

1.4.4 Tail Catcher

The tail catcher measures the hadronic energy leakage from the LAr and the BEMC in the region $5° \leq \theta \leq 175°$ and has a depth of 4.5 interaction lengths. It uses the iron return yoke as absorber material interleaved with streamer tubes for muon track and hadronic shower detection. The hadronic energy resolution is determined

to be $1.5/\sqrt{E(\mathrm{GeV})}$.

1.5 Forward Muons

The forward muon chambers consist of a toroidal magnet around the beam-pipe sandwiched between two layers of the drift chambers. Its primary purpose is to detect energetic muons with $5< p <100$ GeV, and $3° \leq \theta \leq 17°$. It is also used to detect particles coming from secondary interactions with collimators which in turn are designed to protect the detector from synchrotron radiation [48].

1.6 Luminosity System

The luminosity measurement is made with the use of two low angle calorimeters for electron and photon detection (the electron tagger and photon tagger), located at $z = -33$ m and $z = -103$ m respectively, with resolutions of $0.1/\sqrt{E(\mathrm{GeV})}$. They measure the rate of Bethe-Heitler events which have a large and exactly calculable cross-section. The luminosity is then given by,

$$\mathcal{L} = \frac{N_{tot} - \frac{I_{tot}}{I_{pilot}} N_{pilot}}{\sigma A_{BH}} \tag{1.1}$$

where N_{tot} is the total number of events, N_{pilot} is the number of background events in pilot bunches (mainly coming from $eA \longrightarrow eA\gamma$ and is approximately 10% of N_{tot}), I_{tot} (I_{pilot}) are the electron beam currents in the colliding (pilot) bunches, σ is the calculated cross-section and A_{BH} is the acceptance and efficiency of the system. Offline corrections are applied to the luminosity measurement for proton satellite bunches which appear at 5ns intervals with respect to the the main bunch, and arise from mis-timed protons in the pre-acceleration and injection phases. The luminosity is measured to 4%. Photo-production events are triggered using the electron tagger and no signal from the photon tagger, combined with triggers from other detectors since the contaminating cross-section from bremsstrahlung events is so high.

1.7 Scintillation Counters

Scintillators are used to provide a fast veto on proton beam induced background coming from interactions before the beam reaches the detector. The ToF is composed of two walls of scintillating plastic sandwiched between lead plates to protect it from synchrotron radiation, and is located behind the BEMC at $z \simeq -2$ m. This position optimises geometric acceptance and time discrimination, since particles from ep interactions and proton background have a mean separation of $\sim$13 ns compared to the ToF timing resolution of 4 ns. The ToF veto is used at the Level 1 trigger to remove the background events and gives a 99% decrease in trigger rates and therefore a significant improvement in efficiency and dead-time. Two further scintillators, located at $z = -6.5$ m, and $z = -8.1$ m, known as the large and small veto walls respectively, further suppress background mainly from halo muons.

1.8 Trigger and Readout

The rate of ep collisions at HERA is swamped by the rate of background interactions with residual gases, stray protons, synchrotron radiation, and cosmic muons. Table 1.1 shows the typical rates of interactions at average 1994 luminosity. A sophisticated trigger system is required for fast and efficient background removal without loss of physics events of interest. This is further complicated by the small bunch crossing interval of 96 ns. For comparison typical time-scales are given in table 1.2. The trigger and read out system is pipelined so that all the information of each sub-detector from the last 24 bunch crossings is stored whilst a decision is made by the central trigger logic (CTL) at Level 1. Trigger elements are combined from detector components to form sub-triggers which are used to select classes of physics events or useful events for monitoring purposes. When a sub-trigger condition is satisfied, a counter is incremented and the event is read out once the counter reaches its "pre-scale" value. The pre-scales for each sub-trigger are used to downscale events with large rates, however classes of physics events are not pre-scaled if possible, whereas monitor events are often pre-scaled for use in efficiency studies and background monitoring.

To initiate readout of data (typically 2.4 μs after the event occurred), the CTL sends

a *L1keep* signal to all sub-detector branches. At this point the pipelines are stopped and dead-time begins as data cannot be taken during read out. For this reason it is desirable to have high background rejection rates at Level 1.

Event information is then zero suppressed and passed to further trigger levels which have time to make more sophisticated decisions on whether to keep the event or not. However, the Level 2 and Level 3 triggers were not implemented in 1994. Once all compressed sub-detector information is available to the central event builder module, the pipelines are freed resulting in a dead-time of typically 1-2 ms. The data is passed to the Level 4 trigger which performs a simplified version of the full event reconstruction and applies cuts to remove remaining background. Events surviving Level 4 are written to tape at ~10 Hz. Additionally 1% of Level 4 rejected events are kept for monitoring. The permanent data is then fully reconstructed offline at Level 5 where physics and monitor events are separated into different data streams. Further cuts are applied on the physics classes and these data are finally stored in reduced format as Data Summary Tapes available for analysis.

beam gas interactions		50 kHz
cosmic μ in barrel		700 Hz
tagged γp	1.6 μb	2.3 Hz
total $c\bar{c}$	1 μb	1.4 Hz
DIS low Q^2	150 nb	0.2 Hz
DIS high Q^2	1.5 nb	0.1 min^{-1}
Charged Current DIS $P_t \geq 25$GeV	50 pb	0.3 h^{-1}
W production	0.1 pb	0.1 d^{-1}

Table 1.1: Rates and cross-sections at average 1994 luminosity.

Width of proton bunch	1.1 ns
Time to next satellite bunch	5 ns
Flight time to ToF	6 ns
Flight time to barrel muon system	20 ns
Bunch crossing interval	96 ns
Longest drift time in CJC	1 μs
Integration time of LAr pre-amplifier	1.5 μs
Delay of first level trigger	2.5 μs
Front end read-out time	~ 1 ms

Table 1.2: Time scales at HERA and H1.

Chapter 2

Physics at the HERA Collider

2.1 Introduction

In this chapter an overview of DIS physics relevant at HERA is given, with an emphasis on the results that have emerged in the first three years of running. The kinematics of DIS are given, followed by a short discussion of structure function measurements, and analyses of the hadronic final state. Diffractive physics is introduced with recent results of the H1 measurement of the pomeron structure function. Although HERA was designed primarily for the study of DIS, it nevertheless provides an ideal opportunity for the analysis of a wide range of other physics processes. These include "photo-production", in which a quasi-real photon ($Q^2 \sim 0$) interacts with the proton allowing measurements of photon structure to be made, and searches for exotic particles predicted by extensions to the standard model. The analyses of these areas will not be described in the following chapter and the reader is instead referred to [3,4] for details.

2.2 DIS Kinematics

In NC DIS the process of interest is the inelastic scattering:

$$e + p \rightarrow e + X \tag{2.1}$$

where X represents the hadronic final state. In EW the interaction may be mediated by either a photon, or the Z^0 boson and has a propagator term in the amplitude, T, of the form

$$T \sim \frac{1}{Q^2 + M^2} \tag{2.2}$$

where M is the mass of the vector boson. Thus it can be seen that Z^0 exchange is only significant when Q^2 is of the same order as $M_{Z^0}^2 \sim 10^4$ GeV^2 or larger. Charged current processes mediated by large mass $W^{\pm}$ bosons are similarly suppressed.

The deep inelastic scattering interaction to lowest order in α, is shown in the Feynman diagram of figure 2.1. Several notable features of a typical DIS event can be seen in the display of an event in figure 2.2. The proton beam enters from the right and the electron beam from the left. A lone track in the backward direction gives rise to an energetic electromagnetic cluster in the BEMC and is identified as the scattered electron. The cluster of tracks in the central part of the detector comes from the struck quark scattered out of the proton. These tracks deposit most of their energy in the outer (hadronic) section of the LAr calorimeter indicating the hadronic nature of the particles. Finally, significant energy deposits can be seen in the forward direction around the beam pipe which suggest the fragmentation of the proton.

Let the incident beam particles be denoted by the four-vectors $\mathbf{p}$ and $\mathbf{k}$ for the proton and electron respectively, and the scattered lepton by $\mathbf{k'}$. The 4-momentum transfer from the electron to the proton system via exchange of a virtual electroweak gauge boson is given by:

$$\mathbf{q} = \mathbf{k} - \mathbf{k'} \tag{2.3}$$

Since the virtual exchange has space-like 4-momentum, ie. $q^2 < 0$, it is convenient to define a positive variable, Q^2 as

$$Q^2 = -q^2 \tag{2.4}$$

The fixed centre of mass energy of the ep system (neglecting particle masses), $\sqrt{s}$, is given by

$$s = (\mathbf{p} + \mathbf{k})^2 \approx 2\mathbf{k} \cdot \mathbf{p} = 4E_e E_p \tag{2.5}$$

and achieved a value of 300 GeV with the 1994 beam energies of 27.6, and 820 GeV for electron and proton beams respectively. This is equivalent to a 45 TeV electron beam in a fixed target experiment. The invariant mass, W, of the hadronic system, X, is given by

$$W^2 = (\mathbf{p} + \mathbf{q})^2 \tag{2.6}$$

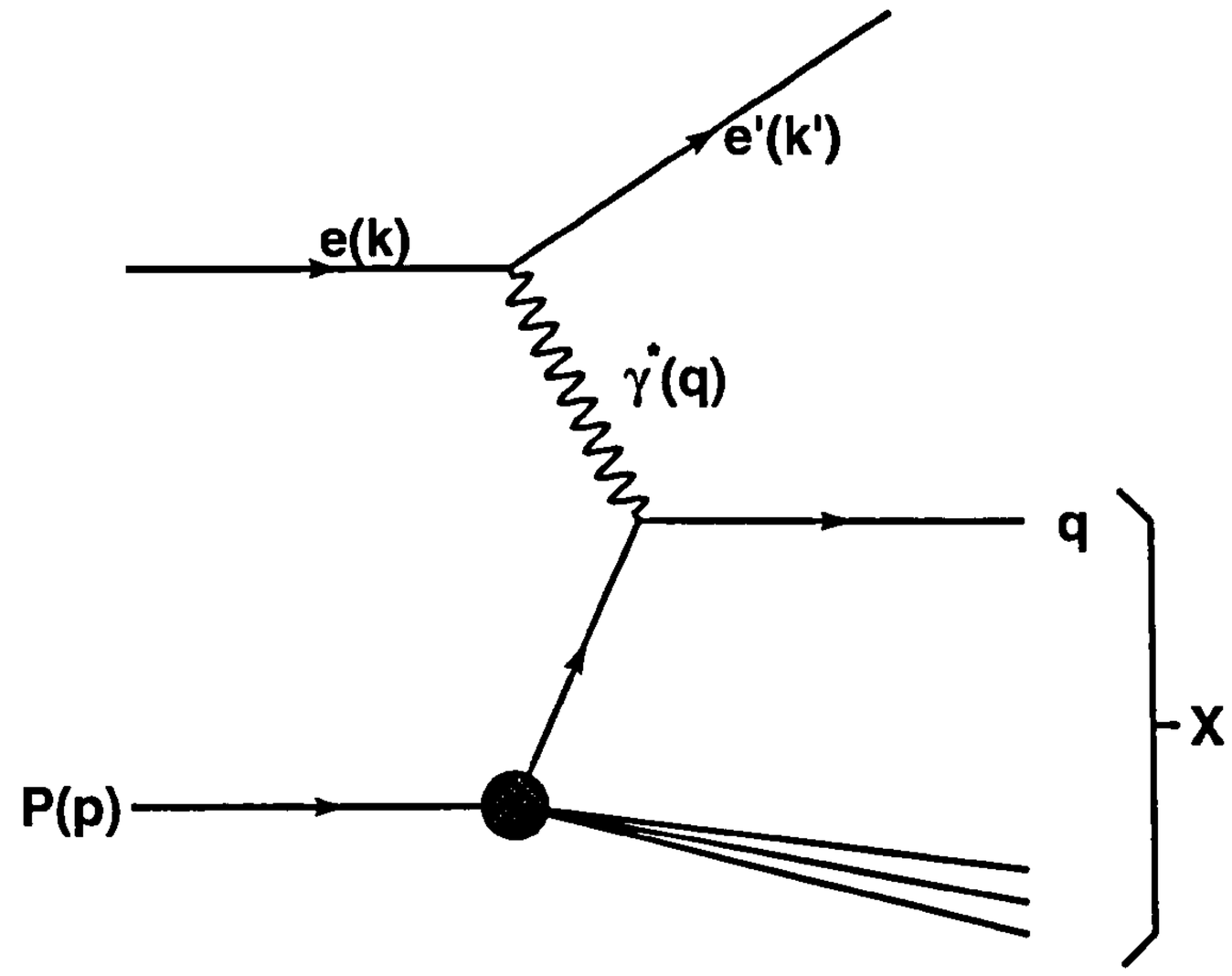

Figure 2.1: Feynman diagram representing a DIS event.

The Björken scaling variables x and y are convenient Lorentz invariant quantities defined as

$$x = \frac{Q^2}{2\mathrm{p}\cdot\mathrm{q}} \tag{2.7}$$

$$y = \frac{\mathrm{p}\cdot\mathrm{q}}{\mathrm{p}\cdot\mathrm{k}} \tag{2.8}$$

where in the parton model x may be interpreted as the fraction of the proton momentum carried by the struck quark in the infinite momentum frame of the proton, and y is the fractional energy loss of the electron in the proton rest frame. Both variables take values between 0 and 1. Assuming azimuthal symmetry only two of the above variables are required to describe the DIS process at fixed $\sqrt{s}$ leading to the useful relation between them:

$$Q^2 = sxy \tag{2.9}$$

In the approximation of massless particles W^2 may be written as:

$$W^2 \approx Q^2\left(\frac{1-x}{x}\right) \tag{2.10}$$

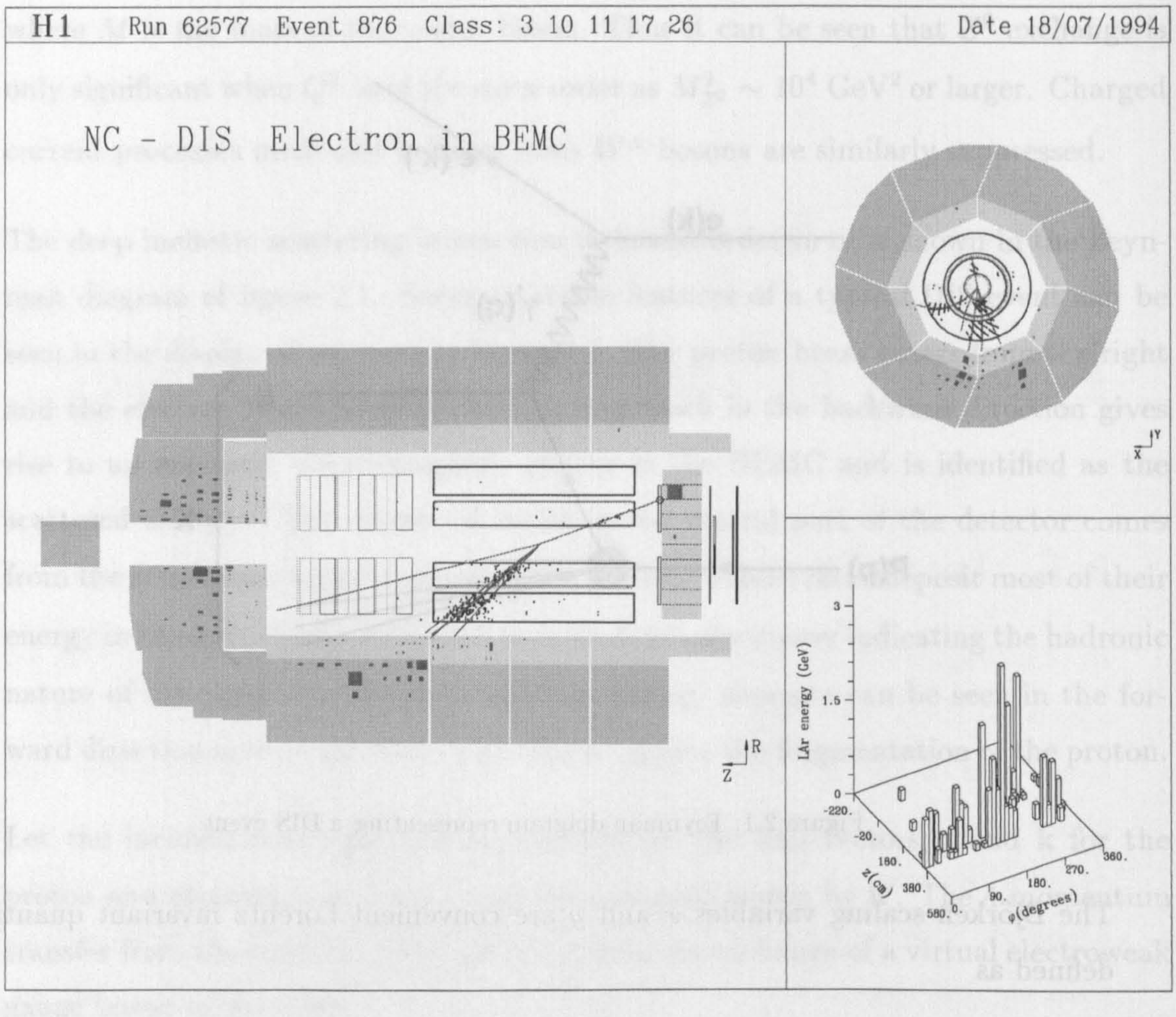

Figure 2.2: A neutral current DIS event taken by the H1 detector.

and

$$x \approx \frac{Q^2}{Q^2 + W^2} \tag{2.11}$$

Since the cross-section is largest for $Q^2 \ll W^2$, values of $x \sim 10^{-5}$ are obtainable, two orders of magnitude smaller than previous fixed target experiments. Figure 2.3 shows the x, Q^2 plane with regions accessible at HERA compared to the regions explored in fixed target experiments.

2.3 Proton Structure Functions

The differential cross-section for inclusive ep scattering in NC DIS at low Q^2 [1] may be described by two *structure functions* F_2 and $2xF_1 = F_2/(1+R)$:

[1] For Q^2 of order M_z^2 an additional structure function xF_3 can no longer be neglected. This describes the parity violating process occuring via Z^0 exchange.

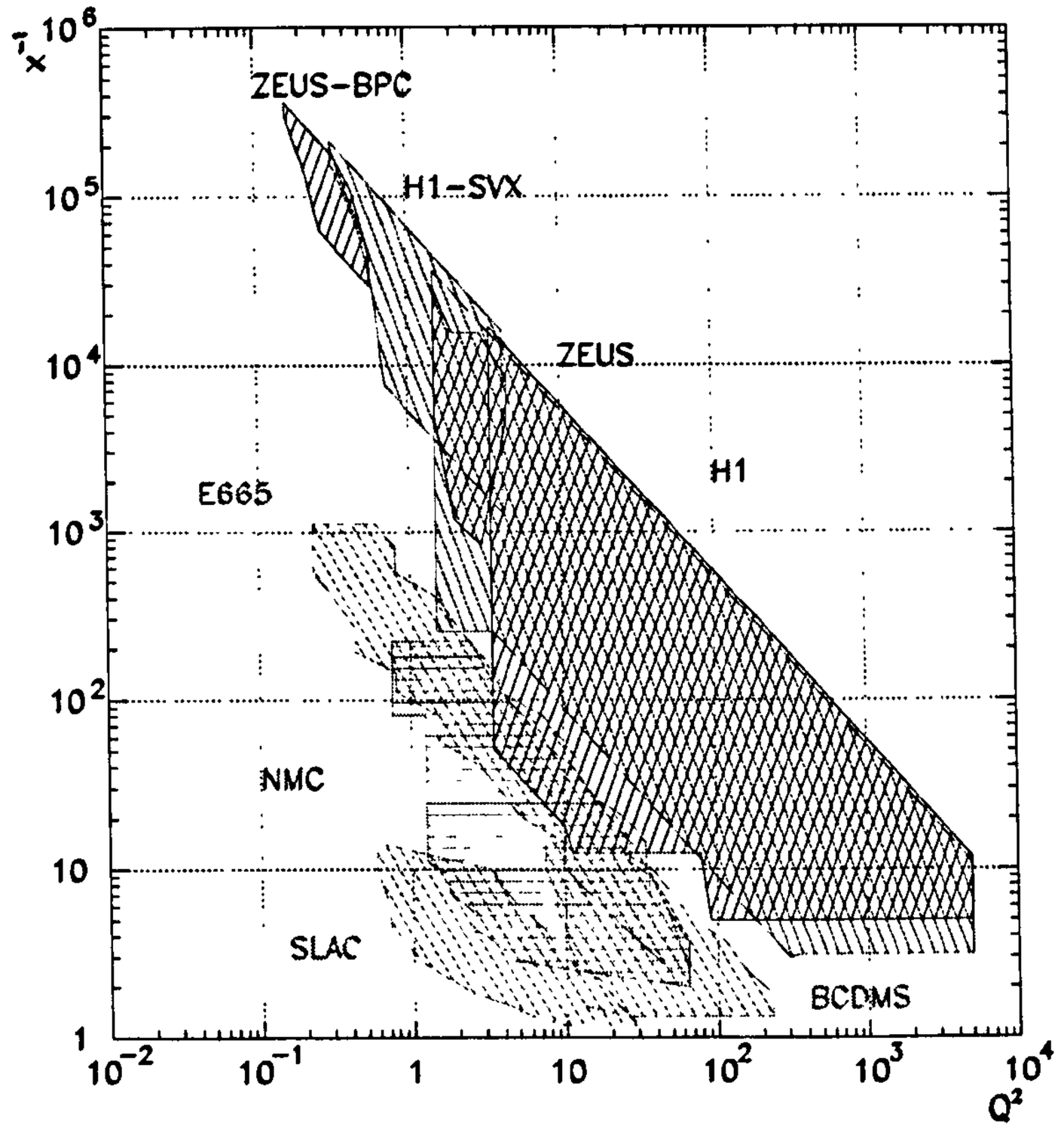

Figure 2.3: Range in x and Q^2 covered by the HERA detectors and fixed target experiments. H1-svx refers to data taken with a forward shifted vertex, and ZEUS-bpc refers to data taken with the new ZEUS beam pipe calorimeter, both of which allow a lower Q^2 to be attained.

$$\frac{d^2\sigma}{dxdQ^2} = \frac{2\pi\alpha^2}{xQ^4}\left[2(1-y) + \frac{y^2}{1+R}F_2(x,Q^2)\right] \tag{2.12}$$

where F_1 describes the cross-section from transversely polarised photons and F_2 the contribution from both longitudinal and transversely polarised photons, (σ_L and σ_T respectively). R is then the photo-absorption ratio:

$$R = \frac{\sigma_L(x,Q^2)}{\sigma_T(x,Q^2)} \tag{2.13}$$

In the limit $Q^2 \to 0$, i.e. as the photon becomes real, both σ_L and $R \to 0$ leading to the relationship

$$F_2(x,Q^2) = 2xF_1(x,Q^2) \tag{2.14}$$

known as the Callan-Gross relation [5], and implies that the proton constituents have spin $\frac{1}{2}$ from a consideration of helicity conservation. Previous experiments [6]

have measured R and found it to be small (~ 0.1) except at low x ($x < 0.02$), where QCD effects are responsible for the violation of the Callan-Gross relation. Although no measurement of R has been made at HERA[2], QCD extrapolations indicate that it contributes no more than ~8% to the differential cross-section at the largest y values [7]. Therefore a measurement of the differential cross-section is an almost direct measure of F_2 after application of small corrections (~10% at lowest x) for QED radiation[3].

Early measurements of F_2 from neutrino, and anti-neutrino scattering [8], revealed a structure that was consistent with a proton made up of three valence quarks at large x, and a sea of quark-anti-quark pairs at low x. The experimental observation of the Q^2 independence of F_2, or *scale invariant* behaviour allowed DIS to be viewed as elastic electron scattering on free, point-like partons [9].

Since photons couple only to quarks, F_2 may be written as

$$F_2(x) = x \sum_i e_i^2 q_i(x) \tag{2.15}$$

where $xq_i(x)$ is the momentum weighted *parton density function* (PDF) for quarks of flavour i, and charge e_i in units of the electron charge. Thus F_2 is dependent on the charge of the interacting partons. This was exploited to experimentally confirm the fractional charge assignments to the partons by comparing F_2 measurements of electron and neutrino scattering on nuclei. If partons have fractional charge the relationship between the neutrino and electron scattering nucleon structure functions is given by

$$F_2^{\nu N}(x) = \frac{18}{5} F_2^{eN}(x) \tag{2.16}$$

where the factor 18/5 is the reciprocal of the mean squared charge of u and d quarks in the nucleon. This was verified experimentally in [10].

The Callan-Gross relation, scaling behaviour of F_2, and the confirmation of fractionally charged constituents of the proton allowed partons to be identified as quarks.

[2]Estimates suggest a meaningful measurement of R could be made with ~10 pb^{-1} of luminosity at each of three proton beam energies.

[3]Corrections for the running of α, the electromagnetic coupling constant amount to $\sim 0.3\%$ over the Q^2 range $1.5 - 5000$ GeV^2.

This forms the basis of the quark-parton model (QPM) which is able to provide an accurate description of the data. However, further evidence indicates the incomplete nature of the model, and in particular the neglect of the role of gluons in proton structure. If quarks are the only constituents of the proton, then a momentum sum rule must be applicable, demanding that the sum of parton momenta equal the proton momentum:

$$\sum_i \int_0^1 x q_i(x) dx = 1 \tag{2.17}$$

The experimentally observed value is found to be 0.5 [11], implying that gluons carry half the proton momentum.

Experiments have shown that Björken scaling holds for moderate $x \sim 0.13$, though at other values scaling violations are evident showing a dependence on $\log Q^2$. This is understood in the framework of QCD where gluon bremsstrahlung or splitting takes place, eg. the processes $q \to qg, g \to q\bar{q}$, and $g \to gg$. Such structure is not resolved at low Q^2, and only becomes apparent as Q^2 increases. In addition the gluons themselves carry a colour charge thereby allowing gluon-gluon interactions. The consequence of this leads to the *running* of the dimensionless coupling constant, α_s, i.e. the dependence of α_s on the scale of the interaction (taken as Q^2 in DIS), such that α_s decreases with increasing Q^2. At large Q^2 this leads to the QCD property of *asymptotic freedom* where quarks may be considered as free and non-interacting. Conversely, at low Q^2, α_s is large and interactions between quarks increase, giving rise to the *confinement* property of quarks which binds them into colourless hadrons (hadronisation). The coupling constant has an energy dependence characterised by the quantity Λ_{QCD} ($\sim$ 270 MeV) which determines the energy scale at which perturbative QCD fails and the hadronisation stage begins.

The HERA measurements of F_2 are shown in figures 2.4, and 2.5. Figure 2.4 presents the H1 data as a function of x in bins of Q^2, covering three to four orders of magnitude in x and Q^2. Events with initial state QED radiation from the electron beam, and forward shifted vertex running allow data to be taken with $Q^2 < 5$. Lower energy data from the NMC and BCDMS collaborations are used to constrain the fits at high x. The data show a clear rise of F_2 at low x which increases with Q^2.

The solid lines represent a global QCD fit to the data. Figure 2.5 shows the data as a function of Q^2 in bins of x, allowing scaling violations to be seen above and below $x = 0.13$.

The scaling violations are predicted in perturbative QCD by the Altarelli-Parisi or DGLAP [40, 12, 13] evolution equations. These are a set of three coupled equations describing the splitting processes given above, and are dependent on the splitting probabilities, and the parton density functions. The PDFs are usually given at a starting scale of $Q_0^2 \sim 4$ GeV^2 and the equations are solved to give the PDFs at $Q^2 > Q_0^2$. Although no evolution in x is possible in the DGLAP framework, the equations are used to estimate low x behaviour by fitting and extrapolating high x data, to use as input at the starting scale. Many sets of parton density functions exist all differing in the starting distributions used.

The DGLAP mechanism operates within the leading log approximation in which only terms of order $\alpha_s^n \log^n Q^2$ are summed in the perturbative expansion of F_2. This approach has provided an accurate description of the data, though is expected to fail at low x where terms of order $\alpha_s^n \log^n 1/x$ become important.

The BFKL mechanism [14, 15] also uses the leading log approach and sums only the $\alpha_s^n \log^n 1/x$, and so should provide a better description of the data where the DGLAP evolution fails. However, present data at the lowest x do not favour BFKL evolution above DGLAP, and may be equally well described by DGLAP, or a mixture of both [16], though measurements of the hadronic final state show indications of a BFKL type component (see below).

The evolution mechanisms can be seen as the building of partonic cascades by the splitting of high x partons to low x partons with increasing Q^2 . Valence quarks, which dominate proton structure at high x, undergo gluon emission, whilst the sea quark (colour singlet) density is driven by the gluon density through the splitting $g \to q\bar{q}$ and so the rise of F_2 at low x may be seen as a rapid increase of the gluon density. Therefore, measurements of the gluon density at HERA are of particular interest.

The increase cannot go on indefinitely and at sufficiently low x, gluon recombination

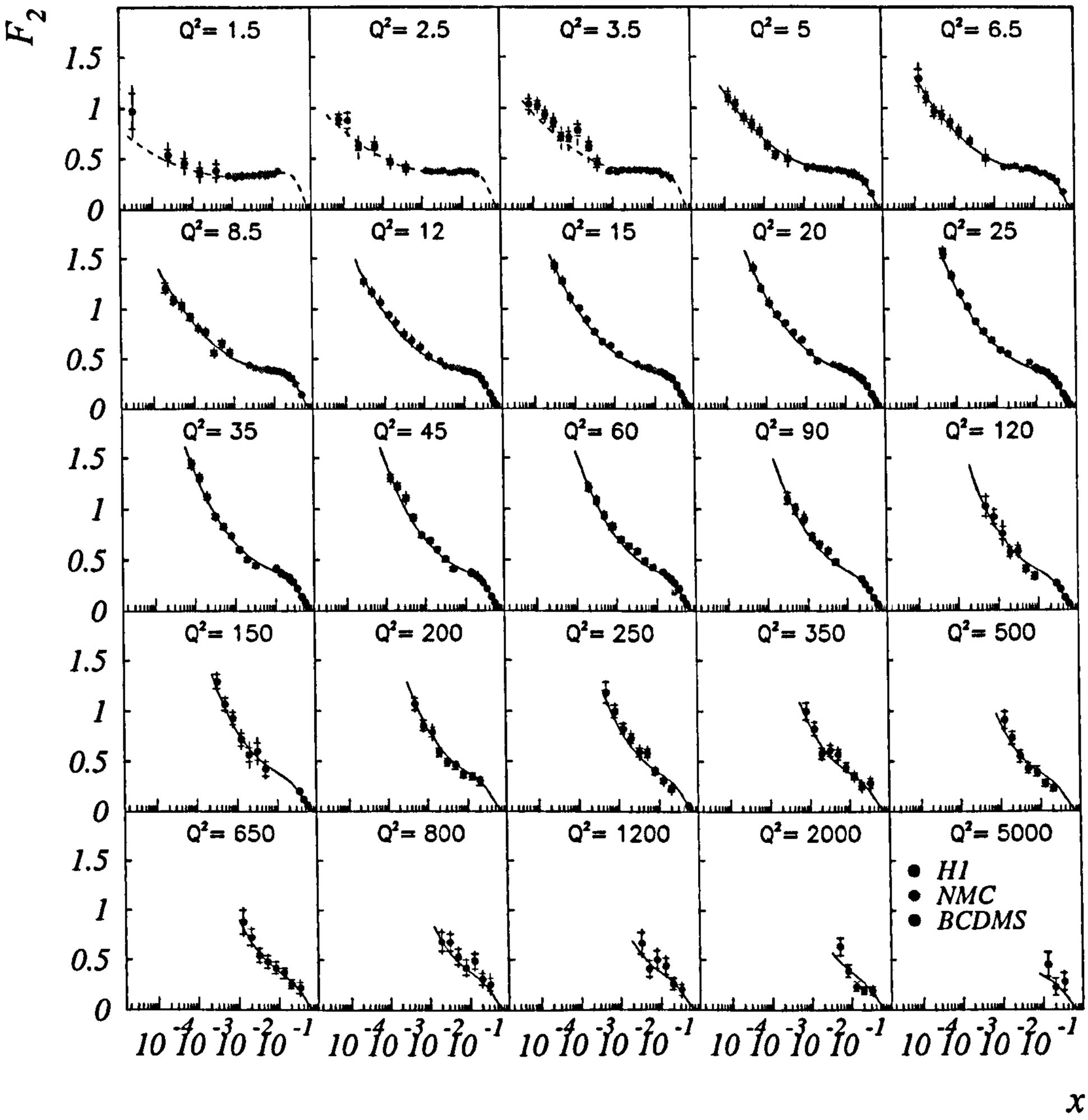

Figure 2.4: F_2 as a function of x showing H1 data annd lower energy fixed target data. The solid line is a NLO QCD fit for $Q^2 > 5$ GeV^2, and the dashed line is the "backwards" evolution of the fit at low Q^2.

effects (ie. $gg \rightarrow g$) must be taken into account. The GLR equation [17] is a first attempt to incorporate this process. Assuming a homogeneous gluon density within the proton, screening effects are expected to be small at HERA, however, if gluons "cluster" around the valence quarks, then the critical density may be reached at higher x and is known as the hotspot scenario [18–20]. Gluon recombination would manifest itself through a saturation of F_2, and since the HERA data exhibit an increase, described by DGLAP evolution (in which the effect is not modeled), it may be concluded that the phenomenon of screening is not visible in the HERA kinematic region. It has been argued [21], however, that F_2 is too inclusive a measurement, and greater sensitivity to screening effects may be obtained through an analysis of

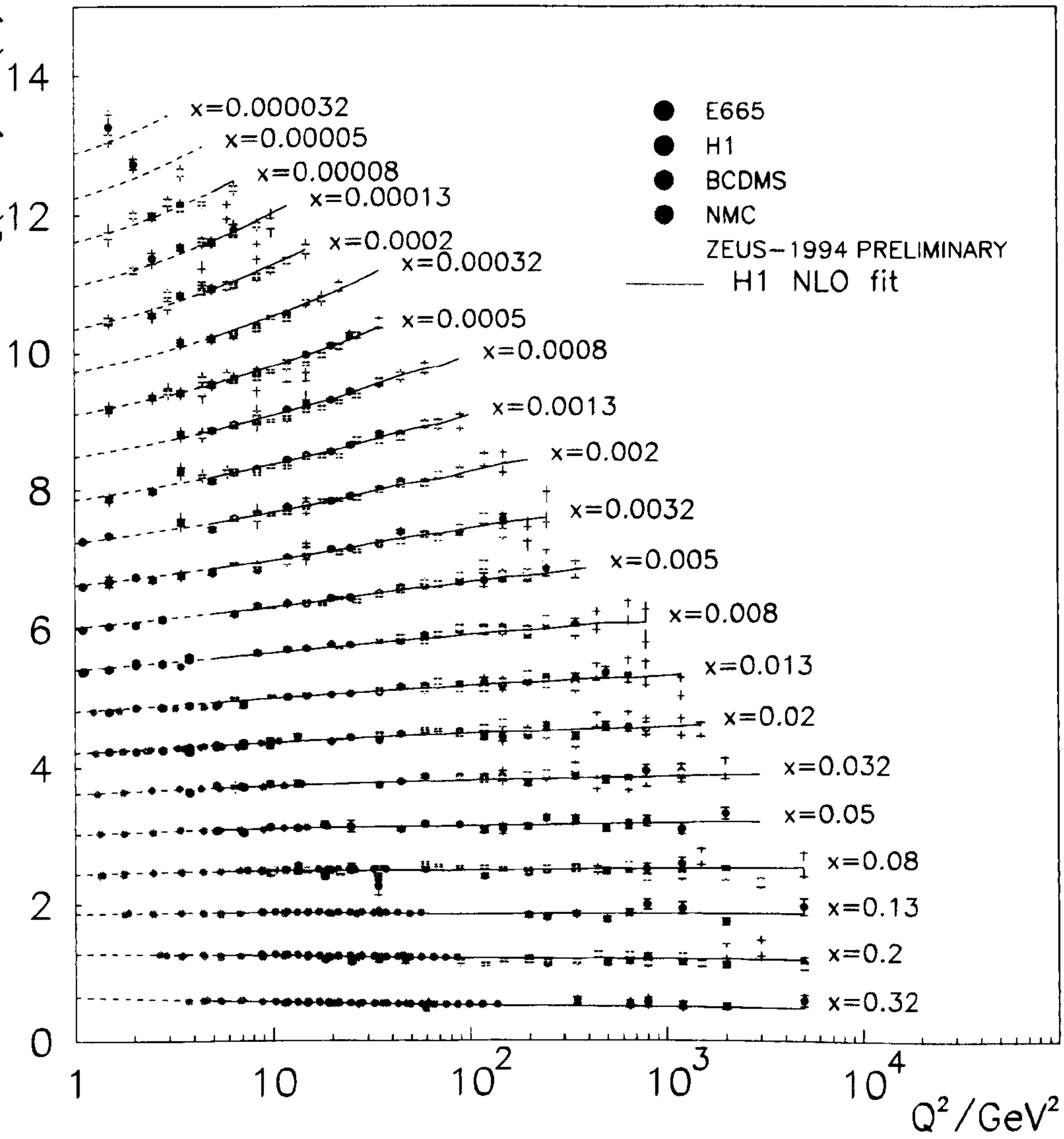

Figure 2.5: F_2 as a function of Q^2. A normalisation constant, c(x), is added to each bin in x for purposes of clarity, where c(x)=0.6(i-0.5) where i is the bin number, and is 1 for x=0.32.

the hadronic final state.

The gluon density can be obtained from F_2 using the method of Prytz [22] (to within a 10% approximation) whereby

$$\frac{\partial F_2}{\partial \log Q^2} \sim \int \alpha_s x g(x, Q^2) dx$$

or from QCD fits to F_2 [16]. Alternatively a direct measurement has been made by studying the rate of boson-gluon fusion (BGF) events in which the virtual boson interacts with a quark from a gluon having undergone the process $g \rightarrow q\bar{q}$, and leads to a two jet final state in the detector [24]. All three methods give compatible results

and show a sharply increasing density as x decreases, consistent with both DGLAP, and BFKL predictions [16]. The H1 determination of $xg(x)$ from a NLO QCD fit to the F_2 data is shown in figure 2.6.

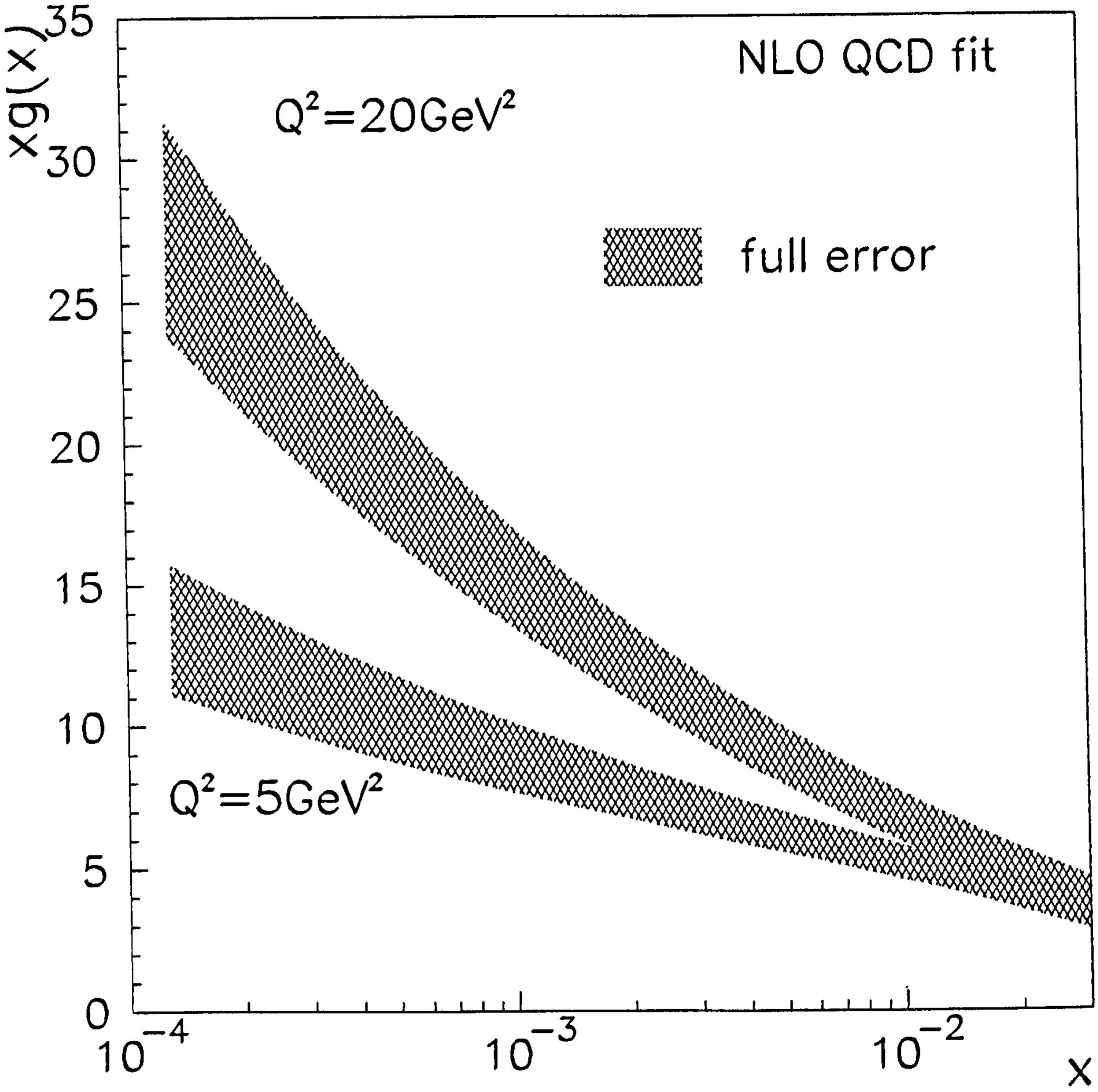

Figure 2.6: The H1 measurement of $xg(x)$ from a NLO fit to F_2 where x is the fractional gluon momentum with respect to the proton.

2.4 The Hadronic Final State

Measurements of the hadronic final state have allowed further details of DIS and QCD to be probed. These include the measurement of α_s by comparing the rates

of one and two jet events [4]. H1 results [25] show that α_s increases by a factor $\sim$3 over two orders of magnitude in Q^2 . Good agreement is obtained by extrapolating the results to the Z^0 mass and comparing with LEP measurements [26].

The Breit frame allows an excellent opportunity to compare events in DIS with one hemisphere of an e^+e^- event. The Breit frame is defined as that frame in which the virtual photon has no time-like component and has momentum Q. This corresponds (in the QPM) to an incoming quark of momentum $-Q/2$ colliding collinearly with the photon and rebounding with momentum $+Q/2$ into what is termed the *current* hemisphere, whilst the spectator system continues into the *target* hemisphere. An analysis of quark fragmentation functions [27] has shown that fragmentation is a universal phenomenon, independent of the mechanism by which the quarks are created.

Measurements of inclusive particle transverse momentum spectra and transverse energy flow have proved to be more sensitive to the evolution dynamics than F_2. In the DGLAP formalism partonic cascades , or "ladders" represent the evolution of parton densities up in Q^2 from the proton to the virtual photon (schematically shown in figure 2.7), and lead to a strong ordering in transverse momentum $k_{tn} \gg k_{tn-1} \gg ... \gg k_{t1}$, and weak ordering in fractional longitudinal momentum with respect to the proton, $x_1 > x_2 > ... > x_n$. However, in the BFKL picture there is no ordering in k_t, and strong ordering in x. Studying the forward region, away from the current region corresponds to looking further down the ladder towards the proton. Therefore it is expected that BFKL dynamics should generate more transverse momentum in the forward direction than DGLAP, and at low x and Q^2 such a discrepancy is observed in the data [28, 29], though it should be noted that the Monte Carlo comparisons are not made with a true BFKL calculation.

Events with charm quarks may be identified by tagging D^0, and D^* mesons. These events have been used by H1 to determine the charm production mechanism for the first time in ep collisions [30]. The analysis finds that within the HERA kinematic region, charm is produced predominantly by BGF events, and quotes a mean ratio of $F_2^c/F_2 = 0.237 \pm 0.021^{+0.043}_{-0.039}$, where F_2^c is the contribution of F_2 coming from

[4] An analysis of jet rates may be used to extract either α_s, or the gluon density, the other being taken from Monte Carlo models.

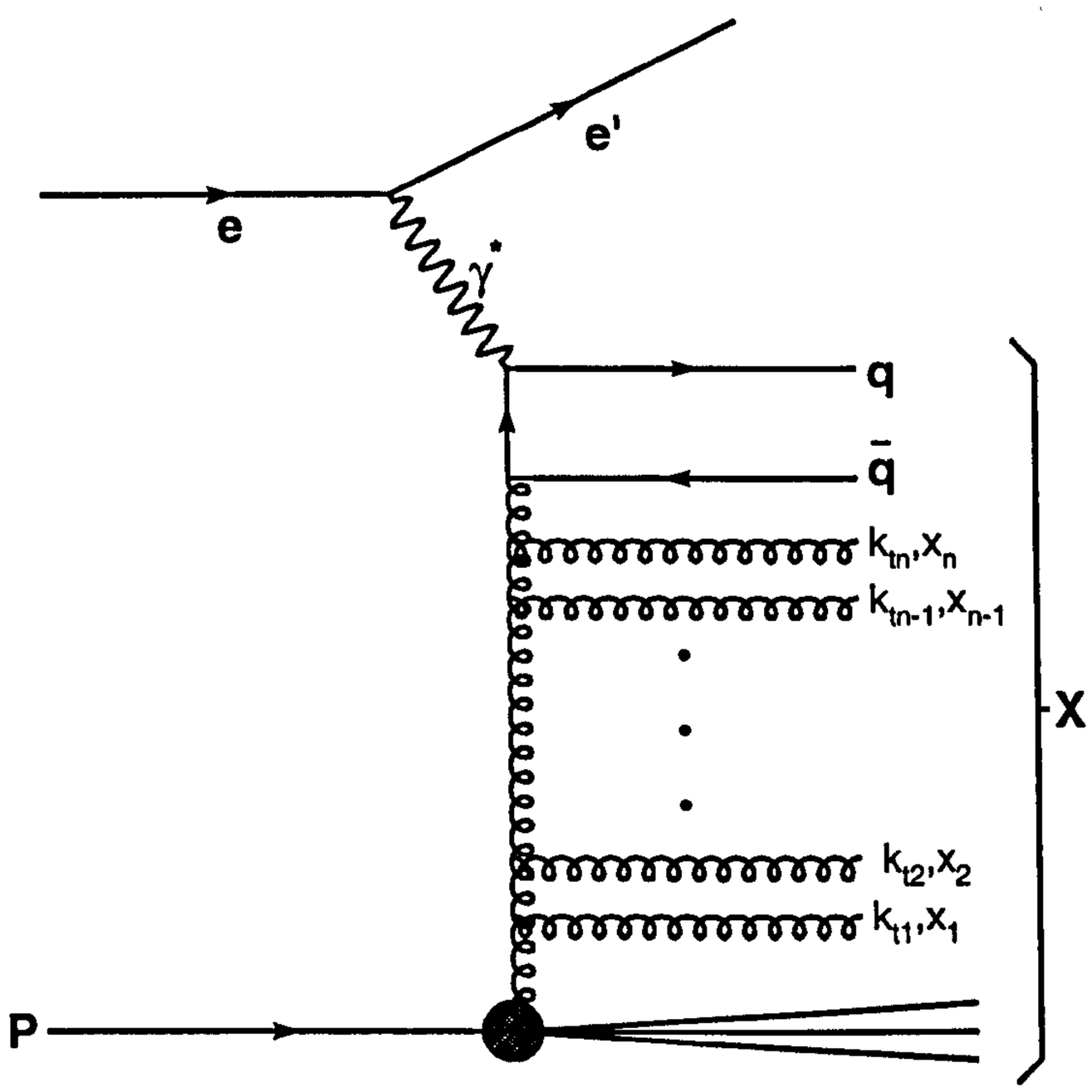

Figure 2.7: Schematic representation of partonic evolution in a DIS event.

charmed events. This is an order of magnitude larger than previous lower energy data, and indicates a slightly larger rise of the gluon density than predicted by the QCD fits of F_2.

2.5 Diffractive DIS Kinematics

In diffractive DIS no signals of proton fragmentation are seen in the main detector, and yet such events are certainly deeply inelastic in that they have a large Q^2. Such an event is shown in figure 2.8 to be compared with the event of figure 2.2. The diffractive event has a scattered electron detected in the BEMC, and a central hadronic "jet", but no activity forward of the jet. The lack of hadronic activity in a large region of rapidity around the proton suggests a colourless exchange between the photon and proton. However, this does not exclude meson exchange, pions for example. Since $Q^2 >> t$ the virtual photon may be pictured as probing the structure of the exchanged object, and, after defining suitable kinematic variables, a structure function can be defined analogous to the proton case. The quantities are shown in figure 2.9, and are M_X , and M_Y , the masses of the photon and proton dissociating states respectively, t, the momentum transfer at the proton vertex, $x_{I\!P}$, the fraction

of the proton momentum carried by the exchange, and β, the fractional momentum of the struck quark with respect to the momentum of the exchanged object. The definitions of $x_{I\!P}$, β and t are

$$x_{I\!P} = \frac{Q^2 + M_X^2}{Q^2 + W^2} \tag{2.18}$$

$$\beta = \frac{Q^2}{Q^2 + M_X^2} \tag{2.19}$$

$$t = (\mathbf{p} - \mathbf{Y})^2 = (\mathbf{q} - \mathbf{X})^2 \tag{2.20}$$

where $x = \beta x_{I\!P}$.

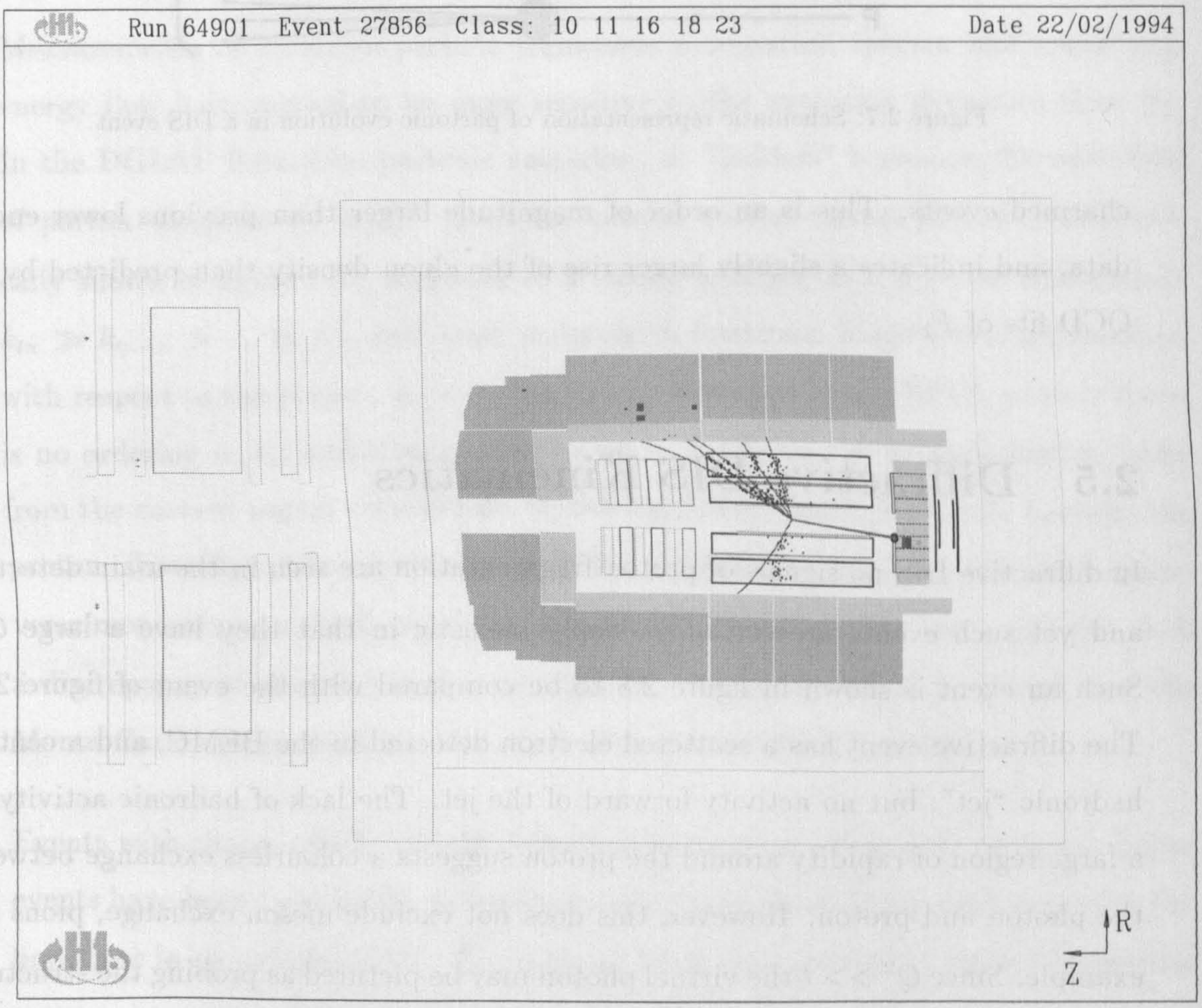

Figure 2.8: A diffractive neutral current DIS event as seen in H1.

The four dimensional differential cross-section, neglecting weak vector bosons, and a longitudinal polarised photon component is related to the structure function by

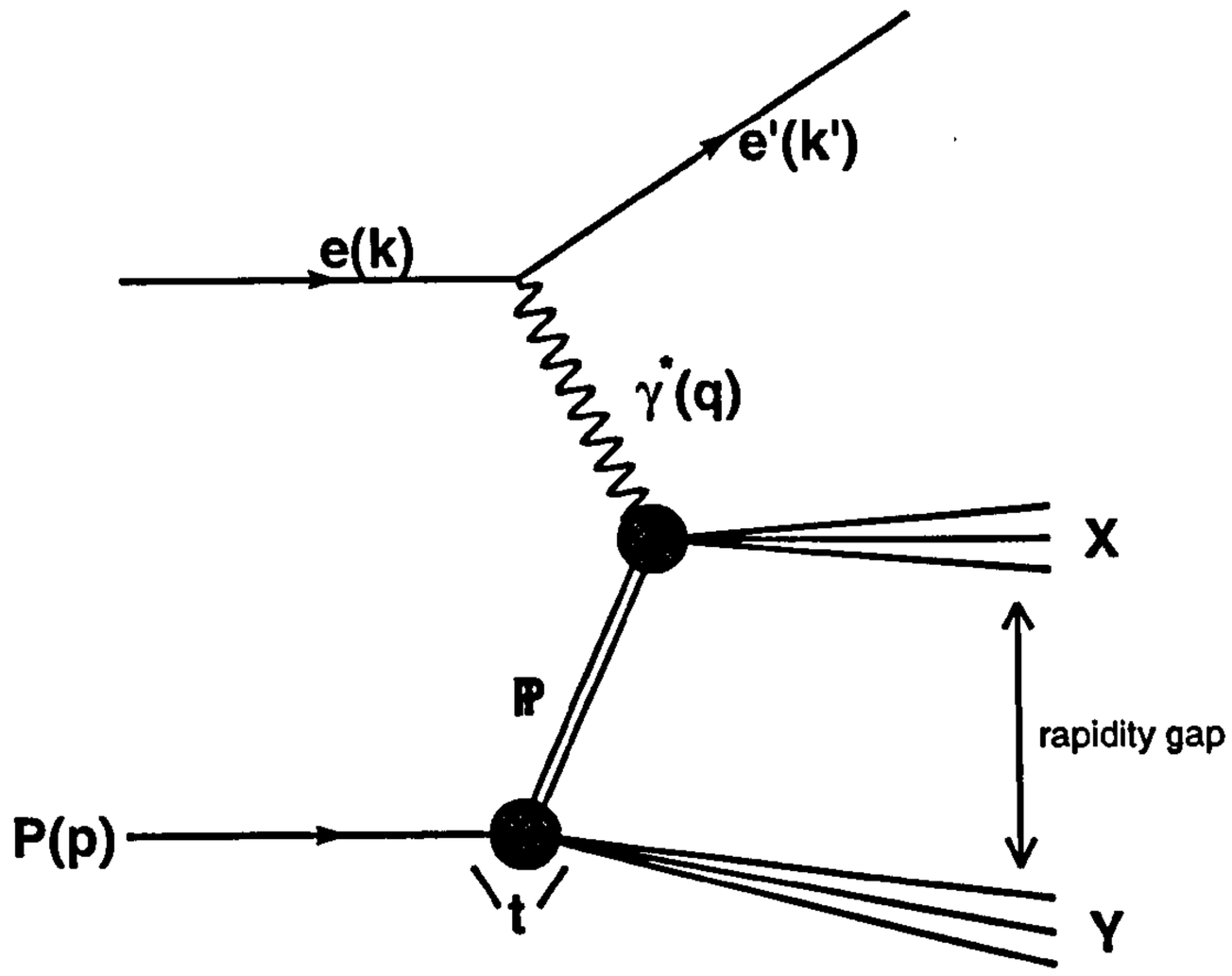

Figure 2.9: Feynman diagram representing a diffractive DIS event.

$$\frac{d^4\sigma^D(ep \to eXY)}{d\beta dQ^2 dx_{I\!P} dt} = \frac{4\pi\alpha^2}{\beta Q^4}(1 - y + \frac{y^2}{2}) F_2^{D(4)}(\beta, Q^2, x_{I\!P}, t) \qquad (2.21)$$

The quantity $|t|$ is generally small and not well measured with the 1994 detector configuration[5] and so all HERA measurements to date have integrated over t giving a three dimensional structure function. If the exchanged object behaves like a hadron, then the structure function is expected to be independent of the flux, and therefore of $x_{I\!P}$ and t, giving a factorised function:

$$F_2^{D(3)}(\beta, Q^2, x_{I\!P}) \to F_2^{D(2)}(\beta, Q^2)(\frac{1}{x_{I\!P}})^{2\alpha(t)-1} \qquad (2.22)$$

The explicit $x_{I\!P}$ dependence on the quantity $\alpha(t)$ is the expectation from the pre-QCD Regge formalism. Regge theory arose as an attempt to understand hadronic reactions at low momentum transfer, where α_s is small, and perturbative techniques fail [6]. It treats low t processes as a sum of exchange contributions from virtual

[5] Detectors at very low angles within the beam pipe are required. Two such components were installed in 1994/95 at z=81 m, and z=90 m with a further two stations planned for installation in 1997 [31,32].

[6] For an excellent introduction and review of Regge phenomenology the reader is referred to [33].

mesons with appropriate quantum numbers which are found to occupy linear "trajectories" in angular-momentum–mass squared space, denoted by $\alpha(t) = \alpha(0) + \alpha' t$, where α is the real part of a complex and continuous generalisation of angular momentum. At asymptotically large s, it predicts elastic hadron cross-sections of the form

$$\frac{d\sigma}{dt} \sim s^{2\alpha(t)-2} \tag{2.23}$$

which succesfully relate t channel resonances with the t dependence of of the cross-section for crossed s channel scattering. The optical theorem relates the total and elastic cross-sections such that $\sigma_{tot} \sim s^{\alpha(0)-1}$. Measurements of hadronic collisions have shown that cross-sections increase with s, implying an exchange component with $\alpha(0) > 1$, though meson trajectories have $\alpha(0) \sim 0.5$ [34]. The *pomeron* ($I\!P$) was postulated to overcome this difficulty and was required to have vacuum quantum numbers so as to describe the universal behaviour of hadronic cross-sections at large s. The pomeron trajectory as measured at hadronic colliders is given by $\alpha_{I\!P}(t) = 1.085 + 0.25t$ [34]. The relatively small slope implies the existence of a spin 2 resonance at large mass.

The preliminary H1 measurement of $F_2^{D(3)}$ indicates approximate scale invariance, though a rise with increasing Q^2 upto the largest β values suggests a large gluon component of the pomeron [35]. DGLAP based QCD fits to the data have shown that the structure is dominated by gluons carrying ~80% of the momentum at Q^2=2.5 GeV^2 near $\beta \sim 1$.

Chapter 3

Monte Carlo Models

Monte Carlo (MC) event generators are essential tools in the analysis of the data. They are models of the underlying physics processes studied at particle colliders and represent the best knowledge we have. Yet no Monte Carlo is without its deficiencies and is typically unable to describe all aspects of the data. A good detector simulation is also necessary in order to be able to use Monte Carlo models to correct the data for effects such as acceptance, efficiency and resolution smearing.

The Monte Carlo generators used in this analysis all employ the same framework to model DIS events. First an exact matrix element is calculated to describe the hard scattering sub-process. QCD processes to first order in α_s are included in the matrix element. Higher order QCD emission is then simulated using approximate methods until the partons have "evolved" to some low virtuality, typically $\sim$ 200 MeV. At this point a hadronisation model is used to form hadrons from the partonic final state, and to model the decays of unstable particles. At H1 particles are defined stable if they have a lifetime greater than 10^{-8} s. This stage of the model is referred to as the generator level and represents what may be seen of a DIS event with a perfect detector. Data, corrected for detector inefficiencies may be compared to generator level Monte Carlo to search for signals of new physics. Corrections to the data are obtained through use of reconstructed Monte Carlo. This involves further processing of the generator level information to simulate the detector in detail. Particles are tracked through the detector volume simulating interactions with dead material, and detector response in active regions. The H1 detector simulation program, H1SIM, is based on the CERN package GEANT [46]. After simulation the events are passed through the same reconstruction program as real data. By comparing data at generator and reconstruction levels, resolutions, efficiencies, and

acceptances may be determined with an accuracy dependent on the accuracy of the detector simulation.

Non–diffractive neutral current DIS events are modeled using the generator LEPTO [38] to calculate the electro-weak matrix element which describes $eq \rightarrow eq$ elastic scattering. This simple picture of DIS is known as the quark parton model (QPM), however, such processes do not account for QCD effects which are large at small x. Thus exact matrix elements to first order in α_s are used to describe the $\gamma^* q$ interaction. This allows the inclusion of two further processes which are shown in figures 3.1 and 3.2. The first describes "hard" gluon emission from the initial, or struck quark and is known as a QCD Compton (QCDC) event. The second process allows gluon contributions to DIS, whereby a gluon splits into a $q\bar{q}$ pair, one of which couples to the virtual photon. These type of events are known as Boson Gluon Fusion events (BGF). Further soft emission is described by either the colour dipole model (CDM) [39] as implemented by ARIADNE [41], or the parton shower approach. In the CDM, partons are emitted from a chain of independently radiating dipoles starting with a dipole formed between the struck quark, and the extended proton remnant. In the parton shower approach soft QCD emission is generated in the leading log approximation where the Altarelli-Parisi equations are used to describe the probability of a parton with momentum p splitting into two partons with momentum zp, and $(1-z)p$. Parton showers need to be "matched" to the matrix elements so as to avoid double counting of hard radiation. The combination of matrix elements with matched parton showers is referred to as the MEPS model, whilst matrix elements and CDM is referred to as MEAR.

To study the effects of QED radiation the generator DJANGO [36] is used which combines the generators HERACLES [37] and LEPTO. The former allows the inclusion of $\mathcal{O}(\alpha)$ processes including real photon emission from the electron as well as virtual electro-weak corrections.

The Monte Carlo used to model the diffractive DIS data sample is RAPGAP [42]. The model uses parton density functions taken from leading order DGLAP QCD fits to the measured pomeron structure function $F_2^{D(3)}$ [43]. As with LEPTO, exact matrix elements are used to calculate first order QCD radiation, with additional

radiation incorporated using either CDM (referred to as RAPA), or parton showers (RAPP). In addition RAPGAP includes virtual electro-weak effects to first order and real photon emission.

All Monte Carlos used in this analysis employ the Lund string hadronisation model as implemented in JETSET 7.4 [44]. A crude option for the simulation of Bose Einstein correlations [45] can be optionally included in the JETSET Monte Carlo. The algorithm does not rigorously model BEC by symmetrising production amplitudes, but treats it as a final state interaction by reshuffling hadron momenta. The model assumes a Gaussian rise of the Bose-Einstein enhancement according to the Goldhaber prescription of equation (5.6). A separate sample of Monte Carlo events was generated and reconstructed in which BEC were included and is referred to as MEAR(BEC). The precise parameters used for the simulation of BEC are given in Appendix B. Unless explicitly stated all Monte Carlo distributions shown are *without* the BEC simulation.

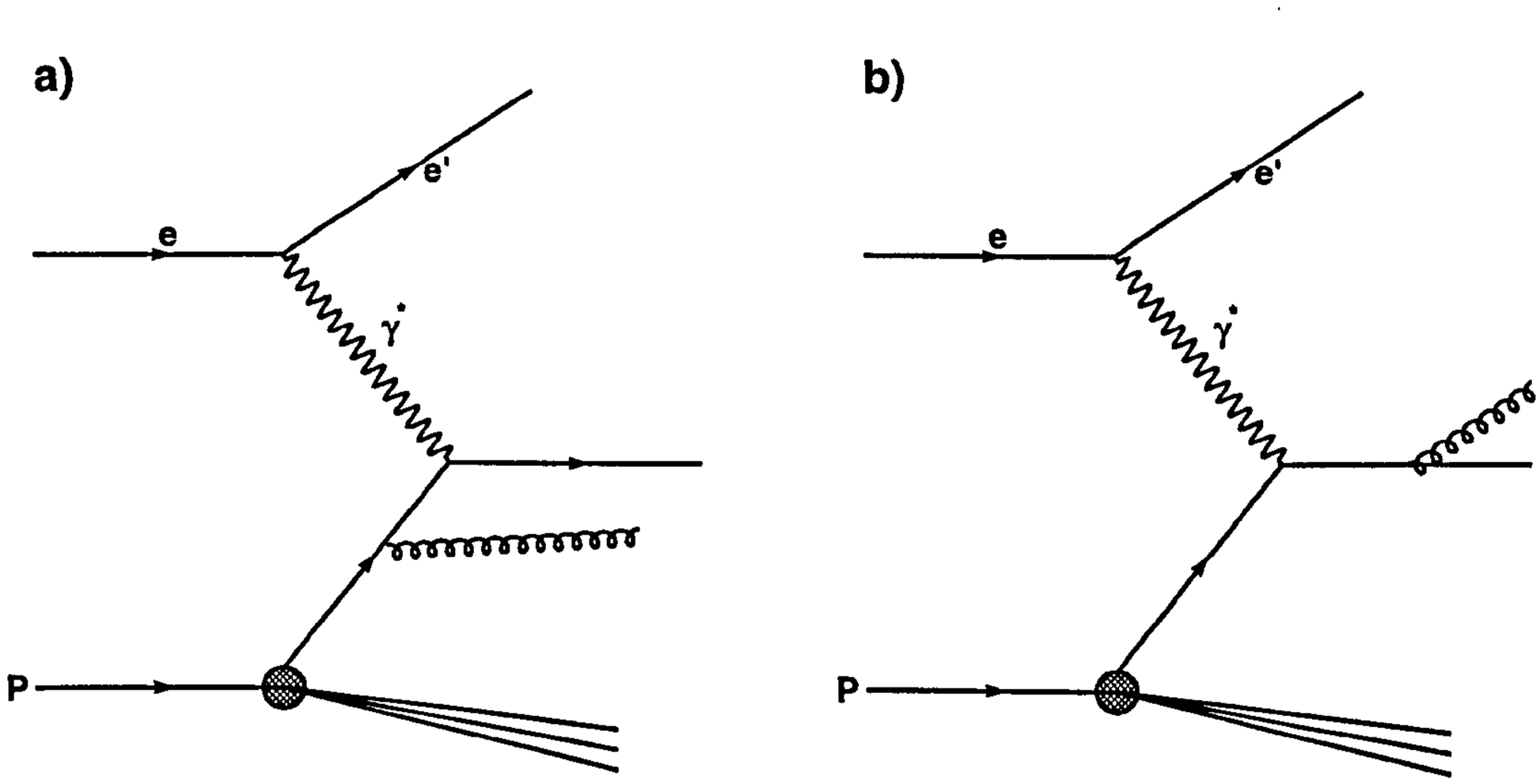

Figure 3.1: The QCD Compton $\mathcal{O}(\alpha_s)$ corrections to the Quark-Parton Model.

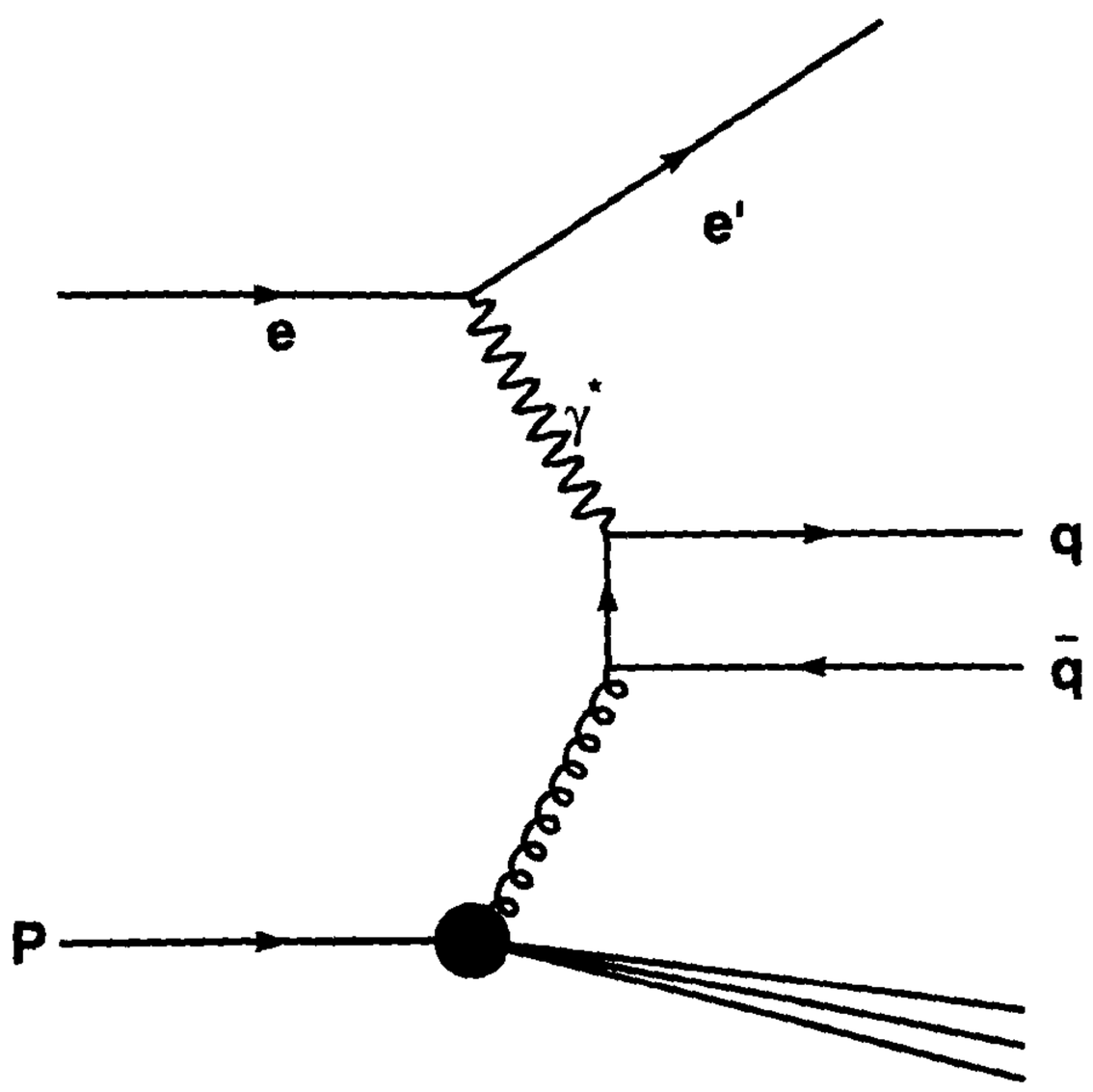

Figure 3.2: The Boson-Gluon Fusion $\mathcal{O}(\alpha_s)$ correction to the Quark-Parton Model.

Chapter 4

Data Selection

The data taken by H1 covers a wide range of physics interests each of which has different signatures in the detector. However, unwanted background events may mimic the signatures of the desired class of physics and need to be studied in order to obtain a pure sample of events. Online, the L1 trigger logic has access to a limited amount of information on which to base a decision as to whether the event is good or not. Later, the L4 trigger has had more time to reconstruct the event allowing a decision to be made based on more detailed information. Nevertheless data succesfully passing the L4 stage is still be contaminated with background from events in which a beam particle collides with a stray gas molecule, or part of the beam pipe itself, or from contamination of an unwanted class of physics events such as photo-production. In order to reduce the amount of contamination selections need to be applied. These are additionally used to limit the data to regions where resolutions are acceptable and the detector simulation is reasonable enough to allow a measurement to be made.

In this chapter the selections applied to the data at all levels from the online acquisition, to the off-line cuts are described. Section 4.1 describes how the data were taken and the trigger conditions used. The offline selections applied to the data are described in section 4.2 and methods of kinematic reconstruction are compared in section 4.3 and 4.4. In section 4.5 Monte Carlo and data are compared at the reconstruction level before any corrections are applied. Track selections are detailed in section 4.6 together with estimates of efficiencies and contaminations obtained from Monte Carlo studies. Finally section 4.7 compares uncorrected single particle spectra with Monte Carlo models.

4.1 Selection of DIS Events

The data in this analysis were taken in 1994 when 820 GeV protons were collided with 27.5 GeV positrons giving $\sqrt{s} = 300$ GeV. Only low Q^2 NC DIS data are analysed in which the scattered positron is detected in the BEMC. The trigger used was a minimum bias trigger requiring a localised energy deposit above 8 GeV, and no veto from the ToF system. The ToF information is used to remove events in which the proton beam interacts with material before reaching H1. In such background events particles from the interaction arrive at the ToF before particles coming back from the nominal interaction vertex. The trigger is fully efficient for electron energies above 10 GeV [47].

4.2 Offline Event Selection

Further selection criteria are applied to the data offline in order to remove remaining background events from beam-gas, and beam-wall interactions as well as unwanted classes of physics events. The following section describes the cuts used which also serve to limit the sample to regions of good acceptance.

- The scattered lepton is required to have an energy weighted cluster radius, ECRA ≤ 4 cm. This cut ensures the BEMC energy deposit is localised as expected from an electromagnetic compared to a hadronic cluster.

- The cluster must be associated with hits in the BPC to ensure that a charged track produces the cluster and to obtain good resolution in θ. The radial separation between the cluster centre of gravity and the BPC track when extrapolated into the plane of the BEMC, R_{bpc}, is required to satisfy $R_{bpc} \leq$ 3.5 cm.

- A geometric cut is applied to remove events where the electron is detected in the less efficient inner region of the BEMC.

- The polar angle of the electron must also satisfy $157° \leq \theta_e \leq 172.5°$. This ensures full containment of the electron cluster within the BEMC.

- With the above selection the largest remaining background source is from γp interactions in which the electron is unseen in the e-tagger and a π^0 de-

cays to $\gamma\gamma$, and one of the photons converts to an e^+e^- pair one of which enters the BEMC faking the signal of a scattered DIS lepton. The energy spectrum of such clusters peaks at low energy and is very different from the prominent kinematic peak expected from genuine DIS events. Therefore the cluster energy is required to satisfy $E'_e \geq 12$ GeV.

The BEMC energy and BPC hits associated with the cluster, combined with an accurate determination of the position of the primary event vertex from tracks in the CJC, mean that the electron polar angle, θ_e, can be determined to within 1 mrad.

The energy cut described above is similar to demanding $y \leq 0.6$ for small x, and thus also removes a kinematic region where the effects of QED radiation are large [49]. These effects are also significant at very low y and are problematic[1] in that initial state QED radiation[2] from the incoming electron effectively lowers the beam energy E_e and the radiated photon is undetected as it escapes down the beam pipe. Thus events suffering initial state radiation have artificially large reconstructed values of y as can be seen from equation 4.1. To remove these events a requirement is placed demanding $W^2 \geq 4400$ GeV^2 as calculated from both the electron and from the hadronic final state. The effects of final state QED radiation from the scattered lepton do not lead to such problems since the radiated photon is generally collinear with the lepton. The spatial resolution of the BEMC is not fine enough to distinguish the electron from the photon and thus the energy is summed in the whole cluster and is therefore accounted for.

In order to compare diffractive with non-diffractive DIS, the data are divided into two sub-samples. Non-diffractive events are required to have the total energy deposit in the region $4.4° \leq \theta \leq 15°$ to be greater than 0.5 GeV. This ensures that evidence for the proton remnant is seen and that there is no large rapidity gap in the forward region.

Diffractive events should conversely have no forward energy, i.e. less than 0.5 GeV in the same region. The following selections are additionally applied:

---

[1] Such events with suitably tagged photons have been used to measure F_2 at very low Q^2 [53], and have also been proposed as a means of measuring the photo-absorption ratio R [54, 55]

[2] In strict quantum mechanical terms the radiated photon cannot be said to 'belong' to either the initial or final state electron. Nevertheless, the concept is useful in the small emission angle approximation.

- The rapidity of the most forward significant energy deposit above noise levels (400 MeV), η_{max}, should be smaller than 3.0 units.

- There should be less than two hit pairs in the forward muon chambers. This requirement can be used to discriminate proton dissociating states since the proton remnant will interact with material in the beam pipe and produce secondary hadronic particles which are detected in the forward muon chambers [48].

- The total energy deposit in the plug is required to be below 3 GeV.

- To ensure that diffractive events are dominated by pomeron exchange and to restrict the data to a region of good acceptance for the dissociating $\gamma^* I\!P$ system, a requirement is placed on $x_{I\!P}$ such that $x_{I\!P} \leq 0.05$. At larger values of $x_{I\!P}$ meson exchanges are known to be increasingly significant [35]. This requirement is an effective cut on M_Y, the forward going mass, and corresponds to a mass of less than 1.6 GeV.

After all selections the diffractive and non-diffractive low Q^2 NC DIS samples contain $\sim 48\,000$ and $\sim 2\,500$ events respectively. The rates of beam-induced background were obtained from electron and proton pilot bunch data and are found to be less than 0.1%, and the photo-production background, estimated from MC, is less than 1% with this selection. The contamination of non-diffractive events in the diffractive data-sample is at the percent level [35]. The phase space region occupied by the data can be seen in the x-Q^2 plane of figure 4.1

The kinematic quantities are determined throughout this analysis using the measurements of E'_e, and θ_e of the scattered lepton - known as the electron method. A comparison with other reconstruction methods is presented in section 4.3. Section 4.5 shows a comparison of event quantities after selection between data and reconstructed Monte Carlo.

4.3 Kinematic Reconstruction Methods

The kinematics of NC DIS events may be reconstructed in one of several ways since the system is over-constrained. The incident beam energies are known and only

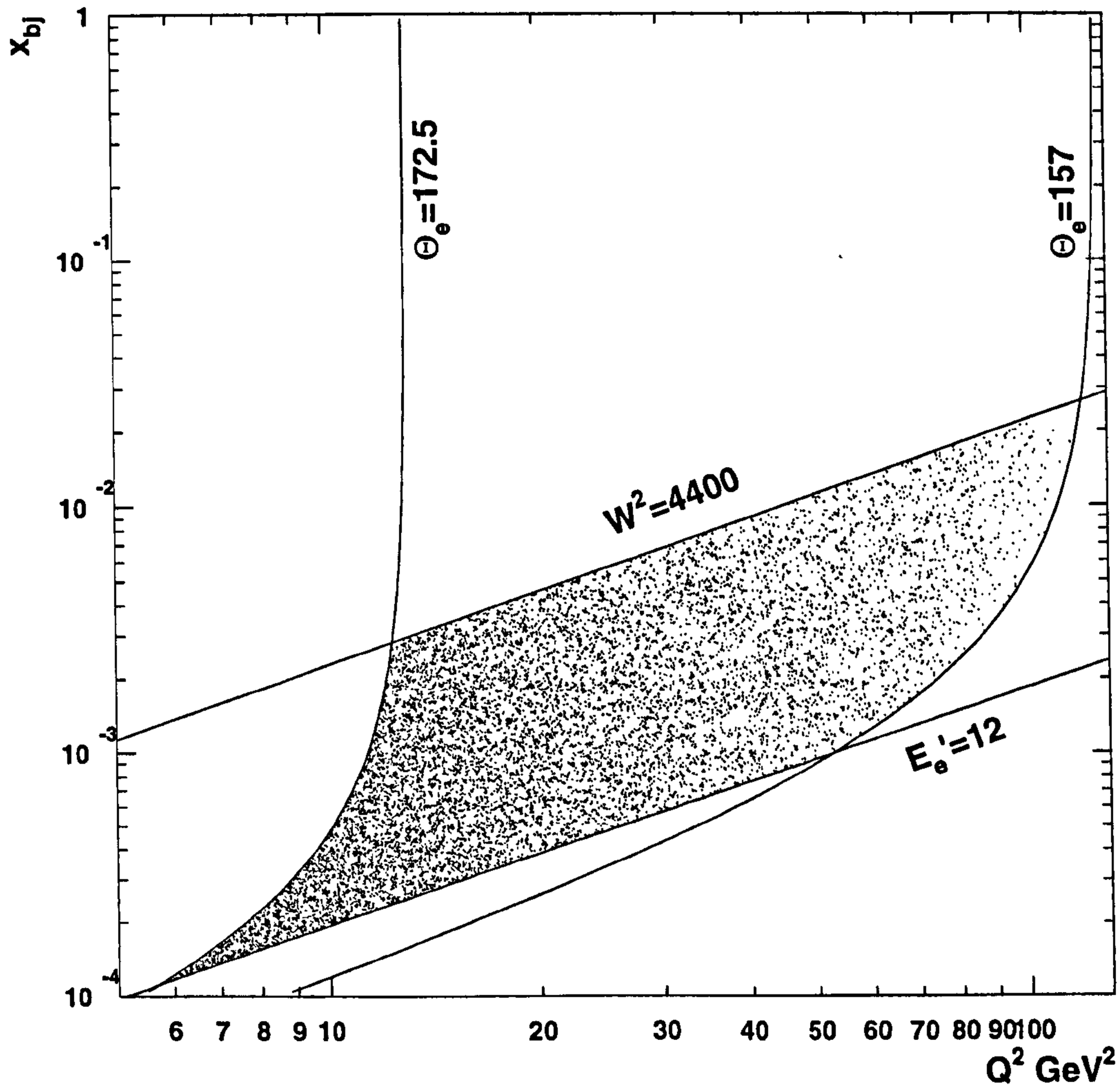

Figure 4.1: Data used in this analysis after all event selection cuts.

two further quantities are needed to describe DIS events in terms of the angle and energy of the scattered lepton, and of the current jet. Three methods are discussed in this section known as the electron, Jaquet-Blondel, and Sigma methods. The first requires only good knowledge of the scattered lepton energy and polar angle. The second relies on a measurement of the hadronic final state, whilst the Sigma method combines the two and is less sensitive to QED radiation. Other reconstruction methods such as the double angle and mixed methods [57] were not considered. Traditionally the electron method was used in fixed target experiments for NC DIS processes, and the Jaquet-Blondel method for CC DIS where there is no detected final state lepton. The following sections briefly discuss each method in turn, and a comparison is made in section 4.4.

4.3.1 Electron Method

The electron method is known to provide an accurate resolution in Q^2 [59]. The method uses measurements of the scattered lepton energy and angle and in principle these are well measured given an easily identified electron. The equations relating measured and kinematic quantities are given below.

$$y_e = 1 - \frac{E'_e}{2E_e}(1 - \cos\theta_e) \tag{4.1}$$

$$Q^2_e = 2E_e E'_e(1 + \cos\theta_e) \tag{4.2}$$

$$x_e = \frac{Q^2_e}{sy_e} \tag{4.3}$$

By taking derivatives the resolutions can be obtained[3]:

$$\frac{dQ^2_e}{Q^2_e} = \frac{dE'_e}{E'_e} \oplus \tan\frac{\theta_e}{2} d\theta_e \tag{4.4}$$

$$\frac{dx_e}{x_e} = \frac{1}{y_e}\frac{dE'_e}{E'_e} \oplus x_e(\frac{E_p}{E_e} - 1)\tan\frac{\theta_e}{2} d\theta_e \tag{4.5}$$

From this it can be seen that the energy resolution limits the accuracy of the Q^2 determination since the angular resolution is better than 1 mrad and the analysis is limited to the range $\theta_e \leq 172.5°$. Equation 4.5 also shows that the x_e resolution degrades as $1/y_e$ thus making the electron method unsuitable for the region below $y \sim 0.1$ The explicit use of the electron beam energy means that this method is sensitive to initial state QED radiation which is known to be large at large and small y [49].

4.3.2 Jaquet-Blondel Method

Measurement of the current jet energy and angle neccesitates use of jet finding algorithms which are difficult to implement, being heavily dependent on the particular

[3]The quantity $a \oplus b$ is defined to be a sum in quadrature, i.e. $\sqrt{a^2 + b^2}$.

algorithm used and on particle losses. However, by imposing energy-momentum conservation one can obtain a better method of reconstruction as shown in the equations below where all sums run over all the observed particles of the hadronic final state, and p_x, and p_y are projections of the particle momentum on the x and y co-ordinate axes. This method was first proposed in [56].

$$y_{jb} = \frac{\sum_i E_i - p_{zi}}{2E_e} \tag{4.6}$$

$$Q^2_{jb} = \frac{(\sum_i p_{xi})^2 + (\sum_i p_{yi})^2}{1 - y_{jb}} \tag{4.7}$$

$$x_{jb} = \frac{Q^2_{jb}}{s y_{jb}} \tag{4.8}$$

Inspection of equation 4.6 shows that with this method y reconstruction is insensitive to the (common) losses of forward going hadrons which contribute very little to the numerator, whereas (rare) hadrons traveling along the negative z axis will introduce a maximal error and shift y_{jb} to lower values.

4.3.3 Sigma Method

The Sigma method is able to reconstruct DIS kinematics independent of initial state QED radiation by reconstructing the incident electron beam energy at the hard interaction vertex, and was first proposed in [50, 51]. The formulæfor kinematic quantities are given below.

$$y_\Sigma = \frac{\Sigma}{\Sigma + E'_e(1 - \cos\theta_e)} \tag{4.9}$$

$$Q^2_\Sigma = \frac{E'^2_e \sin^2\theta_e}{1 - y_\Sigma} \tag{4.10}$$

$$x_\Sigma = \frac{Q^2_\Sigma}{s y_\Sigma} \tag{4.11}$$

where $\Sigma = \sum_i E_i - p_{zi}$ and runs over all particles of the hadronic final state. Equation 4.9 gives y at the vertex of the hard sub-process since the denominator term

arises from a consideration of longitudinal energy-momentum conservation. Also at large y the Σ term dominates over the $E'_e(1-\cos\theta_e)$ term, thus errors in the measurement of Σ tend to cancel in both numerator and denominator. The quantity Q^2_Σ is also independent of initial state QED radiation since an emitted photon is generally collinear with the incoming beam electron and carries little transverse momentum.

4.4 Comparison of Methods

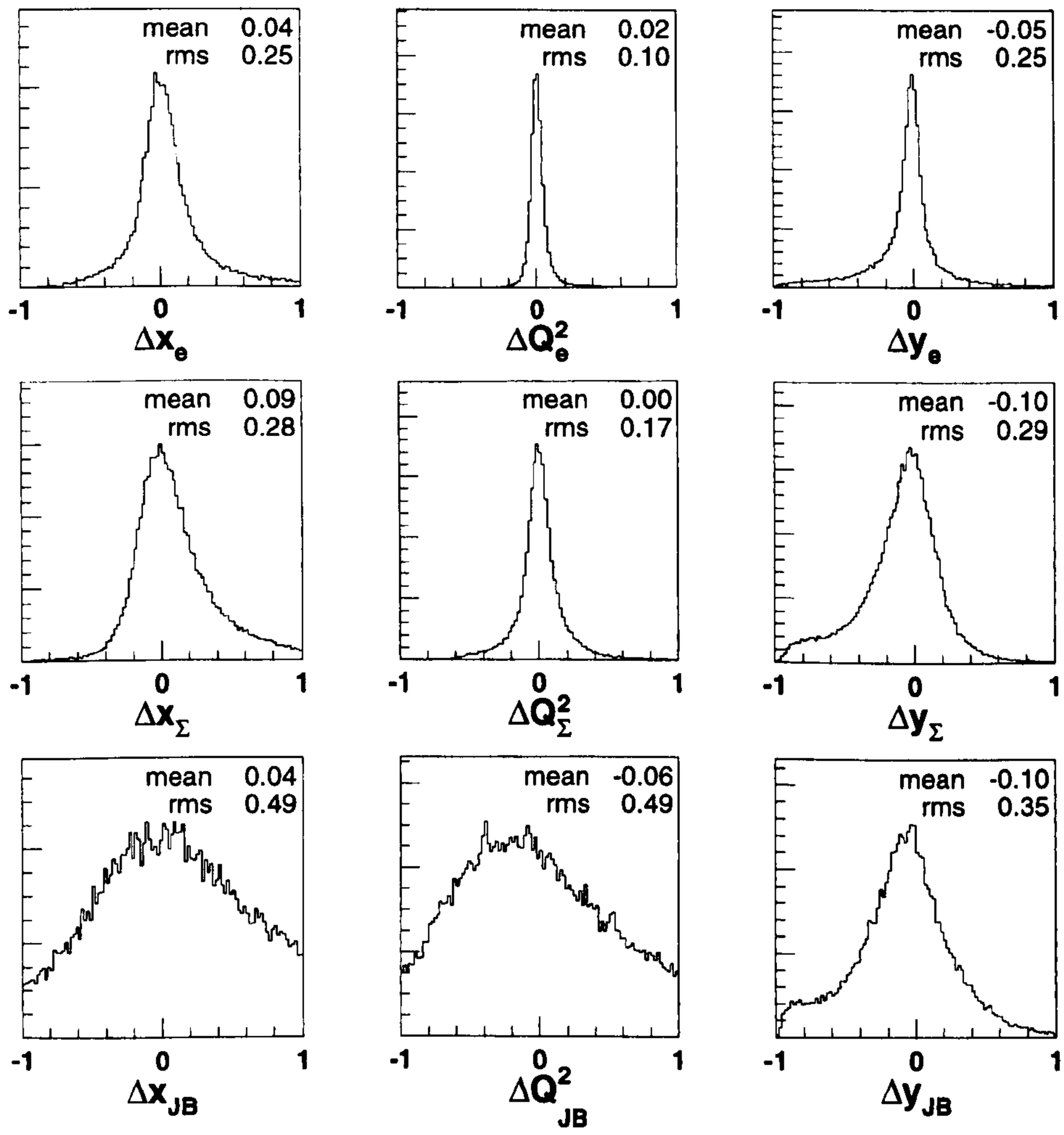

Figure 4.2: Resolutions of the kinematic quantities x, Q^2, and y as calculated using the electron, Sigma, and Jaquet-Blondel methods. An arbitrary scale is used on the y axis.

Figure 4.2 shows the resolutions obtained using each of the three methods within the acceptance region of the analysis. A radiative Monte Carlo (DJANGO) was

used to model for QED radiative effects. The resolution is defined to be

$$\Delta f = \frac{f_{tru} - f_{rec}}{f_{tru}}$$

where f represents a kinematic quantity, the subscript tru refers to the true generated value, and the subscript rec refers to the reconstructed value.

It can be seen that the Jaquet-Blondel fails to provide a competitive measurement of the kinematics, however the Sigma and electron methods are quite acceptable. All three methods have a positive bias on y reconstruction which is ~ 0.1 for the Sigma method arising from losses in the backward beam pipe. The electron method bias is from events with initial state QED radiation which migrates events to larger y. Resolution in Q_e^2 is very good at 10% with a bias of 2%, whilst the Jaquet-Blondel method provides a very bad measurement due to losses in the forward beam pipe which affect the numerator of equation 4.7, as well as backward losses affecting the y_{jb} measurement at large y. Similar x resolution is obtained for the Sigma and electron methods, though the electron method has a smaller bias. Both are affected by QED radiation from the use of s in equations 4.3, and 4.11.

It should be noted that the resolutions obtained are averaged over the whole kinematic region under consideration. The accuracy of x, Q^2, and y determination for each method does vary over the phase space and in some regions, for example at low y, the Jaquet-Blondel method achieves much better results. For further details see [57,58]

4.5 Comparison of Kinematics Between Data And Monte Carlo

In figures 4.3 and 4.4 the uncorrected data are compared to the reconstructed Monte Carlo predictions for diffractive and non-diffractive data. All spectra are normalised to the accepted number of events. The kinematic quantities shown are obtained using the electron method as described in section 4.3. Good agreement is observed between the data and Monte Carlo. Also shown are the parameters of the reconstructed electron: θ_e, ϕ_e, and E'_e.

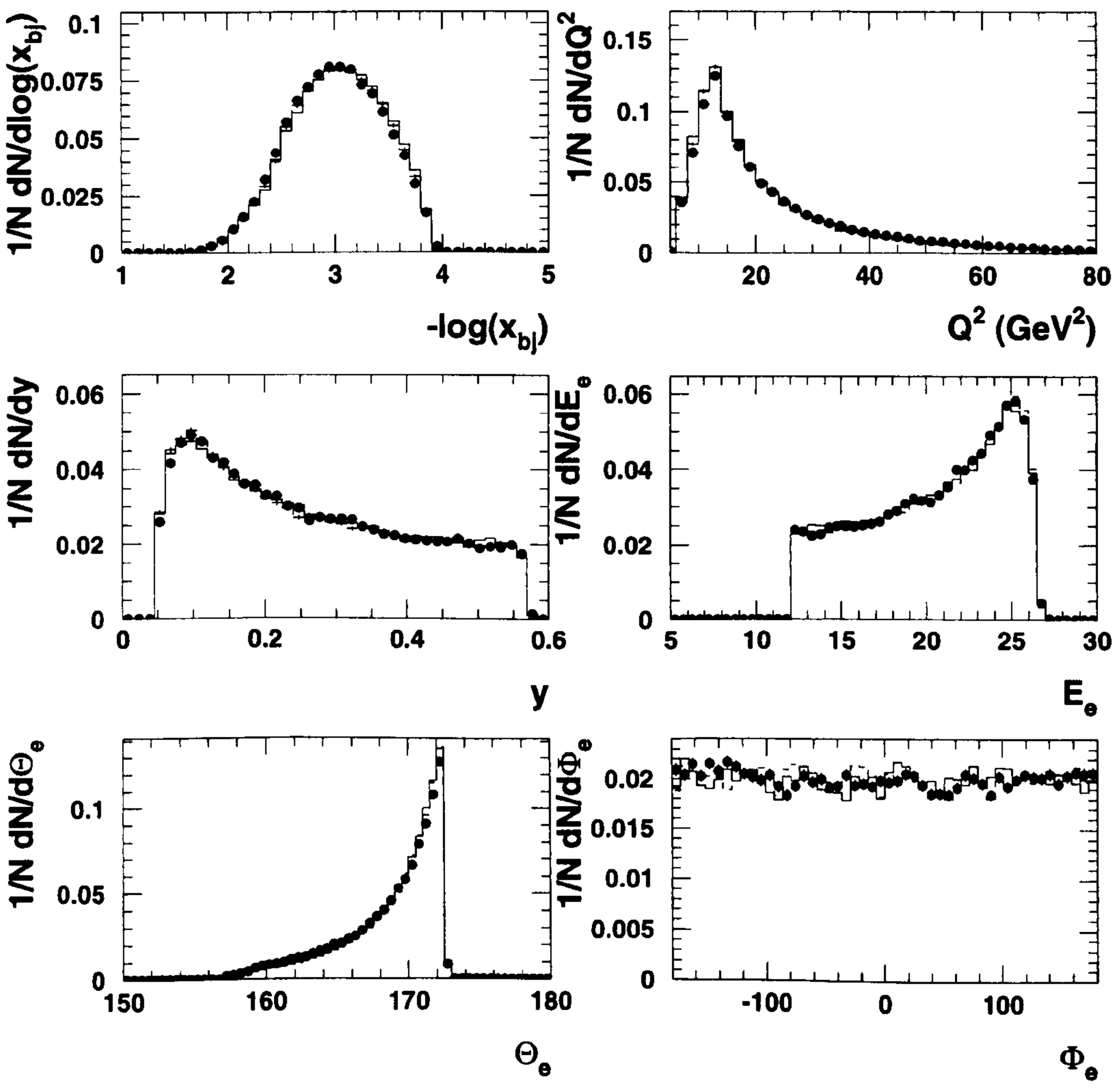

Figure 4.3: Control plots for non-diffractive low Q^2 data (full circles) compared to the MEAR (full line), and MEPS (dashed line) models

The event distributions for the diffractive data sample are shown in figure 4.4. The DIS kinematic quantities x, y, and Q^2 show acceptable agreement between data and Monte Carlo though this is by no means perfect, particularly in the y spectrum and the region $Q^2 < 10$ GeV^2. This is attributed to an imperfect description of the pomeron structure function used in the Monte Carlo models. It is expected that this analysis is insensitive to the details of the structure function, however this assumption is tested in section 5.13. More relevant variables to describe diffractive DIS are M_X ,$x_{I\!P}$, and η_{max}, where the Monte Carlo description is much better.

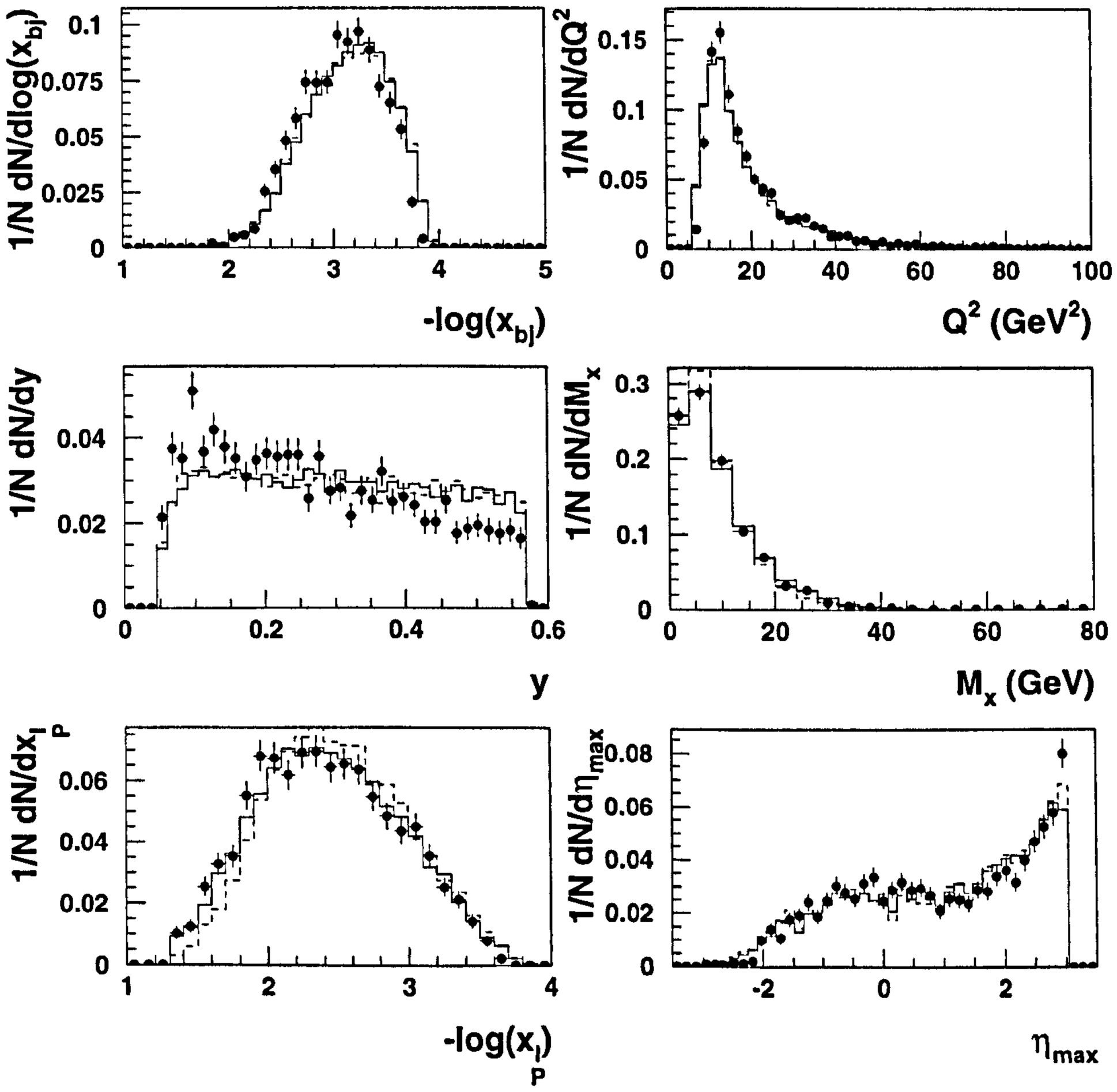

Figure 4.4: Comparison of event observables for diffractive data (full circles) with RAPA (full line), and RAPP (dashed line).

4.6 Track Selection

An analysis of particle correlations is very sensitive to detector related problems such as the splitting of one track into two parts and the imperfect modeling of interactions of the particles with the material of the detector. Physics effects which are not well generated such as resonance production rates could also be significant. These problems affect correlation analyses much more than analyses of single particle inclusive spectra since, although the rates may be small, the particles produced are strongly correlated and usually are confined to small regions of phase space. Therefore a high quality track selection is required. The cuts used are as follows:

- Charged tracks are required to be associated to the primary event vertex in order to minimize decay products from weakly decaying particles, for example the K_s^0 and the Λ^0.

- Requiring a transverse momentum $p_t > 0.15$ GeV rejects strongly curving tracks within the central tracking chambers. These tracks are difficult to reconstruct and are often split into several parts, as they lose energy so rapidly.

- A polar angle satisfying $22° < \theta < 150°$ restricts the analysis to hadrons which can be measured in both jet chambers but which does not require use of the forward tracker. The upper restriction on θ also rejects the scattered lepton track from the analysis of low Q^2 data.

- The total number of CJC hits for each track is required to be greater than or equal to 10. This is a good measure of track quality since more hits allow a better determination of the curvature and hence the transverse momentum of the track.

- Finally a restriction is made demanding that all tracks start in the inner jet chamber. This is a powerful means of rejecting split tracks.

The requirements on p_t, and θ are referred to as acceptance cuts, whilst requirements on radial track length, and track start are referred to as quality cuts. In this analysis all charged particles are assumed to be pions which constitute ~85% of all accepted charged particles as determined from Monte Carlo.

4.6.1 CJC Efficiency Studies

A Monte Carlo study of the CJC efficiency and estimates of contamination are shown in figure 4.5. The study was performed by attempting to associate each MC track at the reconstructed level with a generated track by comparing numbers of simulated hits with the number of hits used to reconstruct the track. A reconstructed track is linked to the generated track with which it shares the largest ratio of reconstructed to simulated hits. An indication of the sensitivity of the method is obtained by examining the distribution of the ratio which shows that 95% of all linked tracks have a hits ratio above 50% and is strongly peaked near 100%. Use of this procedure required an accurate simulation of the central tracking system and included a

description of inefficient wires in a "sick wire map". After the linking process, tracks were classified as follows:

- linked - successfully linked reconstructed and generated tracks.
- ghosts/split - reconstructed tracks with no generated partner arising from mirror or noise hits (ghosts), or split tracks which arise from the passage of one particle being reconstructed as two separate tracks.
- lost - generated tracks which were not reconstructed.

The first two classifications above are further subdivided into *accepted* and *rejected* categories which identify tracks as being accepted or rejected after application of all track selection criteria given in section 4.6 above. The track finding efficiency, ϵ, is then defined as:

$$\epsilon = \frac{n_{link}^{acc}}{n_{link}^{acc} + n_{link}^{rej} + n_{lost}}$$

and the rate of split/ghost tracks, β, as

$$\beta = \frac{n_{split}}{n_{link}^{acc} + n_{split}}$$

where n is the number of tracks in each category labelled by the superscripts and subscripts.

Figure 4.5 shows the efficiency and the split track rate as a function of p_t, and θ before and after application of quality cuts. The efficiency is found to fall dramatically for $p_t < 0.15$ GeV, but is quite stable at larger p_t with an efficiency of 95%. The sharp drop in ϵ at $\theta \sim 20°$, and 160° marks the edge of the CJC acceptance. The quality cuts have a minor effect on the efficiency, reducing it by ~1%.

The rate of split tracks shows a large peak for $p_t < 0.15$ GeV at 17% indicating problems of the reconstruction program in linking track segments from strongly curving tracks which often curl back towards the beam pipe. The rate is relatively stable at 2% in θ, falling off close to the edges of the CJC. The quality cuts have a large

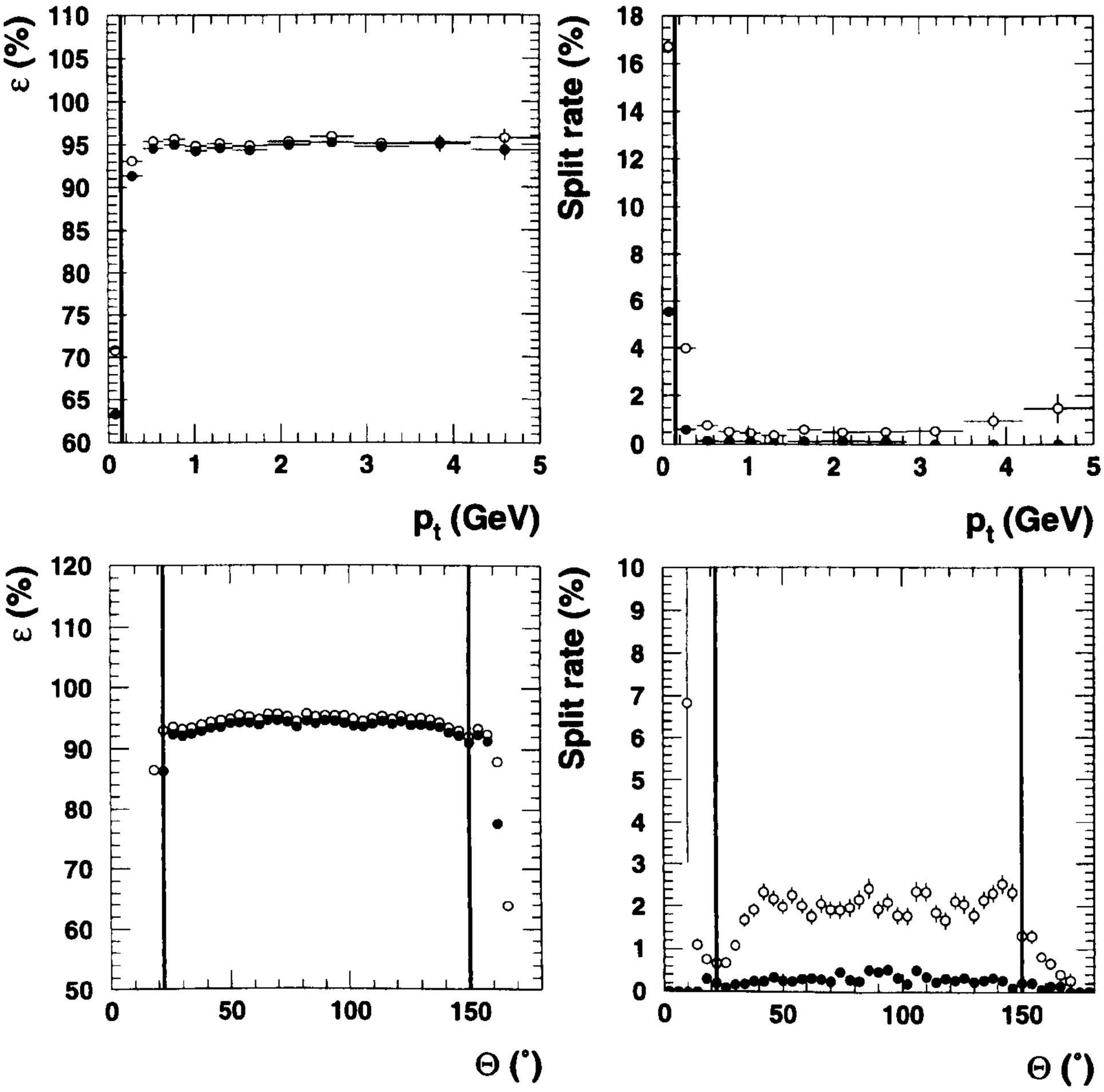

Figure 4.5: Efficiency and split track rate in the CJC before (open circles) and after (full circles) quality cuts. The solid lines show location of cuts in p_t and θ.

affect on the number of split tracks, reducing it to a stable 0.3% in θ.

No difference between the reconstruction efficiency of positively and negatively charged tracks is observed within the acceptance region given by the cuts in p_t and θ. However, in the range $p_t < 0.15$ GeV positive particles are found to have a reconstruction efficiency below that of negatively charge particles. This is a result of the construction of the jet chamber [52]. Also an unsimulated misalignment between the inner and outer chambers could result in a further difference in the reconstruction efficiencies of positive and negatively charged tracks. The effect of misalignment can be seen in figure 4.6 where the ratio of p_t spectra for positive and negative tracks in the data is compared to reconstructed MC before and after

application of a correction for the effect. The correction is not perfect and residual effects remain at the level of 30% at p_t=4.5 GeV, though the Monte Carlo also predicts a slight rise of the ratio and is roughly 15%. It should be noted that the p_t distribution of tracks is very soft (see figure 4.10c) and 99.5% of all tracks have a p_t below 4 GeV. Nevertheless, the impact of this is treated as a systematic error and is discussed further in section 5.13.

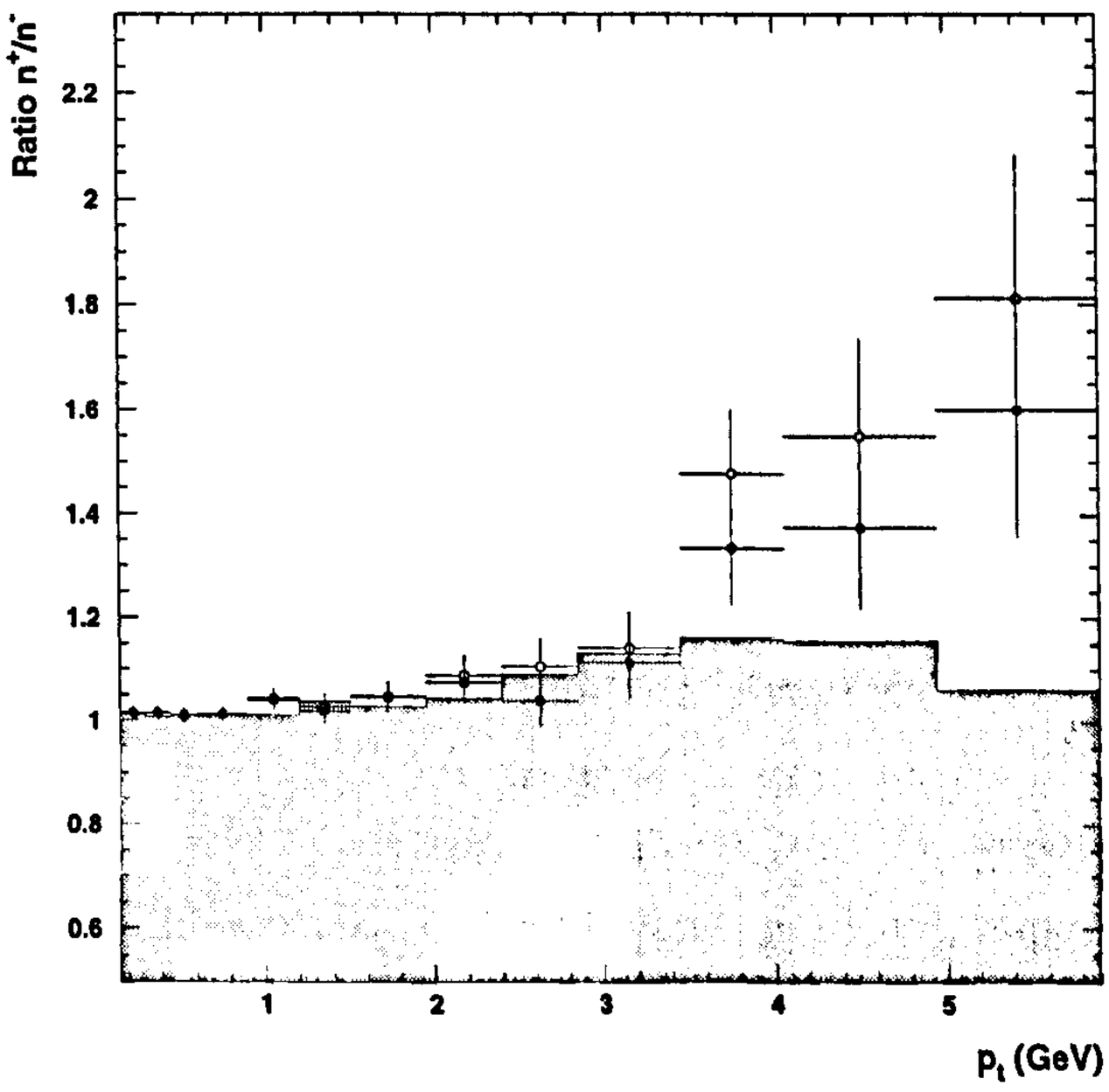

Figure 4.6: Ratio of the number of positive to negative tracks as a function of p_t, before (open circles) and after (closed circles) a correction is applied to the data, compared to reconstructed Monte Carlo (shaded histogram).

4.6.2 Split Track Pairs

BEC studies are very sensitive to double counting effects i.e. the splitting of a single track into two like-sign pieces. For split tracks one finds $M_{inv} \cong 2\ m_\pi$, and such pairs contribute to the interesting region where BEC are significant. A typical split pair is shown in fig 4.7. A large peak in the invariant mass distribution of like-sign pairs at the two pion mass threshold can indicate such split tracks as shown in fig 4.8.

There are three circumstances through which a split track pair may arise, either due to reconstruction inefficiencies, wire inefficiencies, or misalignments between the

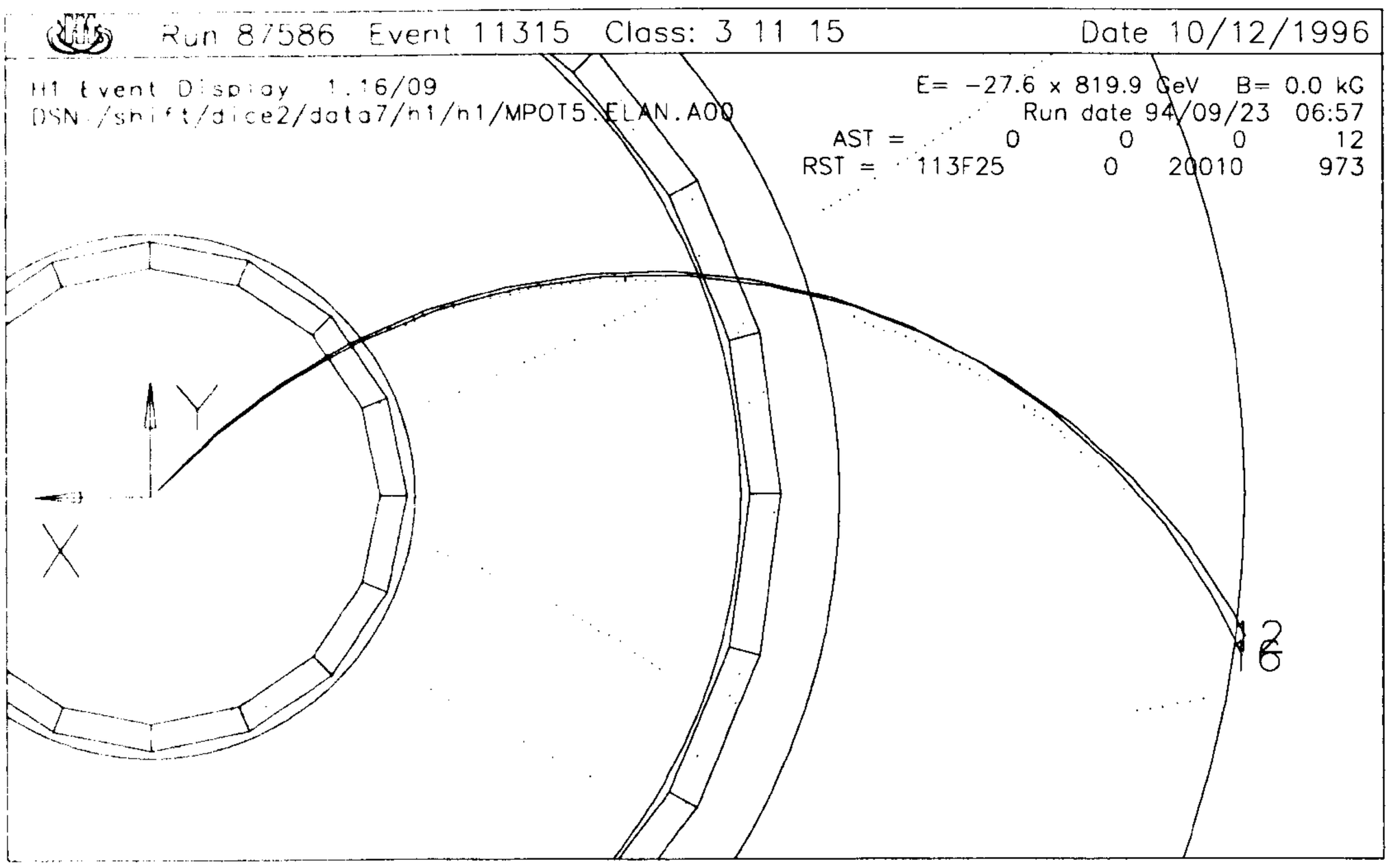

Figure 4.7: A low Q^2 event showing a close up of the central tracker in the $r-\phi$ plane . Clearly visible is a negatively charged split pair in which hits from CJC1 and CJC2 are associated to different tracks. All other tracks have been suppressed.

tracking chambers. In the first case a particle traversing the inner chamber leaves wire hits, but upon reaching the end of the CJC1 can undergo multiple scattering in the dead material between the two chambers. When the track enters CJC2, its momentum is altered and the reconstruction program may find it difficult to associate hits from the two chambers to the same particle. Two tracks are reconstructed very close to one another, and therefore have a very small invariant mass. A description of inefficient wires of the chambers was included in the detector simulation. These regions give rise to a large rate of split tracks and the effect is shown for MC simulation in figure 4.9 as a function of ϕ. The open circles show the rate after application of acceptance cuts in p_t, and θ only. The full circles show the rate after applying the extra quality selection on radial track length and start point of the track. The quality selection removes 85% of the split tracks leaving a remaining rate which is smooth in ϕ and is at the level of 0.3%. The peak structure arises from inefficient cells of CJC1 as simulated by the sick wire map.

MC simulations generally give a more optimistic description of the detector response than is actually the case. It is therefore important to cross check MC results with

estimates obtained directly from the data. This was achieved by scanning a number of events by eye and gave an estimated remaining rate of split tracks of $0.2 \pm 0.1\%$ and an efficiency of $95 \pm 2\%$. Also the scan found no tracks formed from noise hits or mirror hits of real tracks. A finite resolution in track pairs would be seen as an opposing effect to that of split track pairs and would cause two separate particles traversing the detector to be reconstructed as one. A scan of events showed no cases where two sets of hits within the tracker gave rise to only one track.

4.7 Comparison of Particle Spectra

In figure 4.10 the event normalised track spectra are shown separately for diffractive and non-diffractive data compared to the two MC models used with each sample. Since the spectra are event normalised, any absolute shifts of the data with respect to the MC are due to differences in the mean multiplicity. The MEPS MC overestimates particle production in the forward region whilst MEAR underestimates the data. This corresponds to the target fragmentation region where our knowledge is not so good. The ϕ distribution is smooth and flat indicating no holes or serious problems with the CJC acceptance. The p_t spectrum of charged tracks is well described by MEAR, and MEPS exhibits a softer spectrum. As expected the forward peak of the θ distribution in non-diffractive data is much reduced in the diffractive sample since the event selection requires no forward activity. RAPA follows the data well, even to the extent of describing the multiplicity. RAPP, however underestimates the forward region.

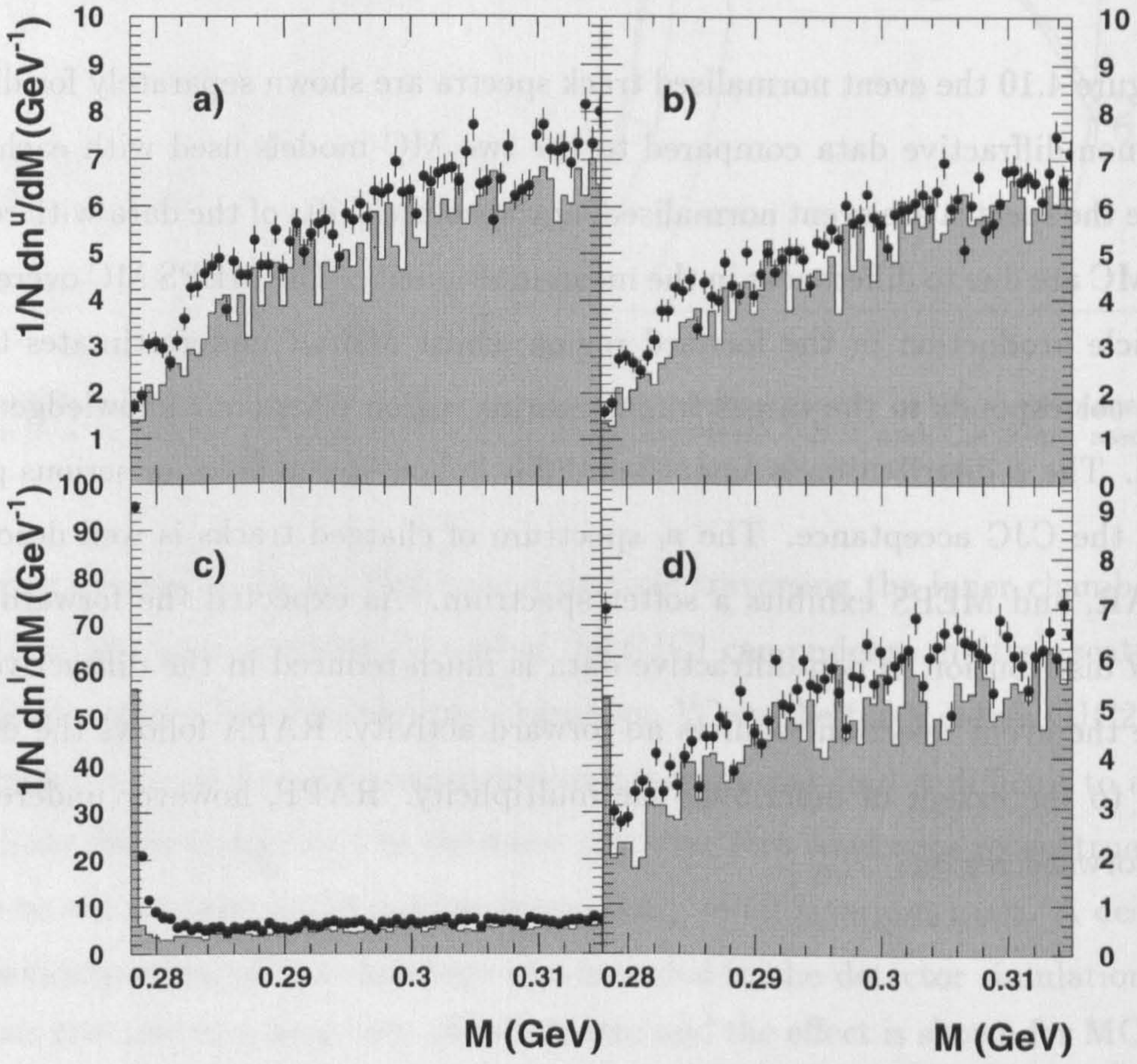

Figure 4.8: The uncorrected event normalised invariant mass spectra for all track pairs showing the effect of the quality selection on the split track rate for data (full circles), and reconstructed MEAR(BEC) MC (histogram). a) Shows the unlike-sign mass spectrum before and (b) after the quality track selection is applied, c) like-sign mass spectrum before and (d) after track selection. The split tracks are clearly visible as the peak at threshold in (c). Note the different scales used.

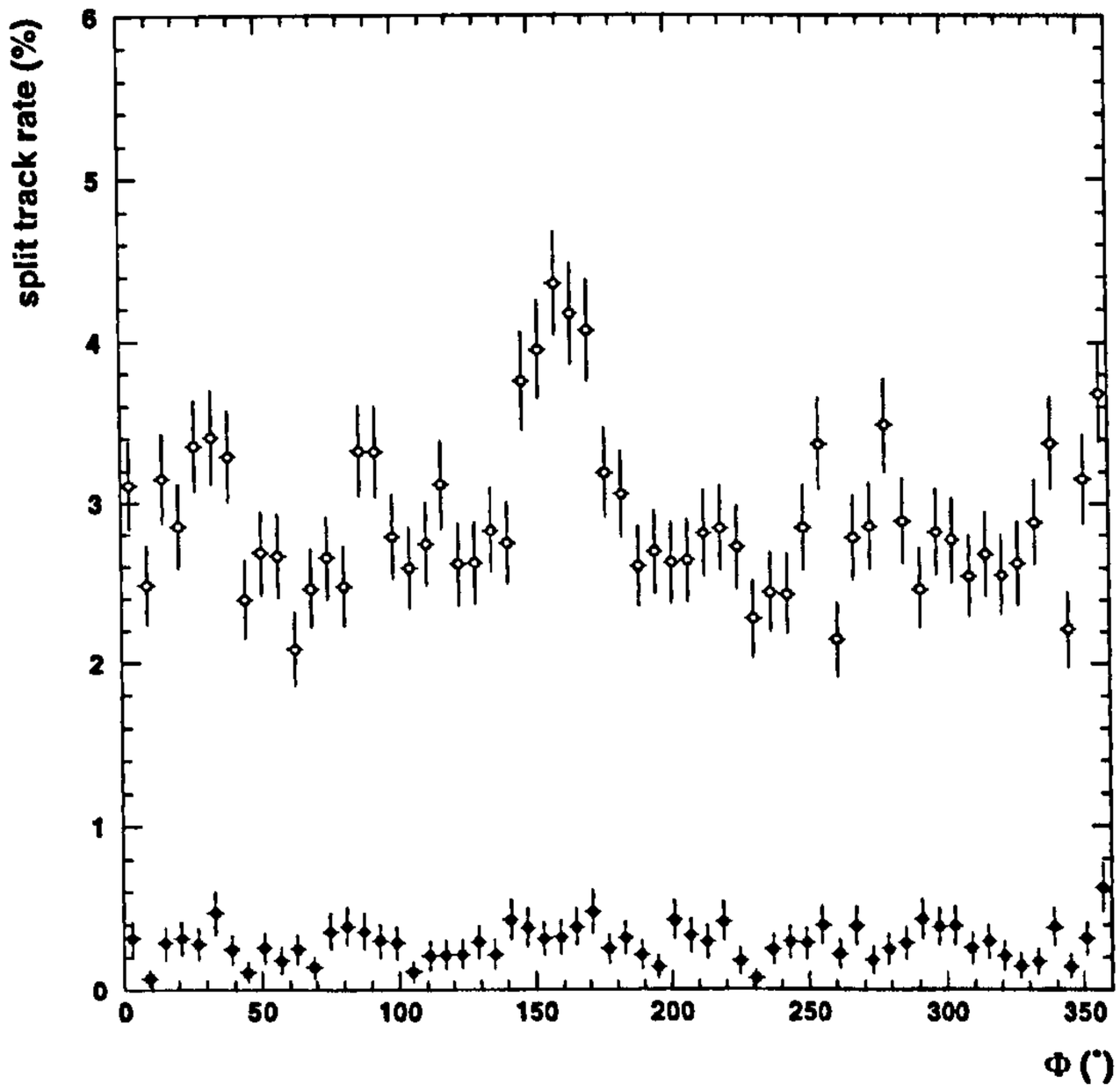

Figure 4.9: MC simulation of the rate of accepted split tracks as a function of ϕ before (open circles), and after (full circles) application of acceptance and quality cuts.

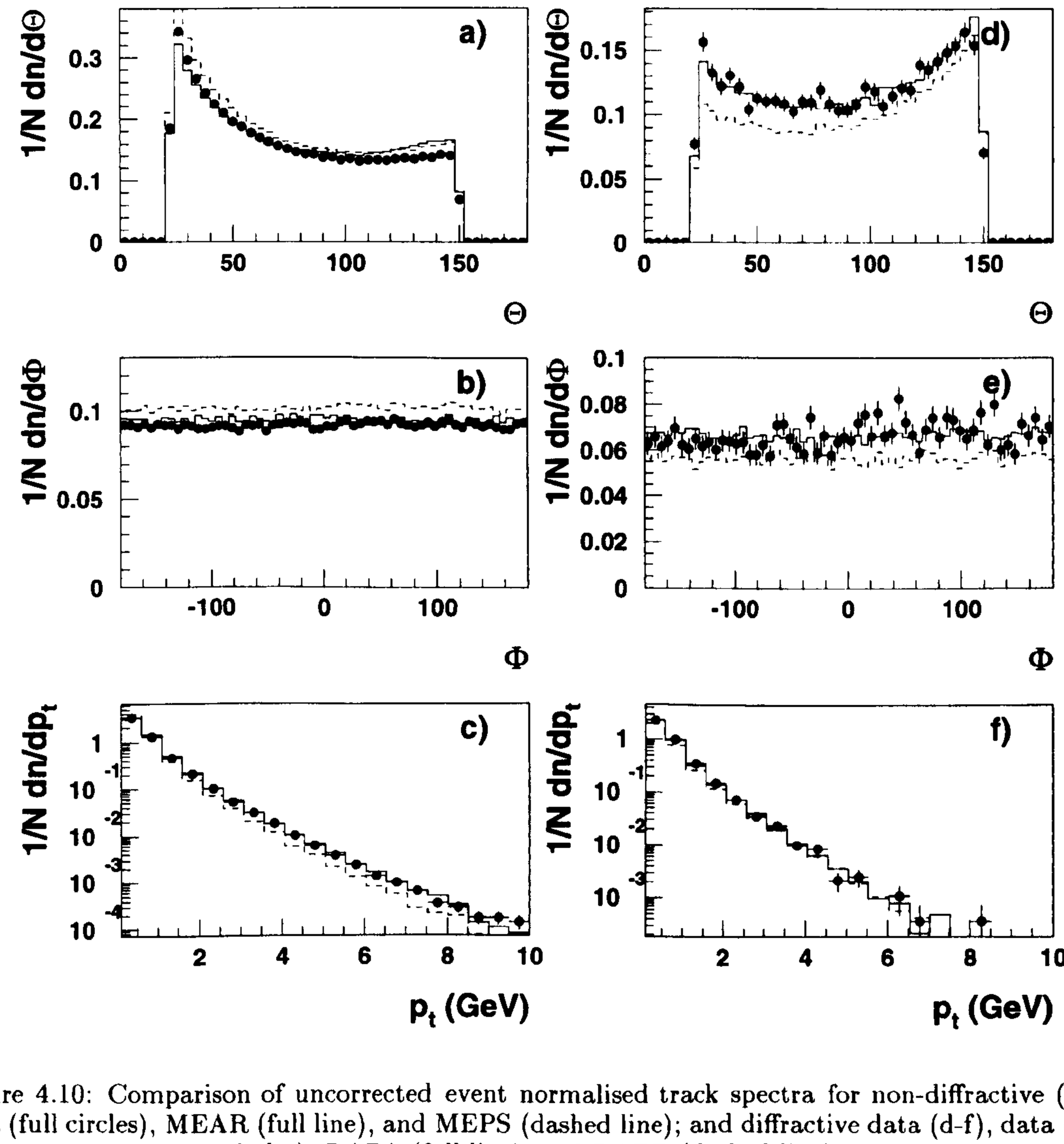

Figure 4.10: Comparison of uncorrected event normalised track spectra for non-diffractive (a-c) data (full circles), MEAR (full line), and MEPS (dashed line); and diffractive data (d-f), data (full circles), RAPA (full line), and RAPP (dashed line)

Chapter 5

Bose-Einstein Correlations

5.1 Bose-Einstein Interferometry

The use of Bose-Einstein correlations (BEC) as an interference measurement was first proposed by Hanbury-Brown, and Twiss [60] in 1954 where the effect was used to measure the angular diameter of stellar bodies. Since then the same effect has been analysed in high energy physics in order to gain information about the space-time distribution of the source from which bosons are emitted. This is of considerable importance since the least understood sector of QCD is the phase of hadronisation when partons below some energy scale (Λ_{QCD}) can no longer be described in the framework of perturbative QCD due to the large value of α_s, the strong coupling constant. At this point the confinement process begins whereby observable hadrons are formed from some distribution of unobservable partons. This process is manifestly perturbatively uncalculable[1] and so any measurement probing this phase is of interest.

The Bose-Einstein effect is quantum mechanical, based upon the quantum symmetry properties of the wave functions of bosons which, unlike fermions, are able to occupy identical quantum states. Since the two-boson wave function is required to be symmetric upon particle exchange, the production amplitude-squared has an interference term which leads to constructive interference when two bosons with four-momenta p_1 and p_2 are identical and thus an *enhancement* in the probability of finding bosons close together in phase space[2]. The normalised two-particle

[1]It is hoped that although perturbative QCD will not be able to shed light on hadronisation phenomena, calculations of lattice QCD may be able to help once techniques have become more refined.

[2]Similar arguments applied to a two-fermion wave function would result in a suppression of the two-fermion correlation function.

correlation function, $R(p_1, p_2)$, is defined as

$$R(p_1, p_2) = \frac{\frac{1}{\sigma}\frac{d^2\sigma}{dp_1 dp_2}}{\frac{1}{\sigma}\frac{d\sigma}{dp_1} \cdot \frac{1}{\sigma}\frac{d\sigma}{dp_2}} \tag{5.1}$$

where $\frac{d\sigma}{dp_1}$ and $\frac{d^2\sigma}{dp_1 dp_2}$ are the single and two-particle inclusive densities. The maximal value of this function occurs when $p_1 = p_2$, since the strength of the correlation depends on the degree of overlap between the single particle wave-functions. This "exchange density" is determined by the size of the emitting source. Hence knowledge of the variation of $R(p_1, p_2)$ with momentum difference carries information about the source distribution. Thus analyses of the Bose-Einstein effect generally measure the correlation as a function of the Lorentz scalar momentum separation T, where,

$$T^2 = -(p_1 - p_2)^2 \tag{5.2}$$

and is trivially related to the invariant mass, M, of the hadron pair:

$$T^2 = M^2 - 4m_\pi^2 \tag{5.3}$$

where m_π is the pion mass. Traditionally the source density is described by a distribution $\rho(\xi)$, where ξ here represents a space-time four-vector. Then, the enhancement due to BEC interference is

$$R(T) = R_0(1 + \lambda \mid \tilde{\rho}(T) \mid^2) \tag{5.4}$$

where R_0 is a normalisation constant, $\tilde{\rho}$ is the Fourier transform of $\rho(\xi)$ and λ is a measure of the incoherence of the source: $\lambda = 1$ for complete incoherence and $\lambda = 0$ for complete coherence. A more detailed discussion of coherence may be found in appendix A. Early models assumed a sphere of emitters with a Gaussian density:

$$\rho(\xi) = \rho(0)\exp(-\frac{\xi^2}{2r^2}) \tag{5.5}$$

The length r is interpreted as the radius of the production volume. Such a source results in a correlation known as the Goldhaber parametrisation:

$$R(T) = R_0(1 + \lambda\exp(-r^2T^2)) \ . \tag{5.6}$$

The string model interpretation of BEC offered by Anderson and Hofmann [68], takes into account the relativistic motion of the pion sources with respect to each other in high energy collisions. This may naïvely be expected to produce a source size contracted along the "event axis" due to the Lorentz boost of the partons. However, in the string model particles are ordered in longitudinal momenta such that particles coming from the ends of the string have a higher momentum than those coming from the centre, and since BEC are visible for particles with small momentum differences, then particles separated by large distances will not significantly interfere. Therefore, the length scale measured in BEC analyses is not the size of the overall hadronisation volume, but the distance between production regions for which momentum distributions still overlap, i.e. BEC measure the region in which pion pairs of four-momentum difference T are produced with comparable probability. This model predicts an approximate exponential shape of the correlation function:

$$R(T) = R_0(1 + \lambda \exp(-rT)) \tag{5.7}$$

Furthermore, the model predicts that the size is independent of the centre of mass energy, and of the reaction creating the colour strings.

Recently, considerable effort has been devoted to the study of fluctuation phenomena in multi-particle production processes, both from a theoretical and an experimental point of view [69]. These studies concentrated on the search for intermittency, i.e. the occurrence of large fluctuations in particle density arising from scale invariant dynamics. This behaviour has been suggested by Bialas and Peschanski [61] to arise from the approximate self-similar (i.e. fractal) nature of the QCD parton cascade, or from large event-by-event fluctuations in the source size. They argue that spikes in the particle density of high energy collisions are expected and imply self-similar energy dissipation in ever decreasing regions of phase space, having borrowed ideas from turbulent fluid dynamics. The scaling implies that the correlation functions have a power-law behaviour, i.e. that correlations exist at all scales and the ratio of correlations at scales T_1, and T_2 is dependent only on the ratio T_1/T_2. To test this hypothesis the data are fitted with a power-law of the form:

$$R(M) = A + B\left(\frac{1}{M^2}\right)^{\beta} \tag{5.8}$$

where A, B, and β are the free parameters of the fit. Note that the power-law is expressed in terms of the invariant mass M rather than T. The power-law behaviour of these factorial moments was already observed in [70].

The remainder of this chapter describes the steps followed in order to answer the following questions:

1. Is there any difference in BEC between diffractive and non-diffractive events, i.e. is the hadronisation of the pomeron remnant different to the hadronisation of the "struck quark" system as viewed by BEC?
2. Do BEC vary over the kinematic plane, and which quantity drives the evolution if seen?
3. Are the data able to distinguish between the three parametrisations of BEC?

5.2 Measurement Method

In order to measure the Bose-Einstein enhancement, the two-particle like-sign inclusive density, denoted by $\rho_2^l(T)$, is normalised to a reference sample $\rho^{ref}(T)$ which ideally contains no Bose-Einstein correlations, by forming the ratio:

$$R(T) = \frac{\rho_2^l(T)}{\rho^{ref}(T)} \qquad \rho_2^l(T) \equiv \frac{1}{N}\frac{dn^{\pm\pm}(T)}{dT} \tag{5.9}$$

where N is the total number of events in the sample and $n^{\pm\pm}(T)$ the number of $(++)$ and $(--)$ pairs in the sample. In this analysis either the two particle unlike-sign inclusive distribution is used:

$$\rho^{ref}(T) = \rho_2^u(T) \equiv \frac{1}{N}\frac{dn^{\pm\mp}(T)}{dT} \tag{5.10}$$

or uncorrelated pairs created by mixing tracks from different events, are used denoted by

$$\rho^{ref}(T) = \rho_1 \otimes \rho_1(T) \equiv \frac{dn^{mix}(T)}{dT} \tag{5.11}$$

where $n^{\pm\mp}(T)$ is the number of (+-) pairs in the sample, and n^{mix} is the number of pairs formed from mixed events. The normalisation conditions for the inclusive

densities may be arbitrarily chosen since ratios and double ratios of densities are taken (see below). In this analysis the normalisation conditions are taken such that

$$\int \rho_2^l(T)dT = < n^l > \tag{5.12}$$

$$\int \rho_2^u(T)dT = < n^u > \tag{5.13}$$

$$\int \rho_1 \otimes \rho_1(T)dT = < n^l > \tag{5.14}$$

where $< n^l >$ is the mean number of like-sign pairs per event, and $< n^u >$ the mean number of unlike-sign pairs per event.

The choice of the reference sample is not trivial and a source of bias and systematic errors in all BEC measurements. Ideally it should satisfy the following conditions:

- Absence of BEC since the signal is an enhancement above all other statistical and dynamical correlations.
- Presence of correlations due to the topology and the global properties of the events. These kinematic effects are present in ρ_2^u, but not in $\rho_1 \otimes \rho_1$ since mixed events do not conserve energy-momentum.
- Absence of dynamical correlations not present in like-sign pairs, the clearest example of which is the effect of decaying resonances which are clearly visible in unlike-sign spectra but not so in like-sign spectra or $\rho_1 \otimes \rho_1$.

The ratios of inclusive densities are defined as follows:

$$R^{lm} = \frac{\rho_2^l}{\rho_1 \otimes \rho_1}; \qquad R^{um} = \frac{\rho_2^u}{\rho_1 \otimes \rho_1}; \qquad R^{lu} = \frac{\rho_2^l}{\rho_2^u} \tag{5.15}$$

The shortcomings of the reference distributions constructed from the data, can be corrected to first order, if both the correlated and uncorrelated distributions are divided by the relevant Monte Carlo distributions. Thus in order to discriminate BEC from other statistical and dynamical correlations, a double ratio is formed by dividing $R(T)$ obtained from data by $R(T)$ obtained from reconstructed Monte Carlo events which do not contain BEC:

$$RR(T) = \frac{R^{data}(T)}{R^{MC}(T)} \tag{5.16}$$

This procedure also corrects for the detector acceptance, and kinematic cuts. This is then fitted with the parametrisation to be tested. Since a double ratio is taken, it is clear that the normalisation applied to the mix spectra as given in equation 5.14 is arbitrary and cancels in the double ratio.

The double ratios are then fitted with modified forms of the parametrisations of equations 5.6 and 5.7:

$$RR(T) = R_0(1 + \kappa T)(1 + \lambda \exp(-r^2T^2)) \tag{5.17}$$

$$RR(T) = R_0(1 + \kappa T)(1 + \lambda \exp(-rT)) \tag{5.18}$$

The additional $(1+\kappa T)$ term is introduced to allow for long range correlations which occur at large T.

5.3 Resolution

A binning is chosen such that the bin width is everywhere smaller than the resolution in T. The variation of resolution with T is shown in figure 5.1 as determined from Monte Carlo simulation, and is consistent with that obtained from data at the K_s^0 resonance. The K_s^0 decays weakly to $\pi^+\pi^-$ with a width of 6.5 MeV as measured by H1 [62]. The width is entirely dominated by detector resolution and thus can be used to cross check the MC simulation of resolution in M or equivalently T.

5.4 Event Mixing

At HERA, events are observed at a wide range of hadronic centre of mass energies. Thus events in the data sample have very different topologies depending on where they lie in the kinematic plane. Events with large Q^2 have a current system which is boosted further forward than events at lower Q^2. Event topologies seen in the $r-\phi$ plane have a hadronic system which is balanced against the recoil of the scattered electron. When forming a mixed event it was thought that pairs taken from events with hadronic jets at different ϕ would give artificially large momentum

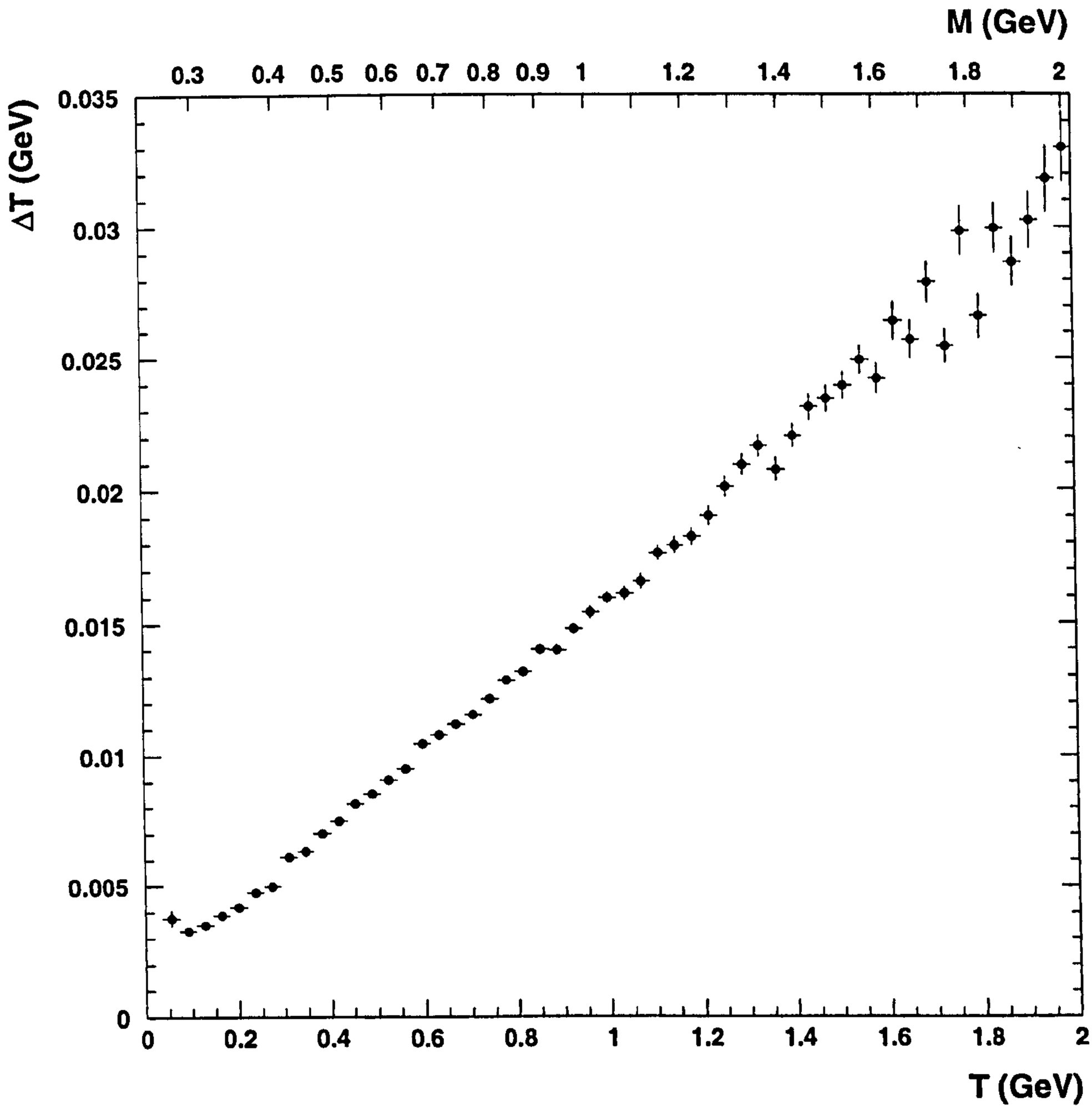

Figure 5.1: Resolution in T as determined from Monte Carlo simulation.

differences, since T is large when the angular separation of the tracks is large. In order to overcome this bias, all events were rotated in the $r-\phi$ plane such that the electron has $\phi = 0$. A similar effect is expected to hold in the $\theta - z$ plane, however this effect can be controlled by mixing events only within small kinematic regions. Mixed events were required to satisfy:

- a Q^2 difference of less than 20 GeV^2.
- a W difference of less than 20 GeV.
- a difference in multiplicity not greater than two.

The effects of these requirements were studied as systematic changes to the fit parameters and the results are described in section 5.13. A mixed event is constructed

by taking all combinations of each track in one event with all tracks in another event which satisfies the multiplicity, W, and Q^2 requirements mentioned above. Insignificant statistical errors are obtained by mixing each event with 20 others.

To ensure that the event-mixing procedure was applied correctly, cross checks were performed by comparing the event-mixed T spectra for different charge combinations. All distributions were found to agree within 4%.

5.5 Two-Particle Inclusive Densities

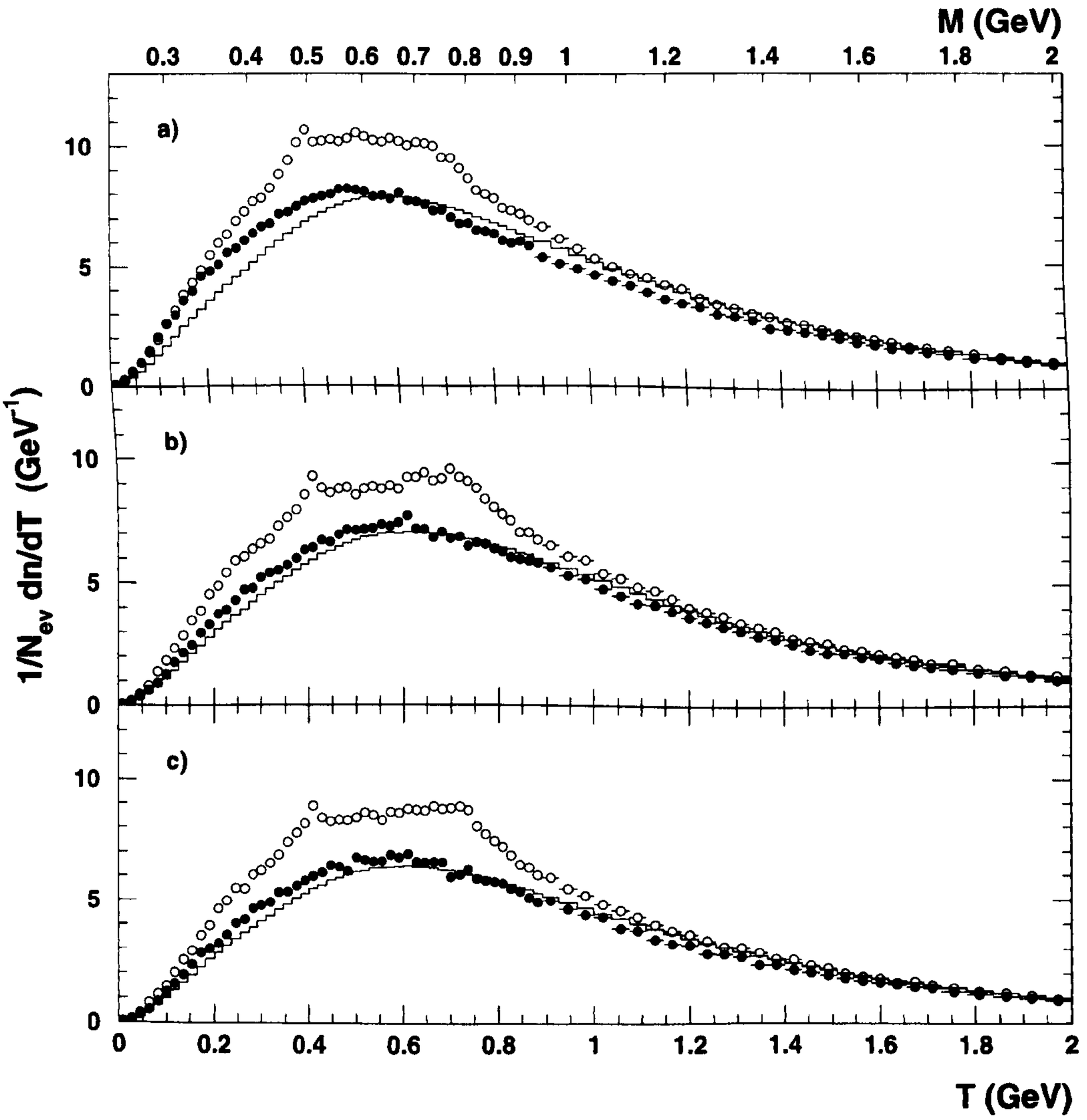

Figure 5.2: Normalised inclusive densities as a function of T showing the unlike-sign combination as open circles, like-sign pairs as closed circles and the event-mixed distribution as a solid histogram. Three uncorrected non-diffractive reconstructed data sets are shown, (a) H1 data, (b) MEAR MC, and (c) MEPS MC.

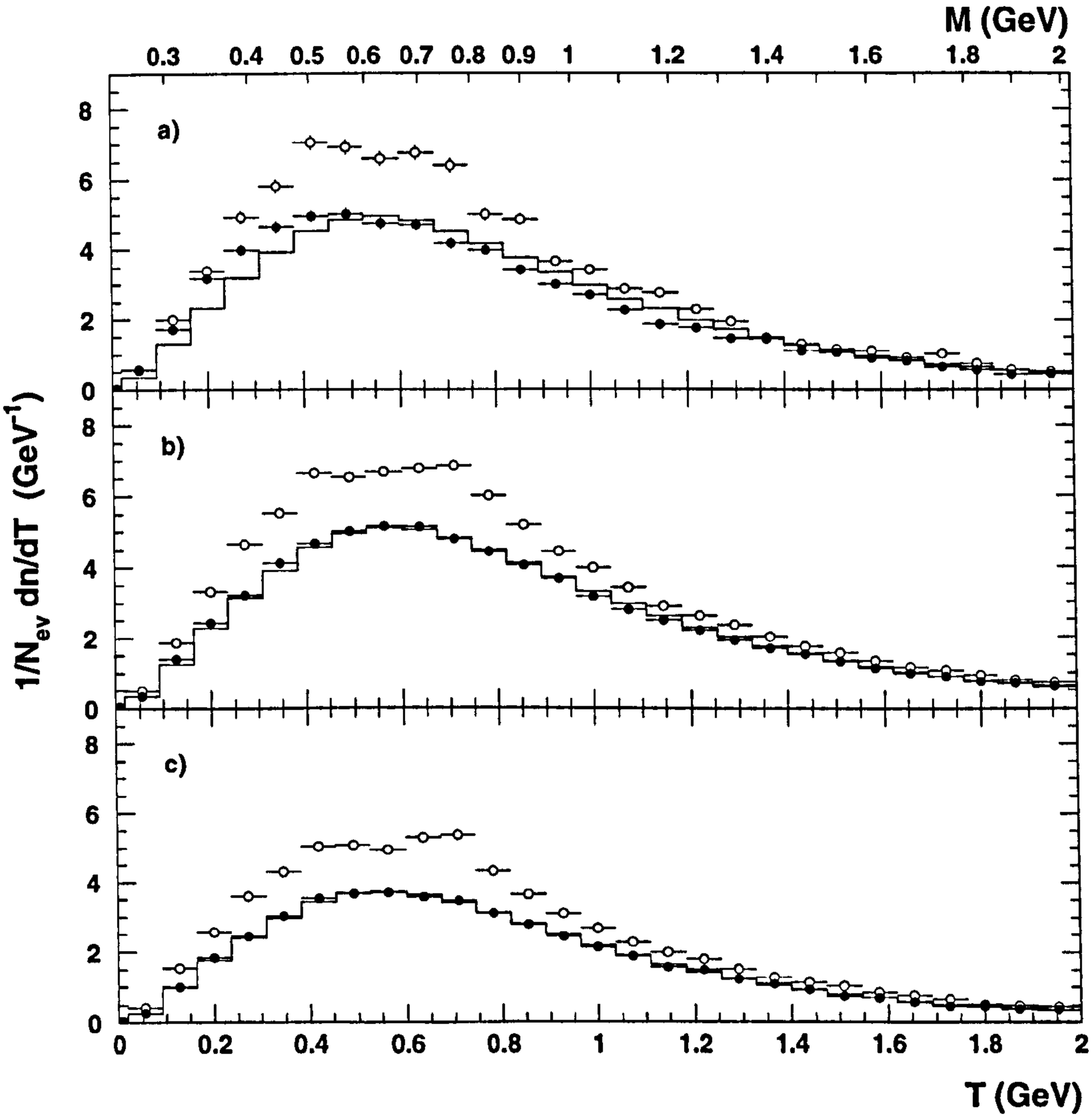

Figure 5.3: Normalised inclusive densities as a function of T showing the unlike-sign combination as open circles, like-sign pairs as closed circles and the event-mixed distribution as a solid histogram. Three uncorrected reconstructed data sets are shown, (a) H1 diffractive data, (b) RAPA MC, and (c) RAPP MC.

In figures 5.2, and 5.3 the uncorrected like, unlike and mixed densities are shown separately for the non-diffractive and diffractive samples. Each data-set is compared to two MC models: MEAR and MEPS for non-diffractive data, RAPA and RAPP for diffractive data. Both samples exhibit close similarity except for the absolute normalisation which is lower for the diffractive data. This arises simply from the the lower multiplicity of diffractive events. The unlike pair distribution contains dynamical correlations from resonance decays, most notably from the ρ^0, K^0_S, η, η' and ω. A sharp peak at $T \simeq 0.4$ GeV can be seen in ρ^u_2 which identifies the K^0_s and the broad maximum at $T \simeq 0.7$ GeV stems from the ρ^0 decay. In both the

diffractive and non-diffractive MC models indications can be seen of possible over production of the ρ^0 resonance as compared to the data. A slight shoulder visible at $T \cong 0.3$ GeV in ρ_2^u arises from the η and η' contribution (see below). In all samples ρ_2^u is more peaked than ρ_2^l in the region $0.3 \leq T \leq 0.8$ GeV and this too can be attributed to resonance decays and the fact that in a net charge neutral event there are more unlike-sign pairs than like-sign ones. The like and unlike spectra converge at large T with the mixed spectra implying that only statistical correlations exist at large invariant masses.

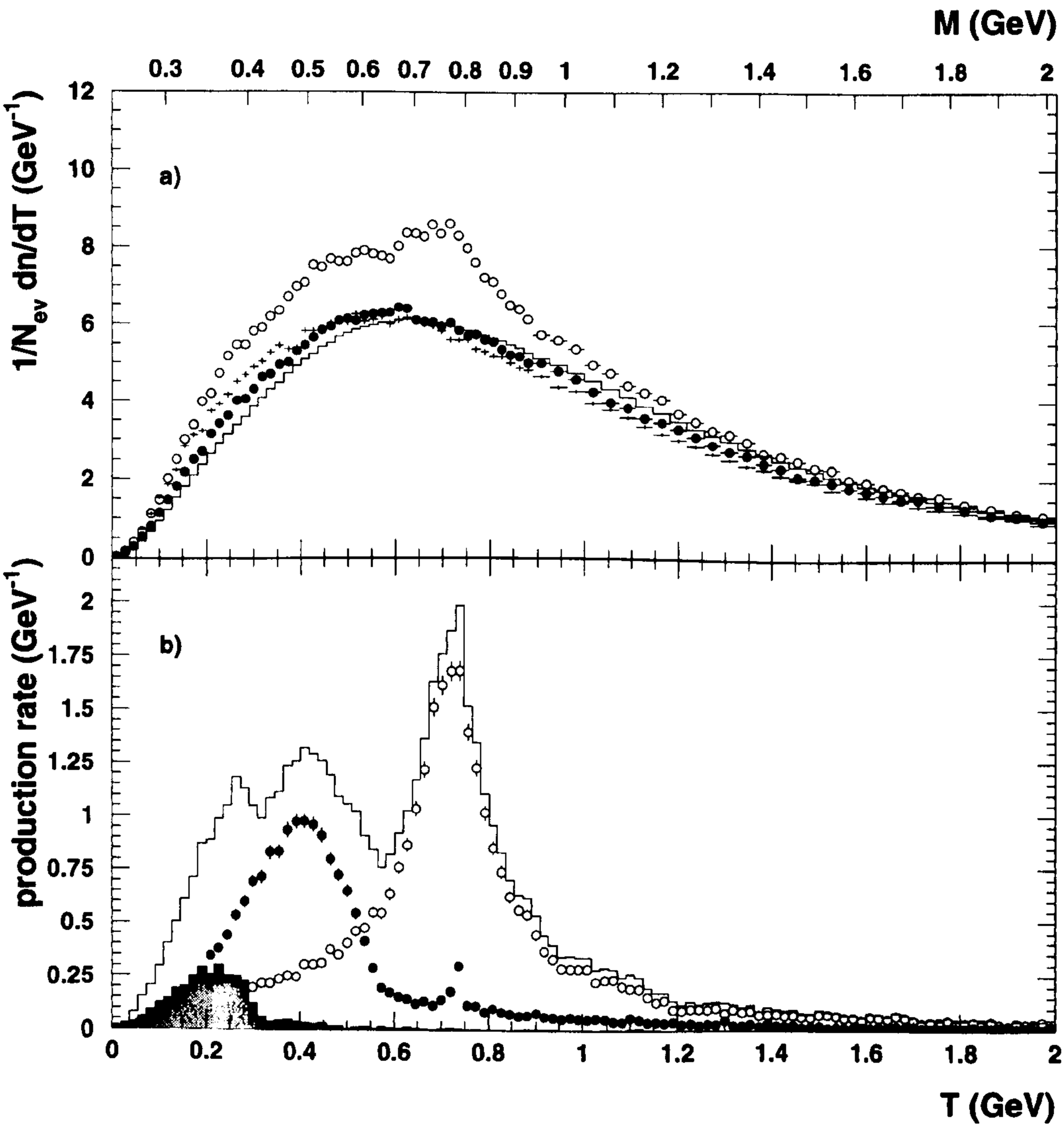

Figure 5.4: MEAR Monte Carlo predictions for the invariant mass distributions of charged particles pairs at the generator level. a) Full circles: like-sign pairs without BEC included; open circles: unlike-sign pairs; solid line: mixed pairs; crosses: like-sign pairs with BEC included. Unlike-sign pair distributions from resonance decays are shown in (b). Open circles - ρ^0; closed circles - ω; dark histogram - η'; light histogram - η; solid line - sum of all contributions.

The mixed pair sample on the other hand still differs in the topological constraints despite the precautions taken in constructing it as well as the global constraints of momentum and charge conservation.

Figure 5.4(a) shows the Monte Carlo predictions at the generator level. Since the standard Monte Carlo simulation does not include BEC, the like-sign pair distribution constitutes the ideal reference distribution for the Monte Carlo with BEC. Neither the mixed event nor the unlike-sign reference distribution agrees fully with the latter. Mixing tracks from different events shifts the distribution towards larger T, though the event-mixed distribution is a better approximation to the ideal reference than the unlike sample. The contributions from resonance decays are separately displayed in figure 5.4(b) where it can be seen that products from η, $\eta\prime$ and ω decay are more important than those from the ρ^0, since they contribute to the low mass region, where BEC appear. The K^0_S is not visible in 5.4(b) as the distribution is shown at the generator level prior to the decay of this meson. The K^0_S and ρ^0 decays cluster in a sufficiently narrow mass region, that they may be excluded in the analysis by removing the regions $0.38 - 0.43$ and $0.65 - 0.85$ GeV in T from fits using ρ^u_2 as a reference sample.

5.6 Ratios Of Inclusive Densities

In figures 5.5 and 5.6 the ratios of inclusive densities (*single ratios*) R^{um} , R^{lm} , and R^{lu} are compared with two Monte Carlo models for diffractive and non-diffractive samples. The ratio R^{um} is used as a test for the quality of the Monte Carlo since the distribution does not exhibit BEC and therefore should describe the data well. This is generally found to be the case, however, slight discrepancies exist. In figure 5.5(a) it can be seen that the ρ^0 peak is shifted to lower T in the data, this shift in the ρ^0 line shape has been previously observed and is postulated to be due to residual BEC in $\pi^+\pi^-$ pairs [65]. The region $0.1 < T < 0.3$ GeV is also overestimated by the Monte Carlo models and can be identified with the region where η and η' reflections appear (see figure 5.4). This effect is not visible in the diffractive sample. A sharp rise of R^{um} is observed at threshold in both data and Monte Carlo. The cause of this is from γ conversions where a photon converts to an e^+e^- pair and is satisfactorily modeled by the reconstructed MC.

In both R^{lm} , and R^{lu} the BEC enhancement is clearly visible for $T < 0.3$ GeV. A slow rise of R^{lm} in the Monte Carlo is observed with decreasing T below 0.3 GeV which is due to the mixing of events with different topologies. At the very smallest values of T a sharp (truncated) spike can been seen which is attributed to the double counting of tracks affecting the like-sign densities. Although the effect is partially simulated in the Monte Carlo models, it could nevertheless introduce a strong bias in the results. Therefore, the analysis is restricted to the range $T > 0.018$ GeV.

R^{lu} also exhibits distinct dips coming from the resonance contributions. In all three ratios the data and Monte Carlo agree well for $T > 1$ GeV. The absolute value of R^{lu} remains below 1 over almost the whole range in T and this reflects the larger unlike-sign pair multiplicity. All three ratios show a plateau like behaviour for $T > 1$ GeV indicating that in this region statistical correlations dominate.

5.7 Comparison of Diffractive and Non-Diffractive BEC

Table 5.1 shows the results of a Monte Carlo experiment, in which MEAR(BEC) is treated as data. It is combined in the double ratios with the standard MC without BEC simulation, and is used to assess whether the analysis methods employed are able to reproduce the inputs to the MC for the BEC simulation of r=0.53 fm and λ=1 (see appendix A for details) at both the generator and reconstructed levels. The first row shows the result, at the generator level, of a Gaussian fit to the *single ratio* formed from ρ_2^l(MEAR(BEC))/ρ_2^l(MEAR). In principle the density ρ_2^l taken from MC with no BEC simulation is the ideal reference sample in that it should contain all the effects of ρ_2^l from data *except* the Bose-Einstein enhancement. Indeed, it can be seen that this method reproduces the input value of r within errors. The extracted value of $\lambda(0.38)$ is, however, significantly reduced compared to the input value ($\lambda = 1$) and is attributed to that fact that not all charged pions are able to exhibit Bose-Einstein interference. In particular those coming from the decays of long lived resonances are known to interfere only very peripherally [70]. The effect of this can be "corrected" for and is further discussed in section 5.10 below. The

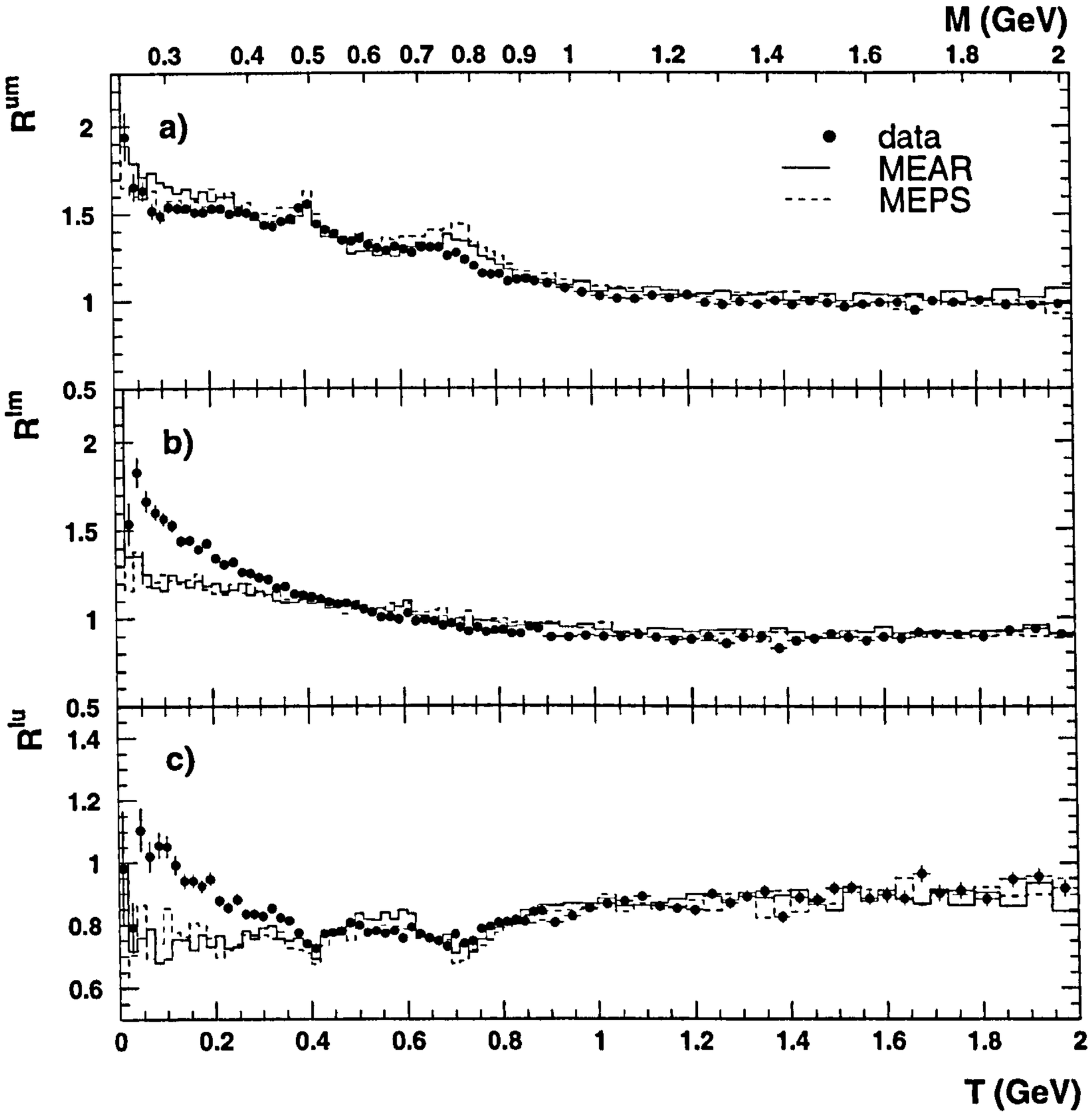

Figure 5.5: Single ratios R^{um}(a), R^{lm}(b), and R^{lu}(c) for non-diffractive data (full circles), MEAR (solid line), and MEPS (dashed line)

results of fits using the standard double ratios RR^{lm} and RR^{lu} are given in rows 2 and 3 of table 5.1. Neither of these are able to reproduce the MC input value for r at the generator, or the reconstructed level. However, it may be noted that the event-mixed reference sample gives a smaller systematic shift of 0.08 fm as compared to the shift of 0.14 – 0.18 fm from the unlike-sign reference. In addition the shifts appear stable against the effects of detector influence. From this it may be concluded that neither reference sample is perfect though the event-mixed method leads to smaller bias in the measurement.

Figure 5.7 shows the double ratios RR^{lm}, and RR^{lu} for both the event-mixed (5.7a) and the unlike-sign (5.7b) reference samples. The full circles show non-diffractive

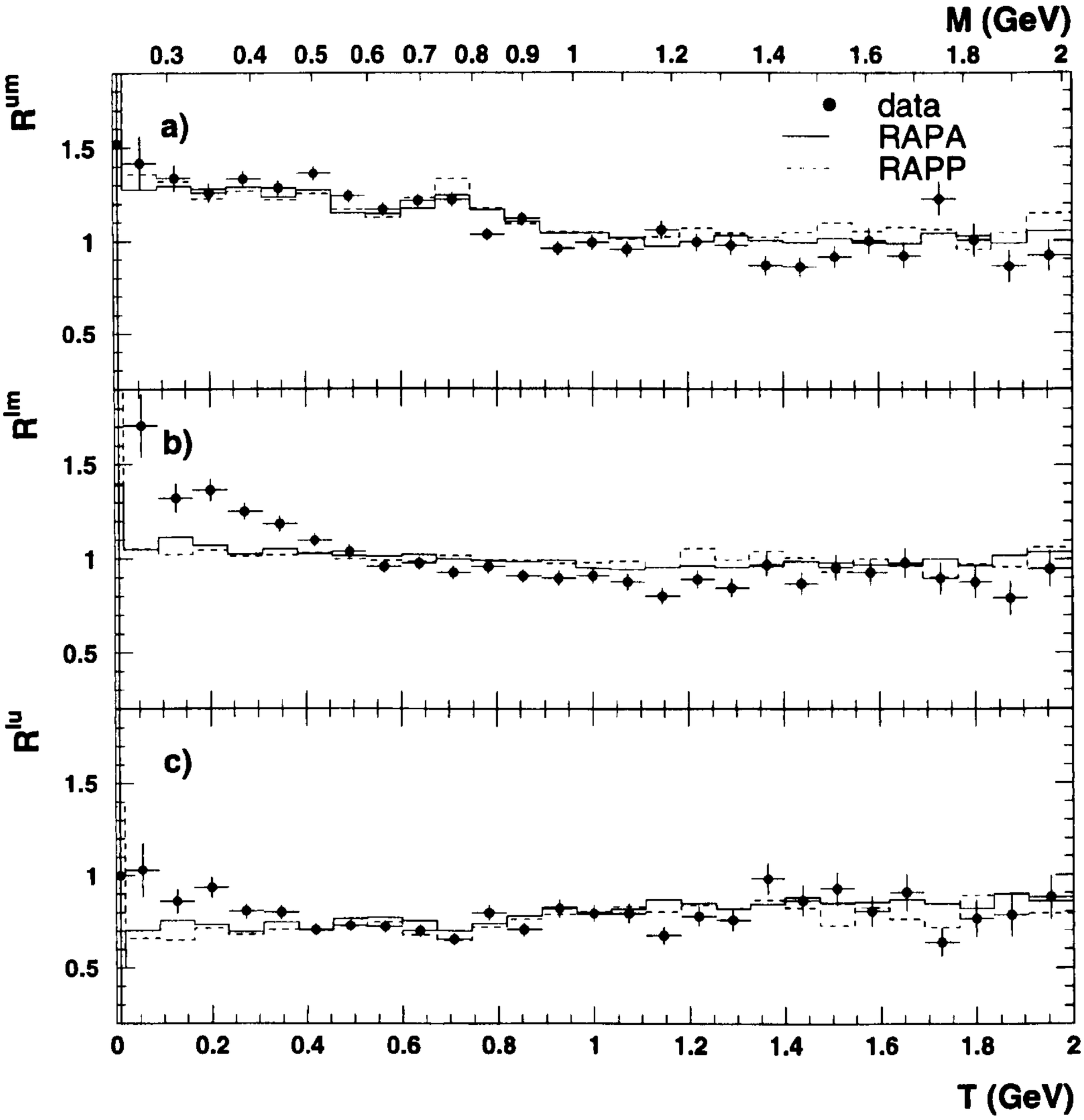

Figure 5.6: Single ratios R^{um}(a), R^{lm}(b), and R^{lu}(c)for diffractive data (full circles), RAPA (solid line), and RAPP (dashed line)

data, and the open circles show diffractive data obtained using the MEAR and RAPA MC models respectively. Each set of points has been fitted with the Gaussian parametrisation of equation 5.17 over the range $0.018 < T < 2.0$ GeV. The solid lines are fits to non-diffractive data, and the dashed lines are fits to the diffractive sample. The quantity λ is determined by the intercept at $T = 0$ and r is determined by the region in T at which the BEC enhancement begins.

The upper figure shows a slight difference in the fits to each data-set in the region of low T, though at moderate T $(0.5 - 0.8$ GeV), where the enhancement begins, no difference is visible. This indicates that the r values are similar, but that the λ values are different. However, the analysis of systematic biases in the measurement

Monte Carlo Level	Reference samples					
	like-sign $\rho_2^l(T)$		unlike-sign $\rho_2^u(T)$		event-mixed $\rho_1 \otimes \rho_1(T)$	
	r(fm)	λ	r(fm)	λ	r(fm)	λ
Gen	0.51 ± 0.02	0.38 ± 0.02				
Rec			0.67 ± 0.04	0.48 ± 0.04	0.61 ± 0.04	0.28 ± 0.02
Gen			0.71 ± 0.04	0.57 ± 0.04	0.61 ± 0.03	0.35 ± 0.02

Table 5.1: Fits to MC with BEC only using single ratios (row 1), and double ratios (rows 2 and 3). Only statistical errors are given.

of r and λ shows large systematic uncertainties in the determination of λ by as much as 50% (see section 5.13). Additionally, λ is found to be very sensitive to the pion purity as discussed in section 5.10. For this reason no emphasis is placed on the measurement of λ but is included in the following for completeness.

The lower plot of figure 5.7 shows the double ratio RR^{lu} . The regions indicated by the arrows were excluded from the fits in order to reduce sensitivity to the MC production rates of the ρ^0 and the K_s^0 . A similar procedure was not used to remove the η and the η' decay products as these cover a range in T not easily identified with a resonance peak. The ratio RR^{lu} shows a similar enhancement as RR^{lm} though the onset of the rise appears at lower T, implying a larger value of r. In this double ratio no significant differences can be seen between the two data-sets.

The values obtained for the parameters r and λ using the Gaussian fits for both the like and unlike-sign reference samples are given in table 5.2 below with statistical and systematic errors. A full discussion of the systematic error analysis is given in section 5.13.

Data set	event-mixed $\rho_1 \otimes \rho_1(T)$		
	r (fm)	λ	χ^2/ndf
non-diffractive	$0.54 \pm 0.03\ ^{+0.03}_{-0.02}$	$0.32 \pm 0.02\ ^{+0.06}_{-0.06}$	96/72
diffractive	$0.49 \pm 0.06\ ^{+0.03}_{-0.03}$	$0.46 \pm 0.08\ ^{+0.17}_{-0.08}$	18/23
Data set	unlike-sign $\rho_2^u(T)$		
	r (fm)	λ	χ^2/ndf
non-diffractive	$0.68 \pm 0.04\ ^{+0.01}_{-0.05}$	$0.52 \pm 0.03\ ^{+0.01}_{-0.21}$	77/56
diffractive	$0.59 \pm 0.13\ ^{+0.08}_{-0.07}$	$0.46 \pm 0.13\ ^{+0.25}_{-0.13}$	26/17

Table 5.2: Summary of extracted fit parameters using equation 5.17 with statistical and systematic errors for both types of reference sample.

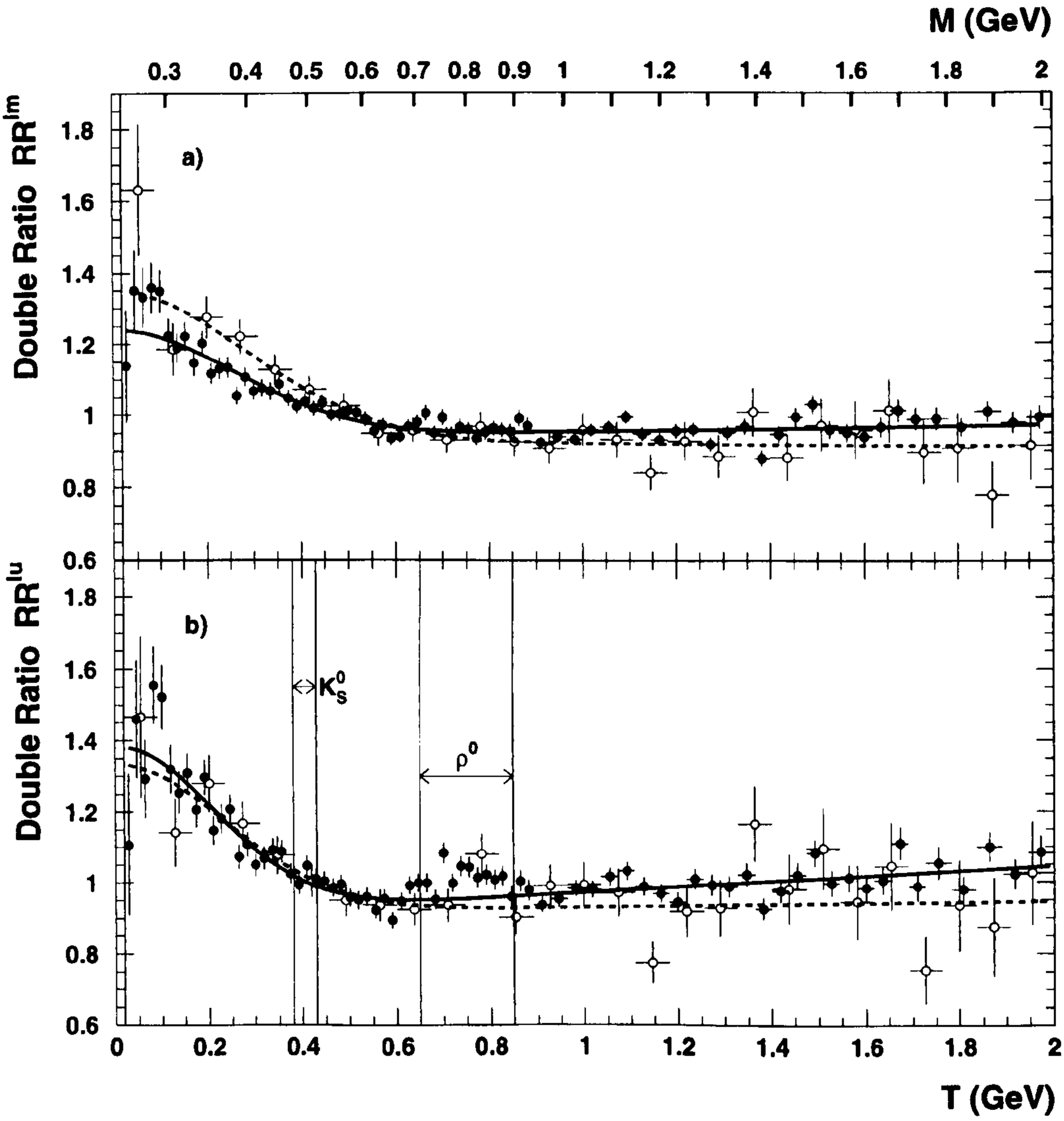

Figure 5.7: Double ratio for diffractive (open circles) and non-diffractive (full circles) data using the event-mixed (a), and unlike-sign (b) reference samples. Gaussian fits to the diffractive data (dashed line) and non-diffractive data (full line) are superimposed. Vertical lines denote regions excluded from the fits (see text).

The unlike-sign reference sample yields r values systematically larger than those from the event-mixed reference sample as observed by many experiments previously [75, 70, 76–79] and is independent of the Monte Carlo generator used. However, the event-mixed reference distribution may be favoured above the unlike-sign reference sample since it approximates an ideal reference sample better than ρ_2^u as can be seen in figure 5.4(a). Additionally, systematic uncertainties are found to be generally smaller for the event-mixed reference as will be discussed in section 5.13.

Both reference samples yield a statistically consistent value for r for the two data-sets used. Although no difference between the diffractive and non-diffractive data-sets

may have been expected, this is the first time such a comparison has been made. In addition comparison of results in BEC analyses is notoriously difficult due to the variety of cuts and analysis methods chosen. Therefore it is advantageous to be able to compare results which have undergone identical analysis chains. As no significant difference is observed, further analysis is concentrated on the non-diffractive data-set.

5.8 Kinematic Dependence of BEC

The non-diffractive data sample is large enough to allow a differential analysis of BEC across the kinematic range of the entire data-set. The data were binned in three bins of the quantities x, Q^2, and W separately. Only the event-mixed reference sample was used together with the Gaussian fit parametrisation of 5.17. Table 5.3 shows the bins used to subdivide the data which were chosen so as to equalise statistics. The results are also given in table 5.3 with statistical errors and generally show no clear evolution of BEC with x, Q^2, or W.

In addition the non-diffractive data were analysed in three subsets of observed charged particle multiplicity. The classes and the corresponding values for r and λ are listed in table 5.4. The value of the parameter r is observed to rise with increasing multiplicity. Indications for an opposite trend are noticeable for x in table 5.3. Previously H1 has observed that the multiplicity is nearly independent of Q^2, but depends weakly on W [83]. The kinematic relation $Q^2 \sim xW^2$, at small x, leads one then to expect a positive correlation of r with W and a negative correlation with x, if r increases with multiplicity. The data appear consistent with this expectation, though the effect is not significant in view of the statistical errors.

The corrected mean multiplicities[3] (obtained using the iterative migration matrix method as used in the H1 measurement of the DIS multiplicity distribution [83]) and the normalised slopes of the multiplicity dependence of r and λ taken from linear fits to the data are given in table 5.4. The corrections to the observed mean multiplicities are found to be small, at the level of 2% for the bins used. The mean values of r and λ used in the slope determination are taken from fits to the whole

[3]Many thanks to Pierre Van Mechelen for providing me with these numbers.

	r(fm) λ	r(fm) λ	r(fm) λ
x	0.60±0.06 0.30±0.03 ($0.0001 \leq x < 0.0006$)	0.56±0.05 0.34±0.03 ($0.0006 \leq x < 0.0019$)	0.44±0.06 0.38±0.07 ($0.0019 \leq x < 0.01$)
Q^2 (GeV^2)	0.52±0.04 0.42±0.04 ($6 \leq Q^2 < 12$)	0.63±0.08 0.25±0.04 ($12 \leq Q^2 < 25$)	0.47±0.04 0.41±0.05 ($25 \leq Q^2 \leq 100$)
W (GeV)	0.52±0.07 0.26±0.05 ($65 \leq W < 120$)	0.48±0.03 0.42±0.04 ($120 \leq W < 180$)	0.68±0.08 0.34±0.04 ($180 \leq W < 240$)

Table 5.3: Parameters r and λ extracted using equation 5.17 for each subset of the non-diffractive data sample. Only statistical errors are given.

Observed Multiplicity	Corrected Multiplicity	event-mixed $\rho_1 \otimes \rho_1(T)$ r(fm) λ	unlike-sign $\rho_2^u(T)$ r(fm) λ
$4 \leq n < 7$	4.9 ± 1.1	0.42±0.05 0.37±0.05	0.53±0.06 0.54±0.08
$7 \leq n < 12$	8.2 ± 1.6	0.58±0.05 0.31±0.03	0.77±0.07 0.54±0.06
$n \geq 12$	13.6 ± 2.4	0.81±0.12 0.42±0.07	0.72±0.09 0.65±0.09
$\frac{1}{<r>}\frac{dr}{dn}$		$0.085 \pm 0.026\ ^{+0.034}_{-0.048}$	$0.045 \pm 0.023\ ^{+0.021}_{-0.071}$
$\frac{1}{<\lambda>}\frac{d\lambda}{dn}$		$0.009 \pm 0.018\ ^{+0.040}_{-0.043}$	$0.024 \pm 0.026\ ^{+0.000}_{-0.054}$

Table 5.4: Parameters r, and λ extracted using equation (5.17) for different multiplicity subsets of the non-diffractive data sample. The last rows list the result for the relative slope of the two parameters with the multiplicity. The first column indicates the interval in observed multiplicity, the second column the corresponding corrected mean multiplicty.

non-diffractive data set as given in table 5.2. The slopes represent the fractional change in r or λ per unit change in multiplicity. Whereas the errors on the λ slope are large and certainly consistent with zero even within the statistical errors, the r slope shows a clear 3 standard deviation (statistical) from zero for the event-mixed reference sample. However, once systematic errors are taken into account both reference samples yield a reduced significance to the slope. The result may be compared to a similar recent measurement from the OPAL collaboration [81] where the authors find a much weaker multiplicity dependence of r, obtained using the unlike-sign reference, given by a normalised slope of 0.0036 ± 0.0006 where the quoted error is statistical[4].

[4]The authors claim that systematic uncertainties do not affect the point-to-point fluctuations, and therefore would have no influence on a determination of the slope of the multiplicity dependence.

In order to compare the multiplicity dependence with other experiments the data are shown in figure 5.8 as a function of mean particle density in the hadronic centre of mass frame. The mean particle density, $\langle dn/d\eta^* \rangle$ is obtained by scaling the corrected multiplicity by $d\eta^*$, the pseudo-rapidity[5] range covered by the CJC in the hadronic centre of mass frame which is found to be 3.2. The H1 data are compared to $p\bar{p}$ data from the E735 experiment [82] and UA1 [80] with $\sqrt{s} = 1800$ and 630 GeV respectively. Full systematic and statistical errors added in quadrature are shown for the H1 data, whilst only statistical errors are shown for the $p\bar{p}$ data. Only data obtained using the event-mixed reference sample is displayed. Reasonable agreement can be seen between ep and $p\bar{p}$ data, though there are indications of a stronger dependence in the H1 data. Further analysis of systematic uncertainties arising mainly from the background parametrisation and detector resolution would be required before a more definitive statement can be made.

It may be concluded that evidence for the multiplicity dependence of r has been observed, though the apparently weaker dependence when using the unlike-sign reference is not understood. In both cases the slope is found to be an order of magnitude larger than that found in e^+e^- data.

5.9 Comparison of BEC Parametrisations

In this section the three parametrisations of BEC given by equations 5.17, 5.18, and 5.8 are compared. The data are shown in figure 5.9 with the three fits superimposed. All three parametrisations provide a good description of the data, however, at threshold the Gaussian fit does not follow the data as well as the exponential or power-law fits. The data exhibit a faster than Gaussian rise with decreasing T. The results are given with statistical errors in table 5.5 below including the χ^2 values for each fit.

The reduced χ^2 values favour the exponential fits, though the larger χ^2 of the power-law is due to the data points at large T rather than a worse description of the BEC enhancement at threshold. To quantify this the data were fitted with a power-law over the reduced range $0.018 < T < 1.0$ to yield $\beta = 1.20 \pm 0.15$ and χ^2/ndf=49/49

[5]Pseudo-rapidity is defined as $-\ln(\tan\theta/2)$.

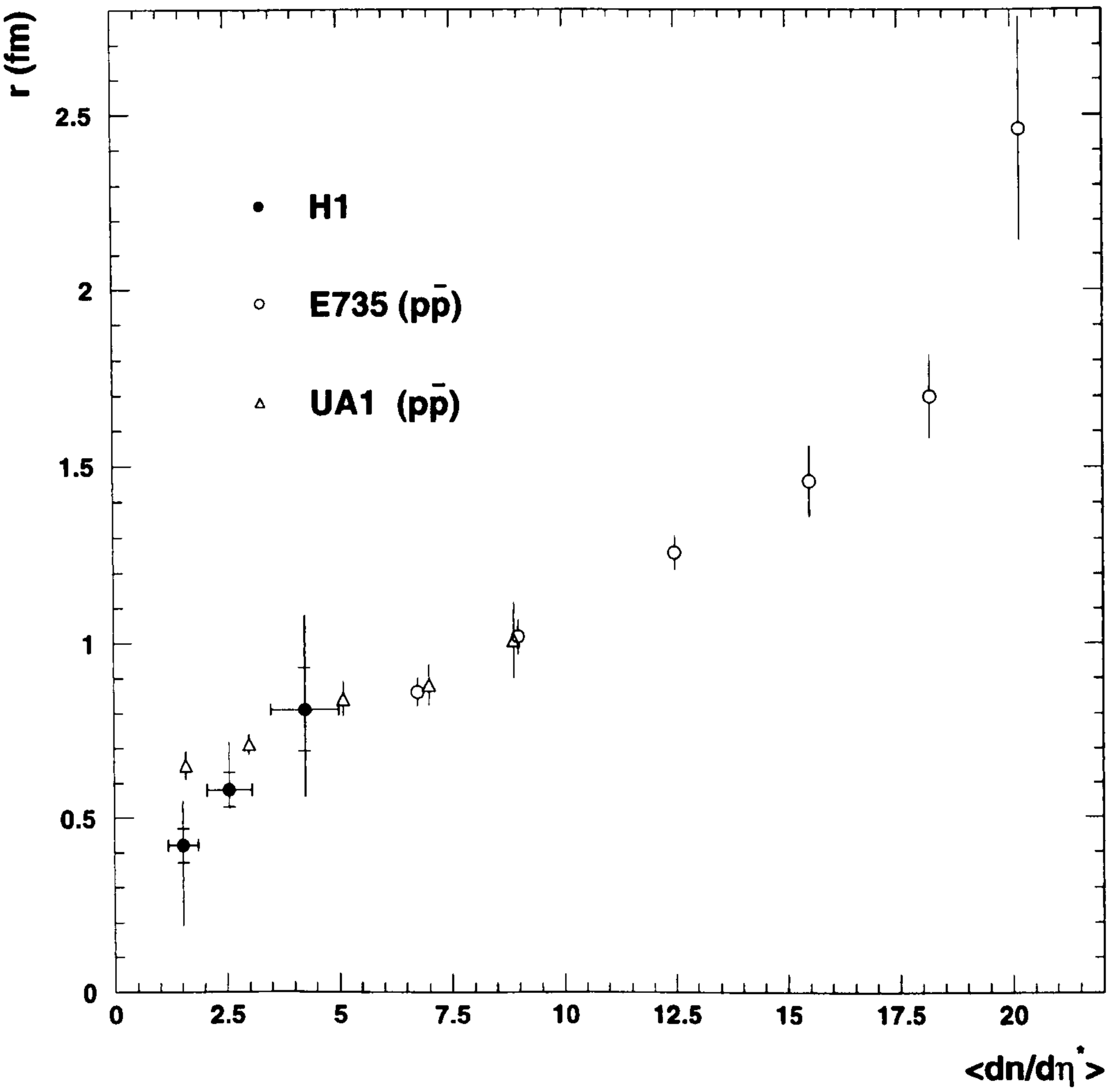

Figure 5.8: The radius parameter r versus $\langle dn/d\eta^* \rangle$. The full circles are from this analysis, the open circles (triangles) are from $p\bar{p}$ data at a centre of mass energy of 1.8 TeV [82] (630 GeV [80]). For the H1 data points the inner errors are statistical and the outer errors are the sum of statistical and systematic errors added in quadrature. The $p\bar{p}$ data are shown with statistical errors only.

for RR^{lm}. Thus, an improved χ^2 is attained with a compatible value for β.

5.10 Purity Corrections

It is known that pions from long lived resonances do not contribute to a *measurable* Bose-Einstein enhancement. The DELPHI collaboration [70] have shown that a data sample enriched with b quarks (yielding long lived B mesons) results in a decrease of the λ parameter, i.e. the BEC effect is attenuated by pions originating from sources separated by several fermi. Correction for the "dilution" of the BEC

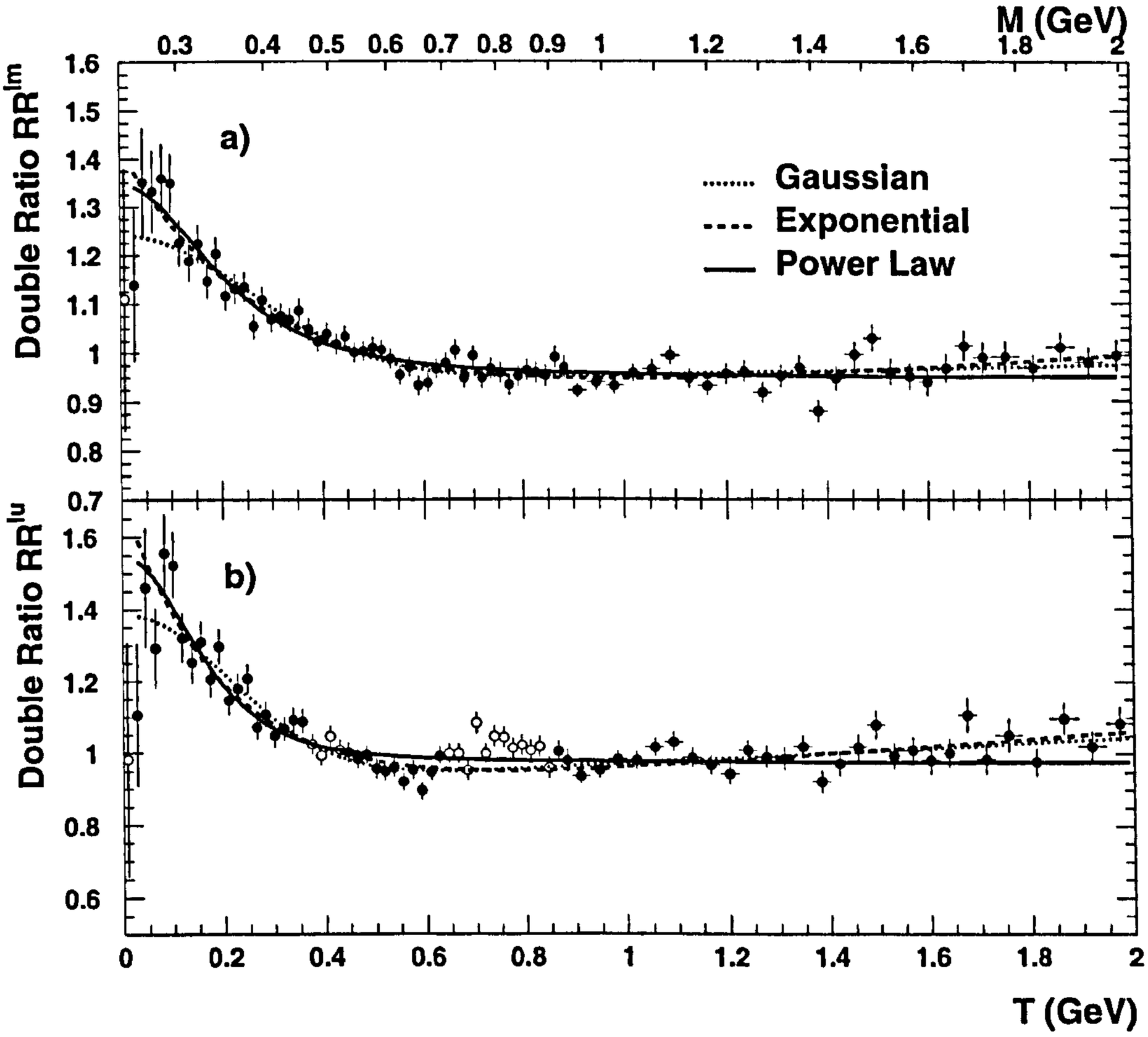

Figure 5.9: Double ratios for non-diffractive DIS data using MEAR Monte Carlo and the mixed reference smaple in (a), and the unlike-sign reference sample in (b). Three fit parametrisations are superimposed. The closed circles are data included in the fits, whilst the open circles are the excluded bins.

effect by non-direct pion pairs have been made by the OPAL and ALEPH collaborations [76, 78]. The correction results in an increase of λ towards 1 as expected, though no changes in r were observed. Pions from short lived resonances and those produced directly from the string cannot be identified in the data, and therefore, a correction for the *origin* of particles can only be obtained from MC. Since there is only one model available in this analysis from which to extract the correction (JETSET), and the correction, in any case, is known to affect λ values only, it was decided not to routinely apply a purity correction to all the results.

Following the method of DELPHI [70] a pion purity corrected result may be obtained

Power law	β	B [GeV^{-2}]	A	χ^2/ndf
RR^{lu}	$2.39 \pm 0.20\ ^{+0.07}_{-0.60}$	$0.001 \pm 0.001\ ^{+0.003}_{-0.001}$	$0.98 \pm 0.01\ ^{+0.02}_{-0.02}$	121/57
RR^{lm}	$1.52 \pm 0.12\ ^{+0.38}_{-0.28}$	$0.008 \pm 0.002\ ^{+0.007}_{-0.005}$	$0.96 \pm 0.01\ ^{+0.02}_{-0.02}$	103/73
Exponential	δ [GeV^{-1}]	r [fm]	λ	χ^2/ndf
RR^{lu}	0.13 ± 0.02	$0.99 \pm 0.09\ ^{+0.02}_{-0.27}$	$1.00 \pm 0.08\ ^{+0.56}_{-0.38}$	85/56
RR^{lm}	0.08 ± 0.04	$0.68 \pm 0.11\ ^{+0.09}_{-0.05}$	$0.64 \pm 0.06\ ^{+0.17}_{-0.10}$	85/72
Gaussian	δ [GeV^{-1}]	r [fm]	λ	χ^2/ndf
RR^{lu}	0.08 ± 0.02	$0.68 \pm 0.04\ ^{+0.01}_{-0.05}$	$0.52 \pm 0.03\ ^{+0.01}_{-0.21}$	77/56
RR^{lm}	0.02 ± 0.01	$0.54 \pm 0.03\ ^{+0.03}_{-0.02}$	$0.32 \pm 0.02\ ^{+0.06}_{-0.06}$	96/72

Table 5.5: Results from exponential (equation 5.18), Gaussian (equation 5.17), and power-law (equation 5.8) fits to non-diffractive data using both reference samples.

by fitting the double ratio RR^{lm} with a further modified form of the Gaussian fit:

$$RR(T) = R_0(1 + \kappa T)(1 + \lambda \cdot f^l(T) \exp(-r^2T^2)) \tag{5.19}$$

where $f^l(T)$ is the fraction of direct like-sign pion pairs to all like-sign particle pairs. Direct is taken to mean particles which come directly from the string, or from short lived resonance states. Long lived resonances are taken to be those with a lifetime larger than the $K^*(892)$. This fraction is displayed in figure 5.10a and is well parametrised by the quadratic function

$$f^l(T) = 0.276 + 0.208T - 0.078T^2 \tag{5.20}$$

This function is used in equation 5.19 to obtain the corrected values for r and λ.

A correction may also be applied to the unlike-sign double ratio, RR^{lu} . This is achieved by weighting the data bin-by-bin with the fraction $f^l(T)/f^u(T)$ where $f^u(T)$ is the analogous fraction for unlike-sign pairs and is displayed in figure 5.10b showing distinct resonance behaviour. The weighted double ratio is then fitted with the standard function of equation 5.17.

The results of the purity correction to the entire non-diffractive data-set are shown in table 5.6 where MEAR has been used to form all double ratios. The effect of the purity correction is the same in both cases, in that the r parameters are largely unaffected, whereas the λ values are altered dramatically to become consistent with 1. Thus, by removing the effect of decay products from long lived resonances and of charged particles other than pions the BEC effect is found to be maximal.

Data set	r (fm)	λ	χ^2/ndf
RR^{lm} corrected	0.59 ± 0.03	1.07 ± 0.07	100/72
RR^{lm} uncorrected	0.54 ± 0.03	0.32 ± 0.02	96/72
RR^{lu} corrected	0.62 ± 0.03	1.08 ± 0.08	51/56
RR^{lu} uncorrected	0.68 ± 0.04	0.52 ± 0.03	77/56

Table 5.6: Comparison of extracted fit parameters for purity correction. The Gaussian model is used for fits (see text), and non-diffractive data with MEAR MC.

5.11 QED Corrections

The effects of QED corrections were examined using the Monte Carlo generator DJANGO [36] which is described in section 3. Non-diffractive events were generated with and without full QED effects to first order in α and are referred to as the radiative and non-radiative samples respectively. To correct the two-particle densities back to the (non-radiative) Born term, the ratio of non-radiative to radiative distribution is formed for each inclusive two-particle density. The ratio is the correction to be applied to the data and is shown in figure 5.11 for the like, unlike, and event-mixed densities. The corrections are small, less than 10% on average, and smoothly varying within the statistical fluctuations. The solid line represents no correction and is plotted to guide the eye. The points were fitted with a linear parametrisation in order to determine a functional correction which would suppress the statistical fluctuations compared to application of a bin-by-bin correction. However, independent fits to all three correction factors produced a consistent parametrisation within errors, which suppressed pair rates at low T by 2%, and enhanced pair rates at large T by 5%. This can be understood if one views the correction coming mainly from initial state QED radiation of a real photon from the beam electron. In this case the effective $\gamma^* p$ centre of mass energy is reduced, and so the phase space for producing large invariant mass pairs is also reduced. Since the functional corrections are the same in all three cases, their effects would cancel in the ratios $R(T)$ and so no QED corrections are applied to the data.

5.12 Final State Interactions

A final state of two or more charged bosons is affected by strong and electromagnetic interactions. The strong interactions are difficult to calculate, and in particular it is hard to distinguish between the initial and final stages of the hadronisation. An

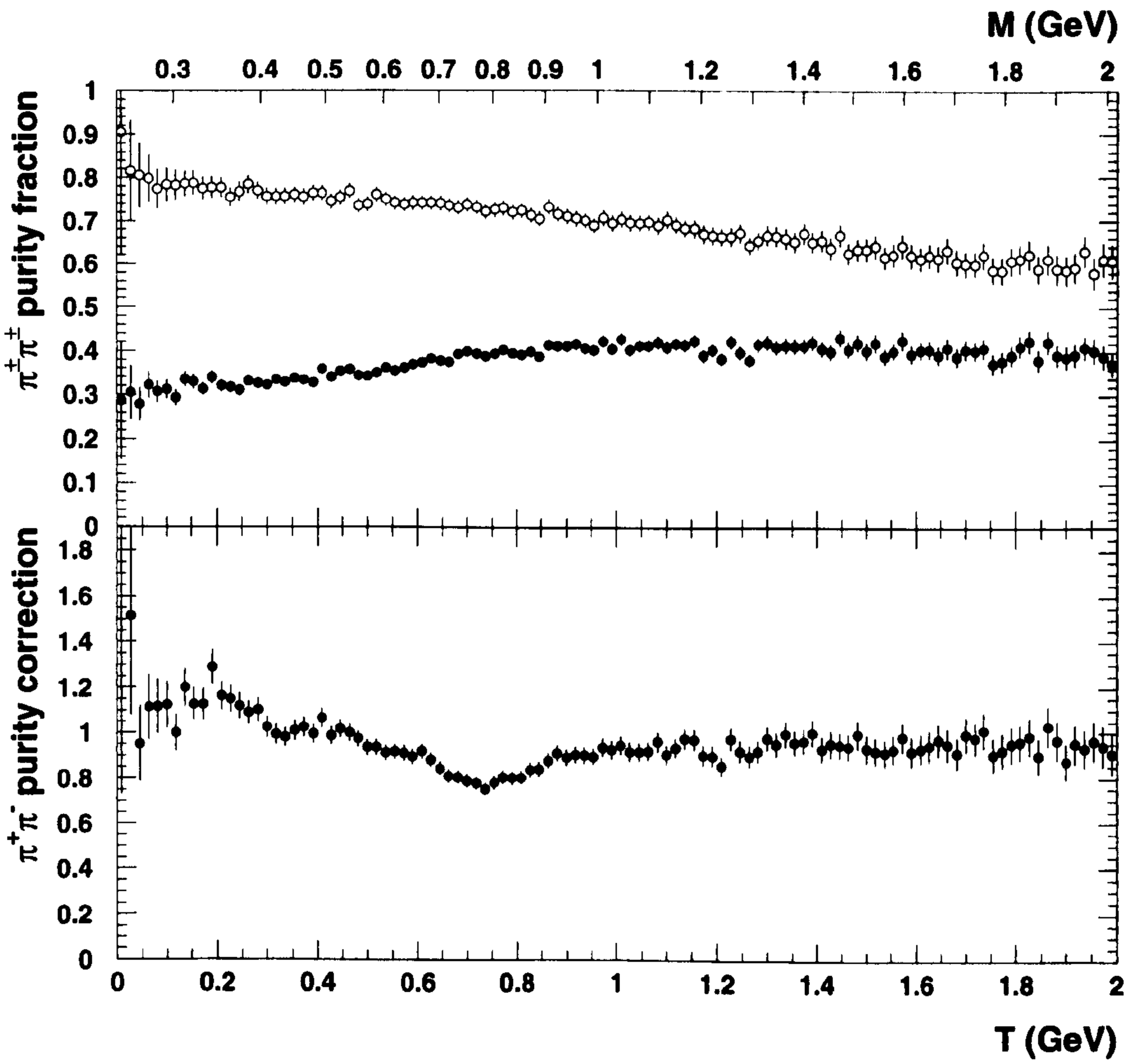

Figure 5.10: The upper plot shows the ratio of like-sign pion pairs to all like-sign particle pairs (open circles), and the ratio of direct like-sign pion pairs to all like-sign particle pairs(full circles). The lower plot shows the unlike-sign pion purity correction (see text).

estimate of the effects of $\pi\pi-$scattering has been made by Suzuki [71], and indicates minor influences on the BEC analysis. This was not considered any further.

The Coulomb forces between charged pairs of particles are expected to modify the two particle correlation. Since two unlike (like) charged particles experience electromagnetic attraction (repulsion), the number of pairs in the region of small relative momenta is enhanced (suppressed). The correction factors for this effect have been estimated and are known as Gamov factors. These corrections are generally small, and only rise above 5% in the region of $T < 0.05$ GeV. The sensitivity to this correction has been investigated by weighting the two-particle inclusive densities with the

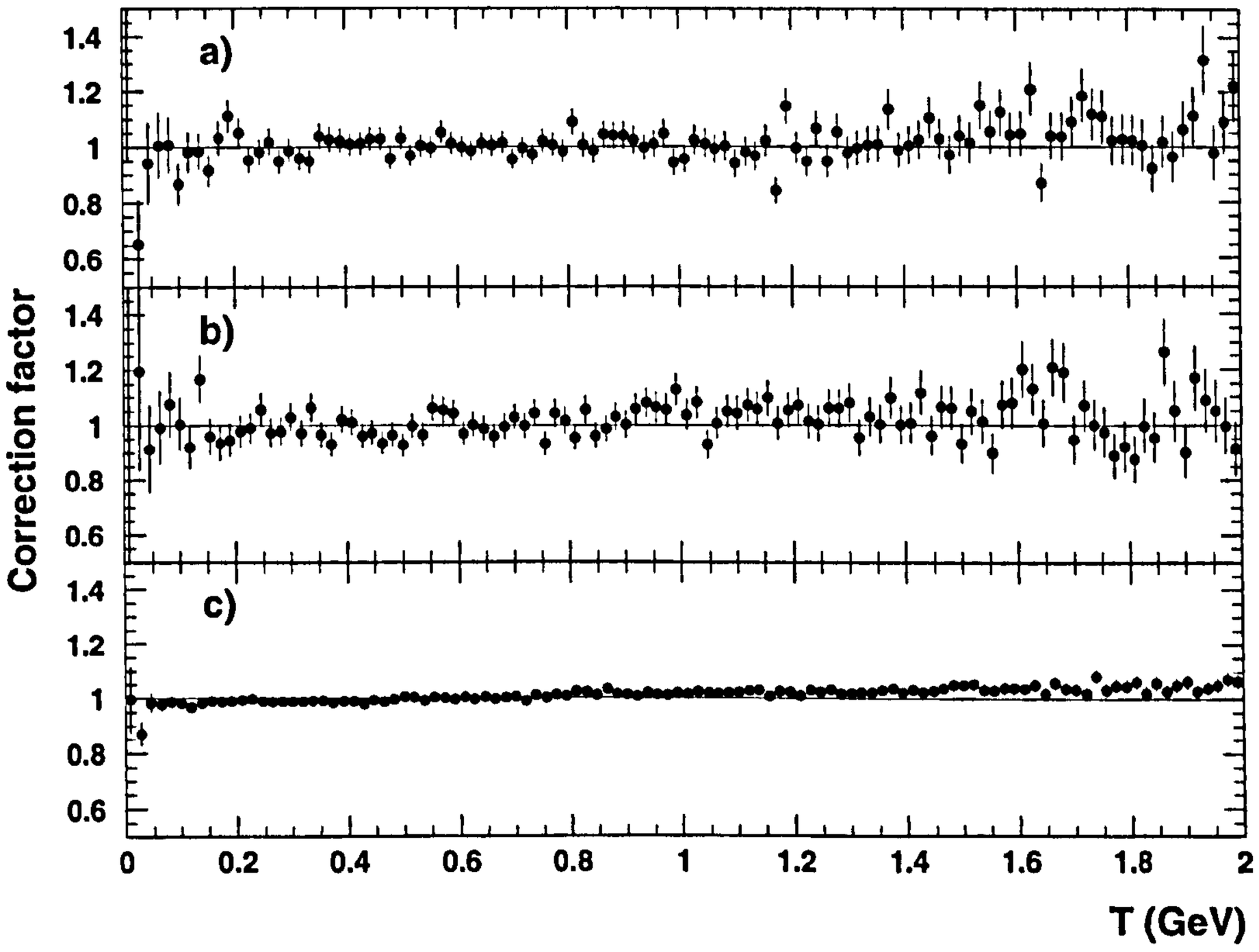

Figure 5.11: Correction function to the two-particle inclusive densities for QED radiative effects for a) like-signs, b) unlike-signs, c) event-mixed distributions.

corresponding Gamov factor, and refitting the data set. Neither λ nor r were seen to change outside the statistical errors. More precise calculations [73, 74] indicate that the Coulomb corrections to BEC are somewhat exaggerated by applying the Gamov factors.

5.13 Systematic Errors

In order to assess the stability of results with respect to assumptions made in the analysis and the effects of cuts etc. a number of checks have been made. The systematic errors which were investigated are listed below. These were thought to have a possible effect on the parameters extracted from the fits to the correlation

function. Each quantity was varied and the difference in fit parameters is then quoted as the estimate of the systematic error. All the significant errors were then added in quadrature resulting in the total systematic error.

- **Detector Resolution.** The effects of resolution smearing and inefficiencies can be tested in a Monte Carlo experiment where Monte Carlo with BEC is treated as data. The analysis is performed at the generated and reconstructed levels. Any difference in the fit parameters is taken as a systematic error arising from detector influence.

- **Model Dependency.** Since a double ratio of data to Monte Carlo is taken there is an explicit model dependency. The size of this can be estimated by comparison of results using two different Monte Carlos.

- **Dependency on Long Range Correlations.** To take into account long range correlations, extra quadratic factors were included in the fit functions for the Gaussian and exponential fits, namely:

$$RR(T) = R_0(1 + \kappa T + \xi T^2)(1 + \lambda \exp(-r^2 T^2)) \tag{5.21}$$

and

$$RR(T) = R_0(1 + \kappa T + \xi T^2)(1 + \lambda \exp(-rT)) \tag{5.22}$$

In addition the fits were performed over a reduced range in T upto 1.2 GeV. The error is taken as the largest deviation.

- **Differences in Track Charge.** Differences in detector response to positive and negatively charged particles could cause systematic shifts of the data. Therefore, positive and negative tracks are analysed separately.

- **Event-Mixing.** The method used in forming mixed events may also influence the results. This was tested by repeating the analysis but requiring more stringent restrictions on the mixing of events. Specifically the requirements were tightened to $\Delta W < 10$ GeV, and $\Delta Q^2 < 10$ GeV^2.

- **Split Track Pairs.** To assess the influence of the remaining rate of split tracks the fits were repeated but with the lower limit in T of the fit raised to 0.036 GeV.

- **Track Selection.** The track selection criteria were altered by requiring tracks to have a radial track length of 10 cm, and no requirement on the total number of CJC hits was demanded.

- **Binning.** The extracted parameters should be independent of the way the data are binned. To test the influence of binning the data were binned with half and double the nominal bin width.

- **Resonances.** For fits using the unlike-sign reference set the regions of the ρ^0, and the K_s^0 resonances were routinely excluded. To determine the sensitivity of the results on the size of the exclusion zones the data were refitted with exclusion ranges reduced to half the nominal range used in the standard analysis.

Tables 5.7-5.11 summarise the systematic errors for each data sample and each fit parametrisation. The effects of binning, track selection, event-mixing, split pairs, and resonances were found to be negligible, i.e. variations were always within statistical errors, and therefore were not included in the final calculation of the systematic errors. In order to compare the size of the systematic uncertainties, the statistical errors are also shown. In addition table 5.7 also shows the deviations obtained from the MC experiment of table 5.1. These deviations were not included in the total systematic error and are shown for comparison.

In order to test whether the analysis of the diffractive data is sensitive to the details of the pomeron structure function used in the diffractive Monte Carlo models, the measurement was repeated after application of the cut $Q^2 > 10$ GeV^2. This additional selection reduces the discrepancy between data and Monte Carlo to the level of $\sim 15\%$ in the high y region (see section 4.5). No deviation of the Gaussian fit parameters for either the diffractive or non-diffractive samples was observed outside the statistical errors.

Due to a lack of reconstructed diffractive Monte Carlo with BEC simulated, no systematic shift has been evaluated for detector resolution in the diffractive measurement. However, one may expect this contribution to the systematic error to be of similar size to the non-diffractive estimate, i.e. $\sim$7% for r, and $\sim$20% for λ. No event-mixing systematic was determined for the non-diffractive data, though the

effect is negligible as expected from the estimate from the diffractive data-set.

In general it can be seen that the systematic fluctuations on r are of the order of $\sim$10%, whilst those on λ are of the order of $\sim$40% for both the Gaussian and exponential fits. It appears that λ is much more sensitive to the influence of the background parametrisation and to the model dependency compared to r. Furthermore, comparison of the systematic deviations reveals that the errors are smaller for the event-mixed reference sample than for the unlike-sign reference.

The β parameter of the power-law model has about 25% systematic errors for both reference samples mainly coming from the background parametrisation, which in this case was obtained from fits over the reduced range of $0.018 < T < 1.2$ GeV.

To assess the significance of the observed multiplicity dependence, systematic errors have been estimated as above for the three multiplicity bins. This was not repeated for the other kinematic dependencies as the statistical errors in those cases are too large to exhibit any clear evolution as may be expected in the W dependence. These systematics are given in table 5.11. They show similar behaviour as seen in the other tables, in that errors on λ are larger than those on r, except in the lowest multiplicity bin. Here, the dominant error on r arises from detector resolution obtained from Monte Carlo. No track charge systematic was evaluated for these sub-samples and so the estimates uncertainties obtained from the entire non-diffractive data-set of table 5.7 have been used.

	unlike-sign $\rho_2^u(T)$		event-mixed $\rho_1 \otimes \rho_1(T)$	
	δr(fm)	$\delta\lambda$	δr(fm)	$\delta\lambda$
Resolution	−0.04	−0.09	±0.00	−0.06
Background parametrisation	−0.01	+0.01	+0.02	±0.00
Models	−0.02	−0.19	±0.00	+0.06
Track charge	±0.01	±0.01	±0.02	±0.02
Sum	+0.01	+0.01	+0.03	+0.06
(quadratic)	−0.05	−0.21	−0.02	−0.06
reference sample †	+0.18	+0.19	+0.08	−0.03
statistical error	±0.04	±0.03	±0.03	±0.02

Table 5.7: Contributions to the systematic errors for the non-diffractive data-sample using the Gaussian fits of equation 5.17. † Shift observed in the Monte Carlo compared to an ideal reference distribution (see text and Table 5.1).

	unlike-sign $\rho_2^u(T)$		event-mixed $\rho_1 \otimes \rho_1(T)$	
	δr(fm)	$\delta\lambda$	δr(fm)	$\delta\lambda$
Background parametrisations	± 0.04	$+0.23$	± 0.01	$+0.13$
Models	$+0.03$	$+0.11$	-0.01	$+0.08$
Track charge	± 0.06	-0.13	± 0.03	± 0.08
Sum	$+0.08$	$+0.25$	$+0.03$	$+0.17$
(quadratic)	-0.07	-0.13	-0.03	-0.08
Statistical error	± 0.13	± 0.13	± 0.06	± 0.08

Table 5.8: Contributions to the systematic errors for the diffractive data-sample.

	unlike-sign $\rho_2^u(T)$		event-mixed $\rho_1 \otimes \rho_1(T)$	
	δr(fm)	$\delta\lambda$	δr(fm)	$\delta\lambda$
Resolution	$+0.02$	$+0.15$	-0.04	$+0.11$
Background parametrisation	-0.27	$+0.54$	$+0.08$	-0.09
Models	-0.04	-0.38	$+0.04$	$+0.12$
Track charge	± 0.01	± 0.02	± 0.03	± 0.05
Sum	$+0.02$	$+0.56$	$+0.09$	$+0.17$
(quadratic)	-0.27	-0.38	-0.05	-0.10
Statistical error	± 0.09	± 0.08	± 0.11	± 0.06

Table 5.9: Contributions to the systematic errors for the non-diffractive data-sample using the exponential fit of equation 5.18.

5.14 Comparison with other Experiments

Table 5.12 summarises the results from other experiments. The errors are only statistical. Different experiments used different data treatments, e.g. sometimes purity correction or Coulomb corrections were applied. These corrections mainly influence the parameter λ, which may explain the larger differences observed here. The values of r extracted with a mixed reference sample are systematically lower than those obtained with an unlike-sign background, which is observed in this analysis too. However, the measured radii are more consistent with each other, considering the systematic errors, which have not in all cases been evaluated, but should be of the same order of as in this experiment. The fact that the data from ℓN–scattering are independent of the energy, and furthermore agree with those from e^+e^-–annihilation at various centre of mass energies, seems to lend support to the string model interpretation, where the "source dimension" is constant.

	unlike-sign $\rho_2^u(T)$			event-mixed $\rho_1 \otimes \rho_1(T)$		
	$\delta\beta$	δB	δA	$\delta\beta$	δB	δA
Resolution	-0.07	$+0.001$	± 0.00	-0.19	$+0.005$	$+0.01$
Background parametrisation	-0.28	$+0.002$	-0.02	-0.20	$+0.005$	-0.02
Models	-0.52	$+0.002$	$+0.02$	$+0.38$	-0.005	$+0.02$
Track charge	± 0.07	± 0.001	± 0.00	± 0.04	± 0.001	± 0.01
Sum	$+0.07$	$+0.003$	$+0.02$	$+0.38$	$+0.007$	$+0.02$
(quadratic)	-0.60	-0.001	-0.02	-0.28	-0.005	-0.02
Statistical error	± 0.20	± 0.001	± 0.01	± 0.12	± 0.002	± 0.01

Table 5.10: Contributions to the systematic errors for the non-diffractive data-sample using power law fits of equation 5.8.

	event-mixed $\rho_1 \otimes \rho_1(T)$					
	$\langle n \rangle = 4.9$		$\langle n \rangle = 8.2$		$\langle n \rangle = 13.6$	
	r(fm)	λ	r(fm)	λ	r(fm)	λ
Resolution	-0.22	$+0.20$	$+0.13$	$+0.03$	-0.12	-0.03
Background par.	$+0.11$	-0.23	$+0.03$	-0.03	$+0.24$	$+0.04$
Models	$+0.04$	$+0.13$	$+0.01$	$+0.01$	-0.18	-0.04
Track charge	± 0.02	± 0.02	± 0.02	± 0.02	± 0.02	± 0.02
Sum	$+0.12$	$+0.24$	$+0.13$	$+0.04$	$+0.24$	$+0.02$
(quadratic)	-0.22	-0.23	-0.02	-0.04	-0.22	-0.07
Statistical error	± 0.05	± 0.05	± 0.05	± 0.03	± 0.12	± 0.07

Table 5.11: Contributions to the systematic errors for the non-diffractive data-sample using the Gaussian fits of equation 5.17 for the three multiplicity classes.

	EXPERIMENT	unlike-sign $\rho_2^u(T)$		event-mixed $\rho_1 \otimes \rho_1$		$\sqrt{s}$
		r(fm)	λ	r(fm)	λ	[GeV]
ℓN	EMC (μp)	0.84±0.03	1.08±0.10	0.46±0.03	0.73±0.06	23
	E665 (μp)			0.39±0.02	0.35±0.02	30
	BBCNC (νN)	0.80±0.04	0.61±0.04	0.64±0.04	0.46±0.03	10-28
	H1	0.69±0.03	0.55±0.03	0.53±0.02	0.32±0.02	300
e^+e^-	DELPHI	0.83±0.03	0.31±0.02	0.47±0.03	0.24±0.02	91
	ALEPH	0.80±0.04	0.62±0.04	0.50±0.02	0.40±0.02	91
	OPAL	0.93±0.02	0.86±0.03			91
	MARK 2	0.84±0.06	0.50±0.07			29 (3)
	TASSO	0.80±0.06	0.35±0.07			34
	AMY	0.73±0.05	0.47±0.05	0.58±0.06	0.39±0.02	58
	VEPP	0.73±0.11	0.71±0.16			9.5 (7-10)
	CLEO	0.54±0.10	0.99±0.14			9.5 (7-10)

Table 5.12: Results from other experiments

Chapter 6

Summary and Conclusions

The work presented in this thesis is an analysis of Bose-Einstein Correlations in diffractive and non-diffractive deep inelastic scattering. The data are restricted to the kinematic region defined by:

- $157° \leq \theta_e \leq 172.5°$
- $E'_e \geq 12$ GeV.
- $W^2 > 4400$ GeV^2 as calculated from the Jaquet-Blondel, and electron method.

The data are split into diffractive and non-diffractive components by requiring diffractive events to display little activity in the forward regions of the detector. Further kinematic requirements are:

- $\eta_{max} < 3.0$
- $x_{I\!P} \leq 0.05$

After all selections the non-diffractive sample consists of 48 000 events and the diffractive sample contains 2 500 events. Tracks are selected within the region:

- $p_t > 0.15$ GeV
- $22° < \theta < 150°$

Additional selections are used to remove split tracks. The data are analysed in terms of the pair four-momentum difference T separately for like and unlike-sign pairs. The analysis is performed in the region $0.018 < T < 2.0$. When using unlike-sign reference sample the regions of the K^0_S, and the ρ^0 resonances are removed:

$0.38 < T < 0.43$, and $0.65 < T < 0.85$ GeV respectively.

Monte Carlo studies have shown that neither the event-mixed, nor the unlike-sign reference sample is perfect. Both are deficient, though the event-mixed sample appears to be a better approximation to the ideal distribution.

The effects of QED radiation are found to be at the 5% level in the two-particle densities and cancel in the single ratios. The effects of Coulomb corrections were not routinely applied to the data, but were found to have no affect on the measured parameters r, and λ for the Gaussian model. Similarly purity corrections were not routinely made, but were investigated. They are found to have little influence on r, but cause the λ value to become consistent with 1 indicating a maximally interfering source once the effects of non-pion pairs and pions from long lived resonances are removed. This confirms the earlier measurements of the DELPHI collaboration.

Using the Gaussian model of BEC diffractive and non-diffractive data are compared and found to reveal no significant difference when using the event-mixed or unlike-sign reference sample. This analysis is the first measurement of BEC in diffractive DIS.

The non-diffractive data are further analysed in three kinematic bins of multiplicity, W, x, and Q^2 seperately. Only the event-mixed reference sample is used with the Gaussian fit model. No significant evolution of the parameters of the model is observed in W, x, or Q^2, however a deviation at the level of 3σ is seen in the differential multiplicity analysis. The results compare well with $p\bar{p}$ data at $\sqrt{s} = 1.8$ TeV and 630 GeV. Comparison of the normalised slope of the r dependence on multiplicity, $\frac{1}{\langle r \rangle}\frac{dr}{dn}$, with data from OPAL reveal a stronger multiplicity depedence at HERA. However, analysis of the systematic errors diminishes the significance of the slope to the level of a 1.8σ deviation from zero.

Finally the data are compared to three models of the Bose-Einstein effect. It is found that all three models provide a reasonable description of the data. However, at threshold, both the power-law and exponential fits provide a better description of the data than the Gaussian parametrisation. A reduced range power-law fit achieves the most favourable χ^2 verifying the idea that the failure of the power-law fit over

the full range is T is due only to the inability of the parametrisation to describe the behaviour at large T where BEC are not expected to be seen. Statistics do not yet allow the data to clearly distinguish between the models, though evidence is seen of a faster than Gaussian rise of correlations with decreasing T.

Comparison with data from other experiments indicate no evolution in $\sqrt{s}$, or any dependence on the initial state. This further lends support the the string model interpretation of the Bose-Einstein effect.

Appendix A

In this section a brief derivation of the two-particle correlation function is given. For a more detailed discussion of coherence and particle correlations the reader is referred to [84,85]. It is possible to derive the correlation function in much the same way as for photon interference in classical optics. First consider the case of a pion source with space-time position $\mathbf{x_a}$. The invariant amplitude for emission of a pion with momentum $\mathbf{k_1}$ is then given by $\Psi_1 \approx e^{i\mathbf{k_1}\cdot\mathbf{x_a}}$. Then, the probability of two pion emission from points $\mathbf{x_a}$ and $\mathbf{x_b}$ with momenta $\mathbf{k_1}$ and $\mathbf{k_2}$ is given by Ψ_{12}:

$$\Psi_{12} \propto e^{i\mathbf{k_1}\cdot\mathbf{x_a}} e^{i\mathbf{k_2}\cdot\mathbf{x_b}}$$

This assumes distinguishable particles. For indistinguishable pions the amplitude must be made symmetric upon exchange of pion 1 and 2, i.e.:

$$\Psi_{12} = \frac{1}{\sqrt{2}}(\Psi_{1a}\Psi_{2b} + \Psi_{1b}\Psi_{2a})$$

In this case the probability, P_{12}, is given by

$$P_{12} \propto \mid e^{i\mathbf{k_1}\cdot\mathbf{x_a}} e^{i\mathbf{k_2}\cdot\mathbf{x_b}} + e^{i\mathbf{k_1}\cdot\mathbf{x_b}} e^{i\mathbf{k_2}\cdot\mathbf{x_a}} \mid^2$$

which may be rewritten as:

$$P_{12} \propto 1 + Re\left[e^{-i(\mathbf{k_1}-\mathbf{k_2})\cdot(\mathbf{x_a}-\mathbf{x_b})}\right]$$

Integrating P_{12} over $\mathbf{x_a}$ and $\mathbf{x_b}$ with a source density $\rho(\mathbf{x})$ then gives:

$$P_{12} \propto 1 + \mid \tilde{\rho}(\Delta\mathbf{k}) \mid^2$$

where $\tilde{\rho}(\Delta\mathbf{k})$ is the Fourier transform of ρ, and $\Delta\mathbf{k}$ is the 4-momentum difference $(k_1 - k_2)$. Thus it can be seen that information about the source dimension is contained in the joint probability. However, this is true only when the sources are *incoherent*, i.e. any degree of coherence will dilute the effect. This is shown in the following. Introducing time dependent phase factors, $f_i(t)$ of the form $e^{i\phi_i(t)}$, the joint probability of observing two pions with momenta $\mathbf{k_1}$ and $\mathbf{k_2}$ is given by

$$P_{12} = \mid \left(f_a e^{i\mathbf{k_1}\cdot\mathbf{x_a}} + f_b e^{i\mathbf{k_1}\cdot\mathbf{x_b}}\right)\left(f_a e^{i\mathbf{k_2}\cdot\mathbf{x_a}} + f_b e^{i\mathbf{k_2}\cdot\mathbf{x_b}}\right) \mid^2$$

which leads to

$$P_{12} = \left[|f_a|^2 + |f_b|^2 + f_a^* f_b e^{-i\mathbf{k_1}(\mathbf{x_a}-\mathbf{x_b})} + f_a f_b^* e^{+i\mathbf{k_1}(\mathbf{x_a}-\mathbf{x_b})} \right] \times$$

$$\left[|f_a|^2 + |f_b|^2 + f_a^* f_b e^{-i\mathbf{k_2}(\mathbf{x_a}-\mathbf{x_b})} + f_a f_b^* e^{+i\mathbf{k_2}(\mathbf{x_a}-\mathbf{x_b})} \right] \tag{.1}$$

Note that this is now just the product of two single particle probabilities P_1 and P_2. Assuming full coherence we obtain $P_{12} = P_1 P_2$ i.e. $R = 1$ and no correlation enhancement is observable [1].

However, if the sources $\mathbf{x_a}, \mathbf{x_b}$, are relatively incoherent, the relative phase between them is not constant, but fluctuates such that the time averaged product $\langle f_a f_b^* \rangle$ is zero. Under this condition of complete incoherence the only surviving terms are:

$$P_{12} = (|f_a|^2 + |f_b|^2)^2 + 2|f_a|^2|f_b|^2 \, Re\left[e^{i(\mathbf{k_2}-\mathbf{k_1})(\mathbf{x_a}-\mathbf{x_b})} \right]$$

where for incoherent emission $P_1 P_2 = (|f_a|^2 + |f_b|^2)^2$, and so $R(= P_{12}/P_1 P_2) \neq 1$ but contains an interference term which reflects the space-time separation of the sources. As above, this expression may be integrated over the source density, to yield the usual expression :

$$R = 1 + \lambda |\tilde{\rho}(\mathbf{\Delta k})|^2 .$$

where the factor λ allows for the degree of coherence of the source. As just shown, for a fully coherent source $\lambda = 0$, so that such a source yields no observable Bose-Einstein enhancement.

---

[1] Recall that the correlation function may be written as

$$R = \frac{P_{12}}{P_1 P_2} = \frac{\langle |\Psi_{12}|^2 \rangle}{\langle |\Psi_1|^2 \rangle \langle |\Psi_2|^2 \rangle} .$$

Appendix B

The parameters of the generator (JETSET 7.4) which were changed from their default values (see [44] and [45]) are :

$$MSTJ(51) = 2 \tag{.2}$$

which includes a Gaussian parametrization according to :

$$C_2(T) = 1 + PARJ(92)\exp\left(-(\frac{T}{PARJ(93)})^2\right) \tag{.3}$$

$$MSTJ(52) = 7 \tag{.4}$$

which specifies the number of particle species for which Bose–Einstein correlations are to be included. MSTJ(52) = 7 incorporates the inclusion of: π^0, π^+, π^-, K^+, K^-, K^0_s and K^0_L.

$$PARJ(92) = 1. \tag{.5}$$

steers the nominal strength of Bose–Einstein effects for T. This parameter corresponds to the "chaoticity parameter" λ.

$$PARJ(93) = 0.38 \text{ GeV} \tag{.6}$$

is the size of the Bose–Einstein effect region in terms of the T variable, see MSTJ(51). The more conventional measure, in terms of the "radius" r of the production volume, is given by: $r = \hbar c/PARJ(93) = 0.2$ fm GeV $/PARJ(93)$. The value of PARJ(93) = 0.38 corresponds to a radius

$$r = \frac{0.2 \text{ GeV fm}}{0.38 \text{ GeV}} = 0.53 \text{ fm}.$$

References

[1] H1 Collab., DESY 93-103 (1993)

[2] H1 Collab., DESY 96-01 (1996); submitted to Nucl. Instr. and Meth. (1996)

[3] Proceedings of the HERA Workshop, vol. 1 (1991) 461-663, for recent results see: H1 Collab., pa02-082, pa02-083, pa02-084, pa02-85, pa02-086, pa02-088, contributions to 28*th* International Conference on High Energy Physics, Warsaw, 1996.

[4] Proceedings of the HERA Workshop, vol. 2 (1991) 1029-1149, for recent results see: H1 Collab., pa07-082, pa07-083, pa07-084, pa07-85, pa07-086, pa07-087, contributions to 28*th* International Conference on High Energy Physics, Warsaw, 1996.

[5] C. Callan, D. Gross Phys. Rev. Lett. 21 (1968) 311.

[6] NMC. Collab., submitted to Nucl. Phys. B (1996). hep-ph/9610231; BCDMS Collab., Phys. Lett. **B233** (1989) 485.

[7] A. De Roeck, J. Phys. G. **19** (1993) 1549.

[8] F. Close, Introduction to Quarks and Partons (1979); L. Leader, E. Predazzi, Gauge Theories and the New Physics (1982).

[9] J. I. Freidman et. al., Ann. Rev. Nucl. Sci., **22** (1972) 203.

[10] GARGAMELLE Collab., Nucl. Phys. **B85** (1975) 269.

[11] M. Breidenbach et al., Phys. Rev. Lett. **23** (1969) 935.

[12] Yu. L. Dokshitzer, Sov. Phys. JETP **46** (1977). 641; V. Gribov, L. Lipatov, Sov. J. Nucl. Phys. 15 (1972) 675; G. Altarelli, G. Parisi, Nucl. Phys. **B126** (1977) 298.

[13] V. Gribov et. al., Sov. J. Nucl. Phys. 15 (1972) 438.

[14] E.A. Kuraev, L.N. Lipatov, V.S. Fadin, Sov. Phys. JETP 44 (1972) 199.

[15] Y.Y. Balitsky, L.N. Lipatov, Sov. J. Nucl. Phys. 28 (1978) 282.

[16] H1 Collab., Phys Lett. **B354** (1995) 494.

[17] L. Gribov, E. Levin, M. Ryskin, Phys. Rep. **C100** (1983) 1.

[18] J. Kwieciński, J. Phys. G. **19** (1993) 1443.

[19] A.H. Mueller, J. Qui, Nucl. Phys **B268** (1986) 427.

[20] A.J. Askew, J. Kwieciński, A.D. Martin, P.J. Sutton, **D47** (1993) 3775 .

[21] E. Levin, K. Charchula, Proceedings of the HERA Workshop, vol 1, (1991) 223.

[22] K. Prytz Phys. Lett. **B311** (1993) 286.

[23] H1 Collab., Phys Lett. **B354** (1995) 494.

[24] H1 Collab., Nucl. Phys. **B449** (1995) 3.

[25] H1 Collab., Phys Lett. **B346** (1995) 415.

[26] ALEPH Collab., Phys. Lett. **B284** (1992) 163; DELPHI Collab., PPE 91-181;
OPAL Collab., Z. Phys. **C59** (1993) 1.

[27] H1 Collab., Nucl. Phys. **B445** (1995) 3.

[28] H1 Collab., Z. Phys. **C94** (1994) 377.

[29] H1 Collab., DESY-96-215, submitted to Nucl. Phys. B. (1996).

[30] H1 Collab., Z. Phys. **C72** (1996) 593.

[31] J. Bähr et al., Nucl. Instr. and Meth. **A324** (1993) 145.

[32] J. Bähr et al., Nucl. Instr. and Meth. **A330** (1993) 103.

[33] P. Newman, Doctoral thesis, University of Birmingham, (1996) unpublished.

[34] A. Donnachie, P. Landshoff, Phys Lett **B296** (1992) 227.

[35] H1 Collab., pa02-061 contribution to 28*th* International Conference on High Energy Physics, Warsaw, 1996.

[36] G. A. Schuler, H. Spiesberger, Proc. HERA workshop, Hamburg (1991) vol. 3, p. 1419.

[37] A. Kwiatkowski, H. Spiesberger, H.-J. Möring, Proc. HERA workshop, Hamburg (1991) vol. 3, p. 1294.

[38] G. Ingelman, Proc. HERA workshop, W. Buchmüller, G. Ingelman (eds.), Hamburg (1991) vol. 3, p. 1366.

[39] G. Gustafson and U. Petterson, Nucl. Phys. **B306** (1988), 746; G. Gustafson, Phys. Lett. **B175** (1986), 453.

[40] G. Altarelli, G. Parisi, Nucl. Phys. 126 (1977) 297.

[41] L. Lönnblad: Comput. Phys. Commun. 71 (1992) 15.

[42] H. Jung, Comp. Phys. Comm. **86** (1995), 147.

[43] Contr. paper by the H1-Collab. to the Topical Conf. on Hard Diffractive Processes, Eilat, Israel, Feb. 1996.

[44] T. Sjöstrand, CERN-TH 7112/93.

[45] L. Lönnblad and T. Sjostrand, Phys. Lett. **B351** (1989) 293.

[46] R. Brun et al., GEANT3, CERN DD/EE/84-1 (1987).

[47] H1 Collab., Nucl. Instr. and Meth. **A372** (1996) 399.

[48] A. Mehta, Doctoral thesis, University of Manchester (1994).

[49] H. Spiesberger et. al., Proceedings of the HERA Workshop, vol. 2 (1991) 798.

[50] U. Bassler, Dissertation, Univ.de Paris VI (1993)

[51] H1 Collab., DESY 94-231 (1994).

[52] T. Eckel, Diploma Thesis, University of Hamburg, DESY report H1-08/94-371 (1994), unpublished.

[53] L. Favart, M. Fleischer, M. Hütte, Z. Zhang DESY FH1K-96-01.

[54] M. Gruné at al., internal H1 note h1-02/95-425.

[55] M.W. Krasny et al., internal DESY note, DESY 91-117.

[56] A. Blondel and F. Jaquet, Proceedings of the study of an ep facility for Europe, ed. U. Amaldi, DESY **79-48** 391 (1979).

[57] S. Bentvelsen et.al.,Proceedings of the HERA Workshop, vol. 1 23 (1991).

[58] K. Müller, Doctoral Thesis, Universität Zürich, 1994.

[59] J. Feltesse, Proceedings of the HERA Workshop, vol. 1 (1987) 23.

[60] R. Hanbury-Brown and R. Twiss,*Phil. Mag.* **45** (1954) 663-682.

[61] A. Bialas, R. Peschanski, Nucl. Phys. **A545** (1992) 285c; Acta Phys. Pol. **B23** (1992) 561.

[62] H1 Collab., Nucl. Phys. **B480** (1996) 3

[63] H1 Collab., Nucl. Phys. **B472** (1996) 3

[64] H1 Collab., Nucl. Phys. **B463** (1996) 3

[65] G. Lafferty, Z. Phys. **C60** (1993) 659

[66] S. Haywood, Rutherford Appleton Lab., RAL 94-074 (1994)

[67] R. Lednicky, V. Lyuboshits, Sov. J. Nucl. Phys. 35 (1982) 770

[68] B. Andersson and W. Hofmann, Phys. Lett. **B169** (1986), 364.

[69] E. A. De Wolf, L. M. Dremin, and W. Kittel, Phys. Rep. **270** (1996), 1.

[70] P. Abreu et al., DELPHI Collab., Z. Phys. **C63** (1994) 17.

[71] M. Suzuki, Phys. Rev. **D35** (1987), 3359.

[72] A. S. Davydov, *Quantum Mechanics* (Pergamon Press, London, 1965)

[73] M. G. Bowler, Phys. Lett. **B270** (1991), 69.

[74] M. Biyajima et al., Phys. Lett. **B353** (1995), 340.

[75] P. Abreu et al., DELPHI Collab., Phys. Lett. **B286** (1992) 201.

[76] D. Decamp et al., ALEPH Collab., Z. Phys. **C54** (1992) 75.

[77] M. Arneodo et al., EMC Collab., Z. Phys. **C32** (1986) 1.

[78] P. D. Acton et al., OPAL Collab., Phys. Lett. **B267** (1991) 143.

[79] V. A. Korotkov et al., Big Bubble Chamber Neutrino Collab., Z. Phys. **C60** (1993) 37.

[80] C. Albajar et al., UA1 Collab., Phys. Lett. **B226** (1989) 410.

[81] G. Alexander et al., OPAL Collab., Z. Phys. **C72** (1996) 389.

[82] T. Alexopoulos et al., E735 Collab., Phys. Rev. **D48** (1993) 1931.

[83] H1 Collab., Z. Phys. **C72** (1996) 573.

[84] M. Bowler, Z. Phys. **C29** (1985) 617.

[85] W. Zajc, Proceedings of the NATO Advanced Study Institute on Particle Production in Highly Excited Matter, 1992, p.435 Eds. H Gutbrod et al.

Acknowledgments

I would like to take this opportunity to thank all those people who have helped me and without whom the work for this thesis would have been not only more difficult, but considerably less engaging. I thank Wladimir Von Schlippe, my supervisor, for introducing me to HERA physics and the subject of multi-particle correlations, I am grateful to Graham Thompson, Frank Botterweck, and Andrew Mehta for setting me straight on many points of experimental technique, and their patient explanations have given me a clearer idea of the role of an experimentalist. Whilst at DESY I learnt a great deal from discussions with people which helped clarify my understanding in a general way and so I would like to thank Michael Kuhlen, Dave Cussans and all the people of building 2G with whom I was fortunate enough to share offices with, in particular Sean Willard, Wieslaw Dlugosz, Vicki Hudgson, and Paul Newman. For providing me with an insight into correlation analyses and helping me in grasping the details of this work I extend my gratitude to Eddi de Wolf, Frank Botterweck, and Genya Levin.

During my stay in Hamburg I made a number of friends whose company is now very dear to me. Vicki introduced me to the Hamburg lifestyle, the comfortable interiors of the Insbeth, and the Kick & Co., and the joys of cheese on a stick. Despite everything I would like to declare my appreciation of her cooking. Chandy, thanks for being such a socially aware person so as to be able to provide piping hot custard at a moments notice. Andy I would like to thank for being the perfect housemate despite his, frankly unnatural, appetite for (raw) liver. His help and advice in my photographic endeavors was invaluable, though there is one final challenge still to complete. I also appreciate the friendship offered by both Paul and Dave and for helping to make Bleicherstrasse such an enjoyable place to live.

Thanks also to all the people in Hamburg, Paul S., Lee, Julian, Kirtsee, Paul T.,

Tim, Stuart, Molly, Hugh, Jane, Ines, Ben, and at QMW Andy, Thanos, Simon, Dave K., Derek N-C (for his excellent advice on how to style my hair), Murrough, Rob, Keith, Martin, Daniel, and Caroline.

My older friends have given me much support over the years and I would particularly like to acknowledge Joss who is a constant source of enlightenment, and without whom my time in Manchester would have been a void - thanks with love and respect. Andy-B, and M I would also like to mention for their patience and regard.

Finally I thank my parents for the support they have offered me over the years, and to my brothers Faraz, and Saqib.